

Stability and Vortex Shedding of Bluff Body Arrays

S. J. Parker and S. Balachandar

ACRC TR-189

August 2001

For additional information:

Air Conditioning and Refrigeration Center
University of Illinois
Mechanical & Industrial Engineering Dept.
1206 West Green Street
Urbana, IL 61801

(217) 333-3115

*Prepared as part of ACRC Project #112
Promotion of Vortex Shedding and Heat Transfer Enhancement
S. Balachandar, Principal Investigator*

The Air Conditioning and Refrigeration Center was founded in 1988 with a grant from the estate of Richard W. Kritzer, the founder of Peerless of America Inc. A State of Illinois Technology Challenge Grant helped build the laboratory facilities. The ACRC receives continuing support from the Richard W. Kritzer Endowment and the National Science Foundation. The following organizations have also become sponsors of the Center.

Amana Refrigeration, Inc.
Arçelik A. S.
Brazeway, Inc.
Carrier Corporation
Copeland Corporation
Dacor
Daikin Industries, Ltd.
DaimlerChrysler Corporation
Delphi Harrison Thermal Systems
Frigidaire Company
General Electric Company
General Motors Corporation
Hill PHOENIX
Honeywell, Inc.
Husmann Corporation
Hydro Aluminum Adrian, Inc.
Indiana Tube Corporation
Invensys Climate Controls
Kelon Electrical Holdings Co., Ltd.
Lennox International, Inc.
LG Electronics, Inc.
Modine Manufacturing Co.
Parker Hannifin Corporation
Peerless of America, Inc.
Samsung Electronics Co., Ltd.
Tecumseh Products Company
The Trane Company
Thermo King Corporation
Valeo, Inc.
Visteon Automotive Systems
Wolverine Tube, Inc.
York International, Inc.

For additional information:

*Air Conditioning & Refrigeration Center
Mechanical & Industrial Engineering Dept.
University of Illinois
1206 West Green Street
Urbana, IL 61801*

217 333 3115

Abstract

The primary purpose of this study was to develop an understanding of the stability of laminar flow through bluff body arrays, and investigate the nature of the unsteady vortex shedding regime that follows. The flow was numerically investigated using a specially developed multi-domain spectral element solver. Important criteria in the solver development were flexibility, efficiency, and accuracy. Flexibility was critical to the functionality of the code, as arrays of varying geometry were investigated. Efficiency with a high degree of accuracy was also of primary importance, with the code implemented to run efficiently on today's massively parallel architectures.

Numerical two-dimensional stability analysis of the flow in several configurations of inline and staggered array geometries was performed. The growth rate, eigenfunction, and frequency of the disturbances were determined. The critical Reynolds number for flow transition in each case was identified and compared to that of flow over a single body. Based on the solutions of the laminar flow, a one-dimensional analytical analysis was performed on selected velocity profiles in the wake region. The results of this analysis were used to guide the interpretation of the two dimensional results and formulate a general theory of stability of inline and staggered bluff body arrays. The nature of the flow in the unsteady regime following the onset of instability was examined for an inline and a staggered arrangement. Particular attention was focused on the vortex shedding which was visualized and quantified through computation of the flow swirl, a quantity which identifies regions of rotary motion. The conditions required for the generation of leading edge vortex shedding were identified and discussed. Finally, a third geometry related to the inline and staggered arrays was considered. Flow solution data for this geometry is presented and its suitability as a model for louvered arrays was discussed.

Table of Contents

Chapter 1	Introduction	1
1.1	Background, Motivation, and Present Work	1
1.2	Literature on Parallel Fins	4
1.3	Literature on Louvered Fins	8
Chapter 2	Solution Methodology	13
2.1	Introduction	13
2.2	Navier - Stokes Equations	13
2.2.1	General	13
2.2.2	Periodic Boundary Conditions	15
2.2.3	Outflow Boundary Condition	17
2.3	Energy Equation	19
2.3.1	General	19
2.3.2	Periodic Boundary Condition	20
2.4	Temporal Discretization	22
2.5	Spatial Discretization	24
2.5.1	Fourier Discretization	24
2.5.2	Multi-Domain Spectral Discretization	25
2.6	Influence Matrix Method	28
2.7	Sub-domain Solver	31
2.8	Program Features	34
Chapter 3	Code Validation	38
3.1	Introduction	38
3.2	Infinite Staggered Array	38
3.3	Square Cylinder	43
Chapter 4	Stability of Bluff Body Arrays	48
4.1	Introduction	48
4.2	Numerical Two-Dimensional Stability Analysis	50
4.3	Two Dimensional Stability Results	54
4.3.1	Inline Array Results	55
4.3.2	Staggered Array Results	63
4.3.3	Non-periodic Results	68
4.4	One Dimensional Floquet Stability Analysis	77
4.5	Rescaling and Parametric Dependence	85
4.5.1	Rescaling	85

4.5.2	Parameter Dependence	88
Chapter 5	Time-Periodic Flow Regime	91
5.1	Introduction	91
5.2	Time Periodic Flow	92
5.2.1	Inline Array	95
5.2.2	Staggered Array	102
5.3	Leading Edge Vortex Shedding	108
5.4	Trailing Edge Vortex Shedding	117
Chapter 6	Intermediate Offset Array	122
6.1	Introduction	122
6.2	Definitions	124
6.3	Flow Solutions	126
6.3.1	Flow Angle	126
6.3.2	Stability	130
6.3.3	Unsteady Flow	132
Chapter 7	Conclusions	141
References	145

Chapter 1

Introduction

1.1 Background, Motivation, and Present Work

The nature of the flow over a bluff body has for many years been the subject of extensive investigation. Experimental, numerical, and theoretical analysis have all been applied to studying cases such as the canonical flow over a circular cylinder, and to other cases like flow over square, rectangular, or elliptic cylinders. It has been observed for all of these geometries that the flow goes through a progression of regimes (Roshko [43]). At low Reynolds number the flow is steady and laminar. With increasing Reynolds number the flow becomes unsteady in a two-dimensional periodic manner with regular vortex shedding forming a Karman vortex street in the wake. At even higher Reynolds numbers the flow becomes three-dimensional, and finally becomes chaotic and turbulent. For a given geometry the transition between these states occur at precise values of the Reynolds number based on the body thickness. Stability analysis has been performed on bodies of various cross-section, and elongated bodies have been seen to have a higher value of the critical Reynolds number (Oertel [37], Jackson [20]). For a flat plate oriented normal to the flow the critical Reynolds number has been found to be 27.8. For a circular cylinder it has been found to be 45.4, and for an elliptic cylinder of aspect ratio two it has been found to be 76.8. The stability of these flows is determined by two parameters, the Reynolds number, and the aspect ratio of the body.

Much of the fundamental work on bluff body flows has been focused on the flow over a single body. Many applications, however, involve the flow past a large number of bluff bodies in close proximity to one another. Examples of such applications are porous media flow, fluidized beds,

and compact heat exchangers. Compact heat exchangers have been the subject of research for over half a century and continue to be studied due to the complexities of the flow and their growing importance in applications where high heat transfer efficiency is important. Compact heat exchangers are generally characterized as interrupted heat transfer surfaces, but they are often modeled as regular arrays of bluff bodies. Three common models often studied are the inline array, offset-strip or staggered array, and louvered array, which are shown in Figures 1.1 and 1.2. Similar to flows involving only a single body, the flow through bluff body arrays sees a similar transition from a laminar, to unsteady, to turbulent flow (Mochizuki et al. [34]). An important element in the design of a compact heat exchanger is the heat transfer coefficient between the bodies, or fins, composing the device and the surrounding fluid. Two mechanisms have been identified in interrupted surfaces which provide improved heat transfer over that of an uninterrupted-interrupted surface. The first is interrupted boundary layer growth, which occurs as the flow moves through the array (Sparrow et al. [45]). As a boundary layer develops along a surface the thermal resistance increases as the boundary layer thickens. Multiple fins allow for the periodic destruction and re-growth of the fluid and thermal boundary layers, which enhances the overall heat transfer coefficient. A second mechanism providing enhanced heat transfer is the self sustained oscillation of the flow occurring after the transition from laminar to periodic unsteady flow. Heat transfer improvements in this regime has been attributed to the regular generation of vortices along the surfaces of the bodies. These vortices act to increase mixing by sweeping hot surface fluid into the free stream and replacing it with cooler fluid (DeJong and Jacobi [11], DeJong et al. [12]). Unfortunately the heat transfer improvements associated with both mechanisms come with an associated pressure drop penalty. Despite the fundamental nature of the transition from laminar to unsteady flow, and the importance of the vortex shedding mechanism to heat transfer enhancement, the stability of the laminar flow in bluff body arrays has not been fundamentally described. This is in part due to the large number of parameters effecting the flow stability, including the Reynolds number, aspect ratio of the bodies, horizontal and vertical spacing in the array, as well as the type of arrangement of the array.

The primary purpose of this study is, therefore, an investigation of the stability of the laminar flow through bluff body arrays and an investigation of the nature of the unsteady vortex shedding regime that follows. The stability of the flow in simple geometries is often analytically investi-

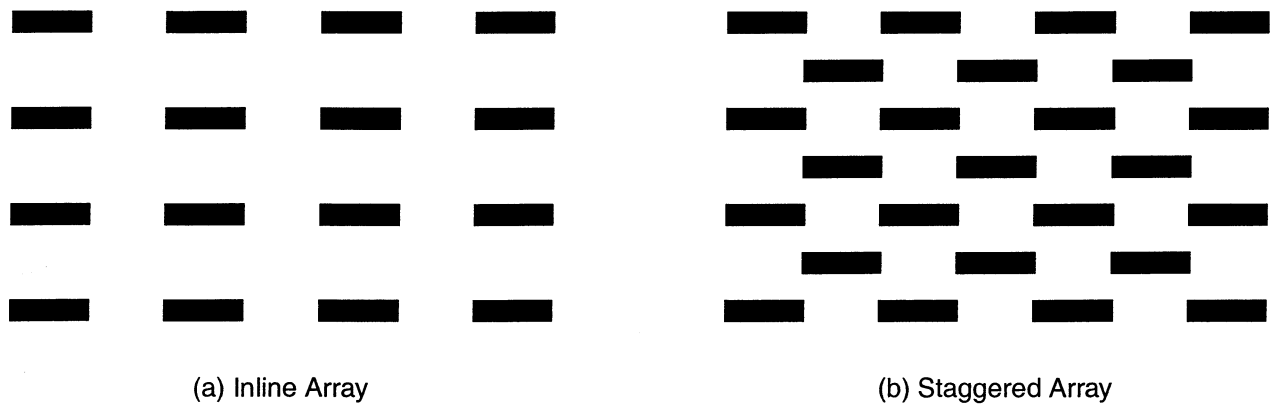


Figure 1.1: Inline and Staggered Arrays

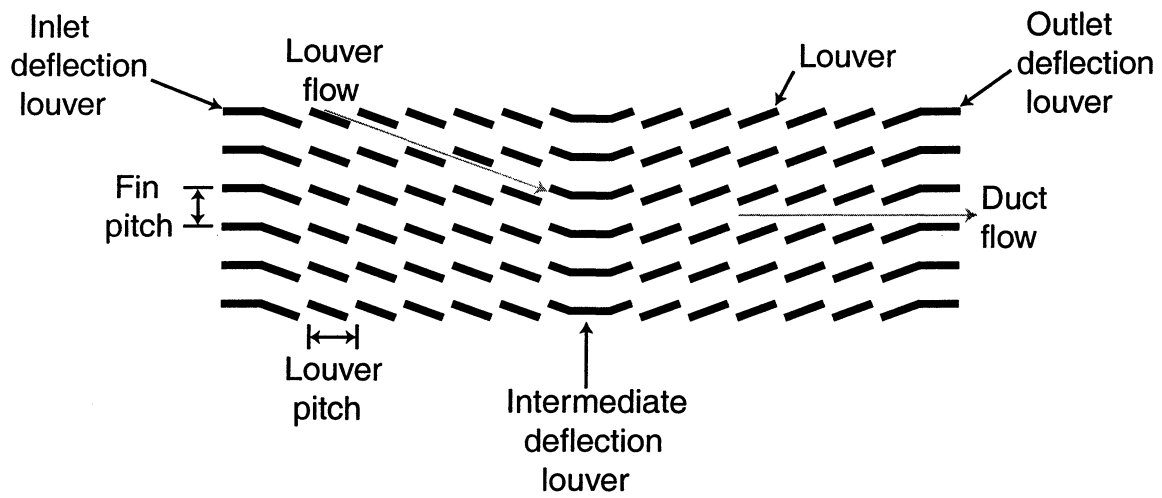


Figure 1.2: Louver Array

gated, however the complexity of the bluff body array geometry precludes such an approach, and instead a numerical investigation has been undertaken. To this end a multi-domain spectral element solver has been developed. Important criterion in the solver development were flexibility, efficiency, and accuracy. Flexibility was critical to the functionality of the code, as multiple array geometries were required to be investigated. Efficiency with a high degree of accuracy was also of primary importance, and the code was implemented to run efficiently on today’s massively parallel architectures.

The code developed was applied to performing a two-dimensional stability analysis of the flow in several configurations of inline and staggered array geometries. The growth rate, eigenfunction, and frequency of the disturbances were determined. The critical Reynolds number for flow transition in each case was identified and compared to that of flow over a single body. Based on the numeric solutions of the laminar flow, a one-dimensional analytical analysis is performed on selected velocity profiles in the wake region. The results of this analysis were used to guide the interpretation of the two dimensional results and formulate a general theory of stability of inline and staggered bluff body arrays. The nature of the flow in the unsteady regime following the onset of instability was examined for an inline and a staggered arrangement. Particular attention was focused on the vortex shedding which was visualized through computation of a quantity referred to as swirl, which identifies regions of rotary motion. The conditions required for the generation of leading edge vortex shedding were identified and discussed. Finally, a third geometry related to the inline and staggered arrays was considered. Flow solution data for this geometry is presented and its suitability as a model for louvered arrays is discussed.

1.2 Literature on Parallel Fins

Two basic and commonly used types of interrupted heat transfer surfaces are the inline and offset, or staggered, geometries. Idealized two dimensional models of these two geometries are shown in Figure 1.1. For over half a century research on the flow and heat transfer properties of these surfaces has been ongoing. This section presents an overview of this past research.

Early investigations of the flow in interrupted heat transfer surfaces by Norris and Spofford [36] and Manson [31] demonstrated that these surfaces could provide superior heat transfer when com-

pared to that of a continuous flat plate surface. Evaluations of the heat transfer and pressure drop characteristics for a number of these surfaces were performed by Kays and London [24] in 1964 and by London and Shah [28] in 1968 with a view toward providing practical design information. In 1975 Wieting [51] utilized the available data for offset strip fin arrays, primarily that of Kays and London [24] and London and Shah [28], to develop correlations for the f and j factors. Two sets of correlations were developed, one for laminar flow at low Reynolds number, and one for turbulent flow at high Reynolds number. No correlations were presented for the intermediate Reynolds number range. It was found that fin thickness did not effect the laminar flow regime, and the channel aspect ratio did not effect the turbulent regime.

In 1977 Sparrow, Baliga, and Patankar [45] performed perhaps the earliest numerical simulation of developing flow through an offset strip fin array. Several array configuration were analyzed, but only steady flow over zero thickness fins was considered. Comparisons where made to the results for an equivalent continuous flat plate geometry and the offset strip fin arrangement was found to provide superior heat transfer performance over a range of operating conditions. It was also noted that the flow entered a periodic fully developed state as it progressed through the array. Using this observation Patankar, Liu, and Sparrow [38] developed an analytical formulation for studying flow and heat transfer in geometries with periodic streamwise variation. This methodology allowed for the investigation of the fully developed flow and heat transfer in large arrays of periodic geometry by solving only for the flow in a small module. The approach was used to generate the numeric solution of the flow through an array of zero thickness offset plates oriented in the transverse direction to the flow. In 1981 Patankar and Prakash [39] applied this methodology to study fully developed flow and heat transfer in the offset strip geometry for steady flow over finite thickness fins. Their study focused on the effects of fin thickness on the flow structure, friction factor, and heat transfer. The finite thickness of the fins was found to produce recirculation regions, and increase the pressure drop disproportionately more than the increase in heat transfer. Local heat transfer data along the surface of the fins were also presented. In 1979 Sparrow and Liu [47] presented a computational study comparing the heat transfer and pressure drop of steady laminar flow over inline, staggered, and continuous plate surfaces of zero thickness. In this study a finite length array was subjected to a uniform oncoming flow and it was found that both the inline and staggered configurations yielded

superior performance over the continuous flat plate for a range of operating conditions.

Cur and Sparrow [9] experimentally considered the flow over two collinear flat plates aligned with the flow in 1978. Average heat transfer results for both plates were determined by using a naphthalene sublimation technique and the heat-mass transfer analogy. The effects of fin thickness, fin spacing, and Reynolds number on the heat transfer coefficients were studied parametrically. Sparrow and Hajiloo [46] also employed the naphthalene sublimation technique in 1980 to study flow and heat transfer in a staggered array of plates. Plate thickness and Reynolds number were parametrically varied and their effects on heat transfer and pressure drop were presented. The flow was observed to become fully developed after the first row of plates for all Reynolds numbers considered and both heat transfer and friction factor were found to increase with plate thickness.

In 1982 Mochizuki and Yagi [33] performed flow visualization studies of the vortex shedding for a range of multi-plate configurations including several staggered arrangements with a varying number of plates in the streamwise direction. Vortex shedding with multiple Strouhal numbers was observed for staggered arrays with nine or fewer streamwise plate rows while arrays containing more than nine rows shed with only a single Strouhal number. Vortex shedding was also observed to begin at the rear of the array and move forward rapidly with increasing Reynolds number. In 1988 Mochizuki, Yagi, and Yang [34] performed wind tunnel and water channel tests on offset strip and perforated plate arrangements, recording the pressure drop, turbulence intensity, and performing flow visualizations. Oscillatory vortex shedding and turbulent flows were observed for the offset strip arrangement, with the location of onset varying within the array dependent on the Reynolds number.

Yang [55] in 1983 discussed the concept of a secondary laminar flow regime which induces an upward deviation in the f and j curves for interrupted surfaces due to oscillations in the flow. The flow oscillation was attributed to the hydro-dynamic instability of free shear layers and analytic stability theory, based on the Orr-Sommerfeld equation, was used to formulate a frame work for determining the critical Reynolds number. It was also suggested that the secondary laminar flow regime is the optimal operational range for heat exchangers.

In 1986 Mullisen and Loehrke [35] experimentally investigated the flow and heat transfer in inline and staggered arrays in a wind tunnel. Flow visualization was also performed using the Schlieren

technique. Three flow regimes were identified, steady, general unsteady, and periodic unsteady. In contrast to Mochizuki and Yagi [33] the flow state was found to be uniform throughout the array. The staggered arrangement was also observed to be more stable than the inline. The impact of varying the streamwise spacing between bodies on friction factor and heat transfer was investigated and the performance of the different array configurations was compared to that of a continuous plate. The interrupted surface geometries were found to provide superior heat transfer, partly attributable to the increased mixing occurring in the unsteady flow regimes.

In 1987 Joshi and Webb [22] developed a semi-analytic model for the friction factor and heat transfer coefficient in the offset strip geometry. This model employed different components for the laminar and turbulent flow regimes, with the laminar components based the numeric results of Sparrow and Liu [47], and the turbulent component based on correlations of the data of Kays and London [24] and London and Shah [28]. A correlation were also developed for identifying the point of transition between laminar and turbulent models. Flow visualization experiments were also performed and four flow regimes were noted from laminar to vortex shedding flow, with the regime found not to vary throughout the array. Friction factor data was also gathered for eight offset strip arrays, and entirely empirical correlations for the f and j factors were also presented. A discussion of the effect of practical issues such as leading edge burrs and surface roughness was also given.

In 1988 Kurosaki, Kashiwagi, Kobayashi, Uzuhashi, and Tang [26] used laser holographic interferometry to visualize the isotherms for flow over an isolated body, two bodies in parallel, two collinear bodies, and several offset array configurations, including a modified one with reported enhanced heat transfer. In 1991 Xi, Futagami, Hagiwara, and Suzuki [54] followed the work of Xi, Murata, Suzuki, Hagiwara [53] with a flow visualization experiment of flow through an offset array. Flow instability was observed to initially arise in the wake of the downstream fins and move upstream in the array with increasing Reynolds number. The Reynolds number at which the onset of instability occurred was found to be dependent on the fin pitch, with smaller fin pitch producing a less stable flow. Fluctuations in the velocity and temperature were found to correlate, indicating that additional momentum and heat transfer occurred due to the wake instability.

In 1990 Manglik and Bergles [29] compiled an extensive bibliography of the literature associated

with offset strip fins. This was followed in 1995 by Manglik and Bergles [30] wherein the existing data and correlations for the offset strip geometry were reviewed and new correlations were presented. The new correlations cover the entire Reynolds number range from laminar to turbulent flow. This was achieved by asymptotic matching of the correlations in the laminar and turbulent regimes.

In 1997 DeJong and Jacobi [11] performed naphthalene sublimation experiments on a standard and a modified staggered array, with the modified staggered array having two different fin pitches. In addition, water tunnel flow visualizations were performed on the staggered geometry. Fin averaged heat transfer results were presented for fins at different streamwise locations in the array and local surface heat transfer data were determined using a laser profilometer. Heat transfer rates were found to be appreciably effected by the presence of upstream vortex shedding, and vortex shedding was found to begin at different locations in the array at different Reynolds numbers. The onset of instability was also found to be effected by the geometric parameters of the array, with a smaller fin pitch producing a less stable flow.

In 1997 Zhang et al. [59] [58] performed a numeric simulation of flow in staggered and inline geometries using the periodic formulation of Patankar, Liu, and Sparrow [38]. Simulations were conducted for unsteady flow over finite thickness fins. In addition, symmeterized simulations producing laminar flows at super critical Reynolds numbers were performed and used to determine the impact of vortex shedding on heat transfer and friction factor. At high Reynolds numbers three dimensional simulations were performed and showed that two-dimensional models can over predict heat transfer and friction losses.

1.3 Literature on Louvered Fins

Another form of interrupted surface commonly used in heat exchangers is the louvered fin design, shown in Figure 1.2. Louvered fin surfaces are easily manufactured in large quantities and therefore used widely in many industries, such as the automotive industry. Commonly these fins are cut out of sheet metal and bent to form a louvered geometry. Louvered surfaces have been utilized in heat exchangers for over fifty years and have been the subject of research for over thirty years.

The earliest reported investigation of the flow in louvered fins arrays was performed by Beau-

vais [4] in 1965. Beauvais's utilized a smoke visualization technique on 10:1 scale models, which produced only qualitative observations about the flow. A result of his experiments was the observation that the flow was largely parallel to the louver direction, previously it had been supposed that primary function of the louvers was to increase the turbulence of the flow through effective surface roughness. In 1983 Beauvais's work was followed by Davenport [10] who performed similar visualization experiments. Davenport determined that the nature of the direction of the flow through the louver array was dependent upon the Reynolds number based on louver pitch. At high values of this Reynolds number the flow direction was observed to be parallel to the louver direction; however, for low values the flow was largely unaffected by the louvers and traveled in the duct flow direction. Heat transfer and friction factor data were also presented for eight different louvered geometries. These data were seen to correlate with the Blasius results for flow over a flat flat, which in turn suggested that laminar boundary layer mechanisms played a dominant role in the heat transfer and friction phenomena.

In 1986 Lee [27] performed an experimental investigation in which pressure drop and heat transfer characteristics were determined for a three by eight array of louver fins at incidence angles varying from twenty to thirty-five degree. Heat transfer data were determined through a naphthalene sublimation technique applied to the central row of fins. Lee observed a significant increase in the Nusselt number of the array over that of a continuous flat plate. However, an increase in the pressure drop was also found. Fin averaged Nusselt number data along the front and back faces of an individual fin were also reported with the forward face showing a higher value than the rear. At low Reynolds numbers the average overall Nusselt number was found to closely approximate that found from laminar short duct theory, but at higher Reynolds numbers significant variation occurred. A similar study was performed by Zhang and Lang in 1989 [57] in which they studied the effects of plate length and angle on heat transfer and pressure drop. They present a correlation for the Sherwood number in the fully developed region, which they found to begin after the fourth row of fins.

Two investigations of flow in louver arrays were performed by Achaichia and Cowell in 1988, an experimental study [2] and a numerical investigation [1]. In their experimental investigation, heat transfer and pressure drop data were determined for fifteen different geometries through wind tunnel

testing. From these data, correlations for both the Stanton number and the friction factor were derived. The experimental Stanton number data show good agreement with a duct flow solution at low Reynolds number and flat plate flow at high Reynolds number. This result further confirms the earlier observations of flow varying from "duct" to "louver" flow with the Reynolds number. In their numerical work, steady flow around a single zero thickness louver in an infinite array was calculated through the use of periodic boundary conditions on the edges of the computational domain. The variation of the flow direction with Reynolds number, louver spacing, and louver angle was determined and a correlating equation for flow angle was presented. The steady flow constraint and the zero thickness of the louver precluded evaluation of any unsteady vortex shedding phenomena.

In 1989 Aoki, Shinagawa, and Suga [3] performed an experimental investigation on a reversing louver array with a central deflection louver. Wind tunnel tests were performed on several different array configurations composed of electrically heated louver elements. The overall heat transfer coefficient for each element in the array was determined. Effects of fin pitch, louver pitch, and louver angle were noted. The heat transfer coefficient of the louvers directly behind the deflection louver were found to be lower than those upstream. For a similar geometry Suga and Aoki [49] performed a two dimensional finite difference simulation. Steady flow and temperature solutions for finite thickness fins were obtained. The temperature solutions allowed an analysis of the thermal wake behavior and local Nusselt number data along the fin surface to be obtained. The effect of the fin thickness, pitch, louver pitch, and angle on the global Nusselt number was also investigated and design recommendations were made. The steady nature of the solutions did not allow for an assessment of the effects of flow unsteadiness and vortex shedding. Hiramatsu, Ishimaru, and Matsuzaki [18] also performed finite difference simulations of the flow and heat transfer for a similar geometry in 1990. Steady two-dimensional computations were used to predict the flow and determine when it would be duct or louver directed. The results were compared to experimental dye visualizations and found to yield good agreement so long as the flow was in the steady laminar state. Local and global Nusselt number results were also reported for various array configurations. The flow was noted to be duct directed at low Reynolds numbers and for large values of fin pitch.

Webb and Trauger [50] performed dye visualization experiments on geometries similar to those

used in the investigations cited above, in 1991. They defined a flow efficiency based on the mean flow direction relative to the louver angle and analyzed the effect of varying fin pitch, louver pitch, and louver angle. Based on their data a correlation was presented for calculating flow efficiency, which they associate with improved heat transfer. It was also noted that the flow is not laminar over the range of practical interest.

Huang and Tao [19] investigated heat transfer and pressure drop over arrays of non-uniform plates using the naphthalene sublimation technique. Nine array configurations were tested, all having a louver angle of twenty-five degrees, but with varying length ratios of successive plates and fin to louver pitch ratio. Sherwood number and friction factor data were recorded and the performance of the non-uniform plate array was compared to that of the uniform plate array. Mass transfer was found to be superior in the non-uniform plate array at low Reynolds number but below that of the uniform array at high Reynolds numbers. The friction factor was always lower for the non-uniform array. The flow and mass transfer were found to be fully developed after the fifth element in the array. In 1995 Cowell, Heikal, and Achaichia [8] provide an overview and summary of previous investigations on louvered fin heat transfer surfaces. A discussion of the flow mechanics is provided followed by a comparison of louvered surface performance to that of the offset strip configuration, with louvered surfaces found to outperform the offset strip.

In 1999 DeJong [13] studied the flow characteristics and heat transfer in three louvered geometries experimentally with the naphthalene sublimation technique. A comparison was made to offset strip geometries, and louvers were found to provide consistently higher heat transfer, but also have a higher friction factor. Also noted was the approximate point of transition from laminar to unsteady flow for the geometries tested. The louver arrangements were found to be less stable than an offset strip arrangement with the same hydraulic diameter. Also in 1996 Zhang [60] performed a numerical investigation of the flow through a louver array of infinite extent. The infinite array was modeled through the use of periodic boundary conditions. The simulations were two-dimensional but included the effects of flow unsteadiness and finite fin thickness. Detailed flow and temperature solutions were obtained and heat transfer and friction factor data were reported. Steady laminar flow was observed at lower Reynolds numbers and unsteady, vortex shedding was seen at higher Reynolds numbers. Data on the local Nusselt number distribution along the fin surface were also

presented and shown to be effected by the presence of vortices shed from the leading edge of the louver.

Chapter 2

Solution Methodology

2.1 Introduction

The solution of fluid flow problems by computational means requires the temporal and spatial discretization of the set of governing equations. The solution technique must have sufficient accuracy to properly capture the underlying physics of the flow and still be efficient enough, in terms of memory usage and computational time, to be of practical use. Furthermore, for the class of problems being considered it is important that the numerical implementation possess a degree of flexibility in terms of the range of geometries that it may be configured to solve. This chapter describes the governing equations used in the analysis, the implementation of the various boundary conditions, the spatial and temporal discretization of these equations, and discusses some of the aspects of the numerical solution procedure.

2.2 Navier - Stokes Equations

2.2.1 General

Only flows involving incompressible, Newtonian, fluids are being considered. The behavior of such fluids is represented by the classic incompressible Navier-Stokes equations which have the form:

$$\frac{\partial \vec{u}}{\partial t} + \vec{u} \cdot \nabla \cdot \vec{u} = -\nabla p + \frac{1}{Re} \nabla^2 \vec{u} \quad (2.1)$$

$$\nabla \cdot \vec{u} = 0 \quad (2.2)$$

In the above equations \vec{u} is a non-dimensional Cartesian velocity vector having the components $\vec{u} = (u, v, w)$, t is the non-dimensional time, p is the non-dimensional pressure, and ∇ is the standard three dimensional Cartesian gradient operator in non-dimensional coordinates x , y , and z . The above variables are made non-dimensional using a length scale \mathcal{L} , velocity scale \mathcal{U} , time scale \mathcal{T} , and pressure scale \mathcal{P} . This scaling produces a non-dimensional parameter the Reynolds Number, Re , which is defined as $Re = \mathcal{U}\mathcal{L}/\nu$, where ν is the kinematic viscosity. Furthermore, the time scale can be defined as $\mathcal{T} = \mathcal{L}/\mathcal{U}$, and the pressure scale as $\mathcal{P} = \rho\mathcal{U}^2$, where ρ is the density.

Since the governing partial differential equations are spatially elliptic, boundary conditions are required on all surfaces bounding the solution domain, for the variables u , v , and w . In the analytic formulation no boundary condition is required for pressure since it can be thought of as a Lagrange multiplier, and acts to keep the velocity solution divergence free. The numerical scheme implemented allows for complex domain geometries along with the application of several types of boundary conditions. In the discrete formulation utilized, a boundary condition on the pressure is required, therefore the analytic form of the discrete pressure boundary conditions will be noted (Gresho and Sani [16], Williams and Baker [52]). The boundary conditions applied to some of the various bounding surfaces of the computational domain are given in Equation 2.3.

$$\begin{aligned} \textit{Body} : \quad & u = 0, \quad v = 0, \quad w = 0, \quad \frac{\partial p}{\partial n} = 0 \\ \textit{Inflow} : \quad & u = c_1, \quad v = c_2, \quad w = c_3, \quad \frac{\partial p}{\partial n} = 0 \\ \textit{Far - Field} : \quad & \frac{\partial u}{\partial y} = 0, \quad v = 0, \quad w = 0, \quad \frac{\partial p}{\partial y} = 0 \\ & u = 0, \quad \frac{\partial v}{\partial x} = 0, \quad w = 0, \quad \frac{\partial p}{\partial x} = 0 \end{aligned} \quad (2.3)$$

The variable n in the above equation represents the direction normal to the bounding surfaces. A *Body* boundary surface represents a solid bounding surface on which the no slip, no penetration conditions are applied. An *Inflow* boundary is a boundary along which a prescribed velocity is specified, and the *Far-Field* condition is used for regions where the flow varies little in the surface normal direction. The first of the two equations for this condition is applied to horizontal boundaries which are parallel to the x directions. The second is applied to vertical boundaries, parallel to the

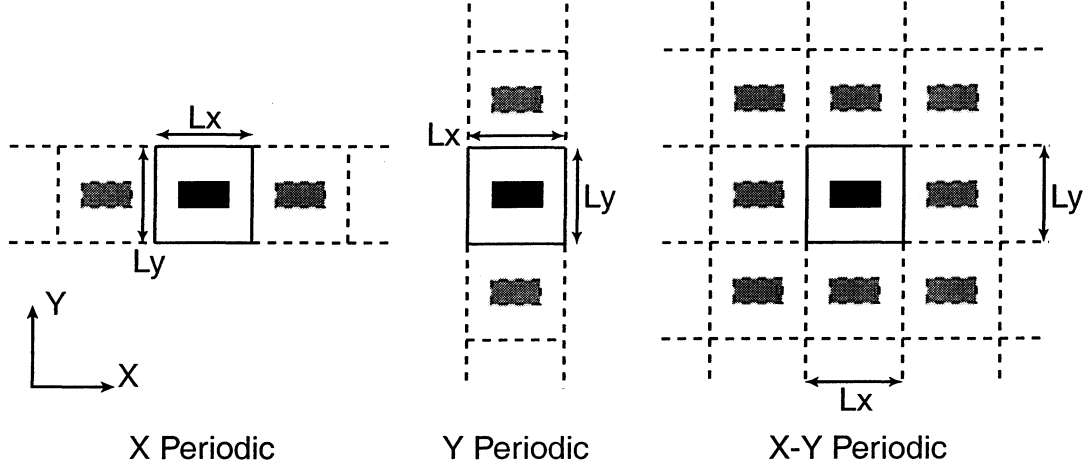


Figure 2.1: Periodic Geometries

y direction. All of the boundary conditions utilize a Neumann condition on pressure (Gresho and Sani [16], Williams and Baker [52]). Two additional boundary types have been defined, *Periodic* and *Outflow*, which require appropriate modification of the governing equations and are described in the two following sections.

2.2.2 Periodic Boundary Conditions

Periodic boundary conditions can be classified as one of two types: periodicity with translational invariance and periodicity without translational invariance. In the case of periodicity with translational invariance, a Fourier expansion along that direction with a uniform grid would be appropriate and no additional modifications to the governing equations are required. Periodicity without translational invariance is harder to handle, as a Fourier expansion is inappropriate in this case. The kind of problems we envision solving with this code are flow, and heat transfer, over an array of cylinders. The array is assumed to be periodic in x , y , or both as is shown in Figure 2.1, while the cylinder cross-section is assumed to be uniform along the third direction, z . In this case periodic boundary conditions with translational invariance are appropriate along the z direction. The domain of periodicity however must be carefully chosen. Along the x and y directions there is clear geometric periodicity, but the presence of cylinders breaks translational invariance.

From Figure 2.1 it can be seen that as a result of geometric periodicity a unit cell can be defined which repeats along the x and y directions. Geometric periodicity does not guarantee a periodic

flow with a period of one unit cell. A more general description of the flow would be to apply the following condition on the velocity field (Patankar, Liu, and Sparrow [38])

$$\textit{Periodic} : \vec{u}(x, y, z, t) = \vec{u}(x + mL_x, y + nL_y, z, t) \quad (2.4)$$

For periodicity over a single cell m and n are set equal to one. For x periodicity only, n is set to zero, and for only y periodicity, m is set to zero. A non periodic flow could be approximated with a large value of m and n . It is clear that computational cost will increase with increasing m and n . For simplicity we will restrict attention to the approximation $m = 1$ and $n = 1$.

A similar equation is needed for the pressure; however, in general the pressure will not be periodic. Whenever there is flow in a periodic direction the pressure will continuously drop in that direction. Therefore, to implement a periodic boundary condition a *modified pressure* is introduced, by removing the secular drift in pressure (Patankar, Liu, and Sparrow [38]). The pressure can be written as

$$p(x, y, z, t) = p_{in} - \beta_x x - \beta_y y + \tilde{p}(x, y, z, t) \quad (2.5)$$

In this equation p_{in} is an arbitrary inlet pressure value, and \tilde{p} is the modified pressure. The terms $\beta_x L_x$ and $\beta_y L_y$ represent linear pressure drops across the length of a cell, which account for the net pressure drop across the cell. The values chosen for β_x and β_y set the pressure gradient which drives the flow. The ratio β_x/β_y determines the direction of the driving pressure gradient and their magnitude sets the pressure scale, which in turn determines the velocity scale. With the net drop in pressure accounted for by the linear terms the modified pressure \tilde{p} becomes periodic and has the boundary equation

$$\textit{Periodic} : \tilde{p}(x, y, z, t) = \tilde{p}(x + mL_x, y + nL_y, z, t) \quad (2.6)$$

A result of the introduction of the modified pressure is that the governing equations 2.1 are modified

by the substitution of the pressure equation 2.5 to give

$$\frac{\partial \vec{u}}{\partial t} + \vec{u} \cdot \nabla \cdot \vec{u} = \vec{\beta} - \nabla \tilde{p} + \frac{1}{Re} \nabla^2 \vec{u} \quad (2.7)$$

where $\vec{\beta} = (\beta_x, \beta_y, 0)$. The values of β_x and β_y now appear as parameters in the Navier-Stokes equations, and serve to indirectly set the pressure, or velocity, scale. The relation between the β values and the pressure scale can be seen by examining the pressure drop between the same point in two neighboring cells.

$$\Delta p(L_x, L_y, 0, 0) = p(x, y, z, t) - p(x + L_x, y + L_y, z, t) = \beta_x L_x + \beta_y L_y \quad (2.8)$$

or

$$\mathcal{P} = \frac{\Delta p^*(L_x, L_y, 0, 0)}{\beta_x L_x + \beta_y L_y} \quad (2.9)$$

The * superscript denotes a physical variable. Unless otherwise stated, the value of $\beta_x = 1$ has been used with x periodic boundary conditions and $\beta_y = 0$ with y periodic conditions.

2.2.3 Outflow Boundary Condition

In the study of flow over bluff bodies it is often desirable to study the flow in a domain in which there exists a net influx and efflux of fluid. The bounding surfaces over which an inflow occurs are generally handled by prescribed velocity over the surface, which is sufficient provided the inflow condition is far enough upstream. This type of boundary condition is described in Section 2.2.1. The elliptic nature of the governing equations require a boundary condition for the velocity on all surfaces bounding the solution domain. However the velocity along the outflow boundaries can not generally be specified as it is greatly influenced by the flow inside the domain. Thus, a Dirichlet condition at the outflow boundary is not feasible. Furthermore, simple Neumann conditions, such as

$$\frac{\partial \vec{u}}{\partial x} = 0 \quad (2.10)$$

where x is the flow direction, have proven to be inadequate (Joslin et al. [23], Streett and Macaraeg [48]). This condition can result in the reflection of advecting flow structures at the outflow boundary, causing errors in the solution within the domain.

Instead, a more accurate implementation of the outflow boundary condition has been utilized (Joslin et al. [23], Streett and Macaraeg [48]). This approach involves the filtering of the streamwise (x) diffusion terms in the governing equations 2.1 to change the nature of the governing equations in the x direction at the outflow boundary from elliptic to parabolic. The diffusion operator in Equation 2.1 is redefined as

$$\nabla_f^2 = f(x) \frac{\partial^2}{\partial x^2} + \frac{\partial^2}{\partial y^2} + \frac{\partial^2}{\partial z^2} \quad (2.11)$$

and Equation 2.1 becomes

$$\frac{\partial \vec{u}}{\partial t} + \vec{u} \cdot \nabla \cdot \vec{u} = -\nabla p + \frac{1}{Re} \nabla_f^2 \vec{u} \quad (2.12)$$

The filter function, $f(x)$, is defined such that it has a value of one throughout most of the computational domain, and drops to zero as the outflow boundary is approached. The filter function used was defined as

$$\begin{aligned} f(x) &= 1 & x < x_b \\ f(x) &= \frac{\tanh(\varepsilon(x-x_c)) - \tanh(\varepsilon(x_e-x_c))}{\tanh(\varepsilon(x_b-x_c)) - \tanh(\varepsilon(x_e-x_c))} & x > x_b \end{aligned} \quad (2.13)$$

In this equation x_b is the x coordinate of the beginning of the attenuated region, x_c is the center, and x_e is the end. Figure 2.2 depicts a typical geometry and filter function. ε is a parameter used to control the steepness of the attenuation curve, here the value of ε was chosen to be 2.5. The governing equations 2.12 are applied at the outflow boundary where there is no longer an x diffusion term. The region of space over which the value of the filter function is not equal to one is referred to as the *buffer domain*. In this buffer region the character of the governing equations is altered to allow the flow to smoothly advect through the outflow boundary. Mittal and Balachandar [32] have used this boundary condition in the context of a cylindrical computational domain and show that vortices shed from the cylinder are smoothly advected out of the computational domain, without

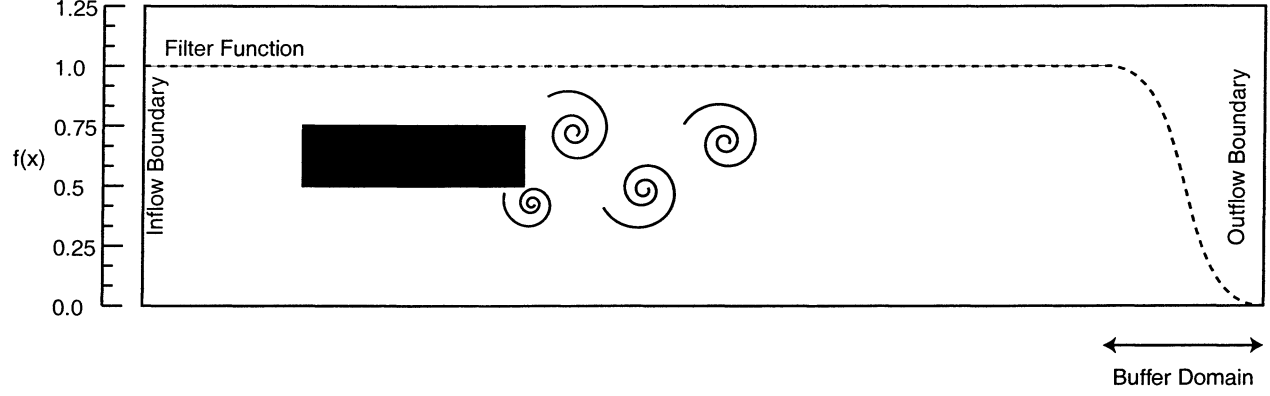


Figure 2.2: Outflow Filter and Buffer Domain

any spurious reflections at the outflow boundary.

2.3 Energy Equation

2.3.1 General

In addition to solving the Navier - Stokes equation we also consider the solution to the energy equation for incompressible flow having constant properties and no viscous dissipation. The energy equation has the form

$$\frac{\partial T}{\partial t} + \vec{u} \cdot \nabla T = \frac{1}{PrRe} \nabla^2 T \quad (2.14)$$

where T is the non-dimensional temperature field and Pr is the Prandtl number defined as $Pr = \nu/\alpha$, with α being the thermal diffusivity of the fluid. The same scalings used with the Navier - Stokes equations 2.1 and 2.2 are applied with the addition of a temperature scale, \mathcal{E} , and a heat flux scale, $\mathcal{Q} = k\mathcal{E}/\mathcal{L}$, where k is the thermal conductivity. Several types of boundary conditions, similar to those used for the Navier - Stokes equations, have been implemented.

Several basic boundary types have been defined, given by

$$\text{Temperature:} \quad T = c \quad (2.15)$$

$$\text{Flux:} \quad -\nabla T \cdot \vec{n} = q'' \quad (2.16)$$

$$\text{Far Field.} \quad \nabla T \cdot \vec{n} = 0 \quad (2.17)$$

An outflow condition has also been implemented to allow the solution of problems with non-periodic geometries. This condition is implemented using a buffer domain technique in the same manner as for the Navier - Stokes equations, which is described in section 2.2.3. The Laplace operator is redefined as shown in equation 2.11 and the energy equation becomes

$$\frac{\partial T}{\partial t} + \vec{u} \cdot \nabla T = \frac{1}{PrRe} \nabla_f^2 T \quad (2.18)$$

2.3.2 Periodic Boundary Condition

Implementation of the periodic boundary conditions for temperature involves many of the same issues that occurred in handling the pressure. Applying the same technique, the secular increase or decrease in temperature is removed and the total temperature is written in terms of a modified temperature as

$$T(x, y, z, t) = T_{in} + \gamma_x x + \gamma_y y + \Theta(x, y, z, t) \quad (2.19)$$

where Θ is the modified temperature. Substituting the above equation into the energy equation 2.14 produces

$$\frac{\partial \Theta}{\partial t} + \vec{u} \cdot \nabla \Theta = -(u\gamma_x + v\gamma_y) + \frac{1}{PrRe} \nabla^2 \Theta \quad (2.20)$$

A periodic boundary condition for Θ of the form

$$\Theta(x, y, z, t) = \Theta(x + mL_x, y + nL_y, z, t) \quad (2.21)$$

may be applied if the proper values of γ_x and γ_y are used. These values determine the net temperature increase across a periodic cell in the x and y directions respectively. The values of these parameters must be consistent with the rate at which energy is added to a cell and convected from it. To insure this condition is met, a first-law control volume analysis may be performed on a cell,

which yields the relation

$$\gamma_y L_y \bar{Q}_y + \gamma_x L_x \bar{Q}_x = \frac{1}{PrRe} \int \int_S \vec{q}'' \cdot \vec{n} da \quad (2.22)$$

\bar{Q}_x and \bar{Q}_y are the volumetric flow rates through a cell in the x and y directions. The integral is over all the internal surfaces within a cell over which there is a heat flux \vec{q}'' . The first two terms in equation 2.22 are the net rate at which energy is advected from a cell in the x and y directions, while the last term is the rate at which energy enters the cell through the internal surfaces. It is further necessary to insure that the net advection of energy from a cell is in a direction consistent with the bulk fluid motion. If the average temperature in each cell, \bar{T} , is calculated, its gradient can be found as

$$\nabla \bar{T} = \gamma_x \hat{i} + \gamma_y \hat{j} \quad (2.23)$$

The bulk fluid velocity is given by

$$\vec{u} = \frac{\bar{Q}_x}{L_y L_z} \hat{i} + \frac{\bar{Q}_y}{L_x L_z} \hat{j} \quad (2.24)$$

The requirement that the direction of these two vector quantities be the same produces the relation

$$\gamma_x \bar{Q}_y L_y = \gamma_y \bar{Q}_x L_x \quad (2.25)$$

which when combined with equation 2.22 gives the following relations for γ_x and γ_y

$$\gamma_x = \frac{q_{net} \bar{Q}_x L_x}{PrRe \left[(\bar{Q}_y L_y)^2 + (\bar{Q}_x L_x)^2 \right]} \quad (2.26)$$

$$\gamma_y = \frac{q_{net} \bar{Q}_y L_y}{PrRe \left[(\bar{Q}_y L_y)^2 + (\bar{Q}_x L_x)^2 \right]} \quad (2.27)$$

where

$$q_{net} = \int \int_S \vec{q}'' \cdot \vec{n} da \quad (2.28)$$

The use of the periodic boundary condition for temperature imposes certain limitations on the type of flows that may be solved. Equations 2.26 and 2.27 were developed assuming the net amount of energy in a cell remains constant, and equation 2.20 ignores any temporal variation in the values of γ_x and γ_y . Furthermore, under this formulation it is necessary that all internal boundaries have a constant heat flux boundary condition.

2.4 Temporal Discretization

This section details the temporal discretization employed for both the Navier - Stokes and Energy equations. The discretization of the Navier - Stokes equations is discussed, with the same method applied to the Energy equation. The Navier - Stokes equations, in their most general form for this work, are

$$\frac{\partial \vec{u}}{\partial t} + \vec{u} \cdot \nabla \cdot \vec{u} = \vec{\beta} - \nabla \tilde{p} + \frac{1}{Re} \nabla_f^2 \vec{u} \quad (2.29)$$

$$\nabla \cdot \vec{u} = 0 \quad (2.30)$$

where $\vec{\beta}$ is defined in Section 2.2.2 and ∇_f^2 is defined in Section 2.2.3. This general form includes the modifications for periodic and outflow boundary conditions. If no periodic boundary conditions are used the value of $\vec{\beta}$ may be set to $\vec{\beta} = (0, 0, 0)$ and the modified pressure, \tilde{p} , becomes identical to the standard pressure. Similarly, if an outflow boundary condition is not utilized the filter function, $f(x)$, has the value $f(x) = 1$ through out the computational domain and ∇_f^2 becomes the standard Laplace operator ∇^2 .

The temporal discretization is performed using a general two-step time split scheme (Chorin [7], Kim and Moin [25]). In this scheme an intermediate velocity field, \vec{u}^* , is calculated using the advection, diffusion, and linear pressure drop terms in equation 2.29 according to the following

equation:

$$\frac{\vec{u}^* - \vec{u}^n}{\Delta t} + NL = LP + \frac{1}{Re} DIF \quad (2.31)$$

The term NL represents the explicitly discretized nonlinear term using a third order Adams - Bashforth scheme and is given by

$$NL = \frac{23}{12} (\vec{u}^n \cdot \nabla \vec{u}^n) - \frac{16}{12} (\vec{u}^{n-1} \cdot \nabla \vec{u}^{n-1}) + \frac{5}{12} (\vec{u}^{n-2} \cdot \nabla \vec{u}^{n-2}) \quad (2.32)$$

LP is the linear pressure drop coefficients discretized using Crank - Nicholson giving

$$LP = \frac{1}{2} \vec{\beta}^{n+1} + \frac{1}{2} \vec{\beta}^n \quad (2.33)$$

and DIF is the implicitly discretized diffusion term also using Crank - Nicholson, giving

$$DIF = \frac{1}{2} \nabla_f^2 \vec{u}^* + \frac{1}{2} \nabla_f^2 \vec{u}^n \quad (2.34)$$

Due to the missing pressure term the intermediate velocity, \vec{u}^* , will not be divergence free. The second step of the time split scheme corrects the velocity field by making it divergence free through the action of the pressure term. This is done using the equations

$$\frac{\vec{u}^{n+1} - \vec{u}^*}{\Delta t} = -\nabla \tilde{p}^{n+1} \quad (2.35)$$

$$\nabla \cdot \vec{u}^{n+1} = 0 \quad (2.36)$$

which when combined produce the Pressure Poisson equation

$$\nabla^2 \tilde{p}^{n+1} = \frac{1}{\Delta t} \nabla \cdot \vec{u}^* \quad (2.37)$$

The advancement of the solution from \vec{u}^n to \vec{u}^{n+1} requires first the solution of equation 2.31 for the intermediate velocity, \vec{u}^* , followed by the solution of equation 2.37 for the pressure at the new

time, \tilde{p}^{n+1} , and finally the use of equation 2.35 to compute the new velocity, \vec{u}^{n+1} .

2.5 Spatial Discretization

The temporal discretization described in Section 2.4 results in a set of elliptic partial differential equations in spatial variables. Equations 2.31 and 2.37 both have the general form

$$\left(f(x) \frac{\partial^2}{\partial x^2} + \frac{\partial^2}{\partial y^2} + \frac{\partial^2}{\partial z^2} - \sigma \right) g(x, y, z) = h(x, y, z) \quad (2.38)$$

For equation 2.31 the term g is the intermediate velocity \vec{u}^* and $\sigma = 2Re/\Delta t$. For equations 2.37 g is the modified pressure \tilde{p}^{n+1} and $\sigma = 0$. With $\sigma = 0$ equation 2.38 changes from a Helmholtz to a Poisson equation.

The numerical solution of the above equation requires that it be discretized in the three spatial dimension x, y , and z . The requirements placed on the spatial discretization where that it posses a high degree of accuracy, handle moderately complex geometry, readily adapt to new geometries, and implement efficiently on parallel computer architectures. To meet these requirements a multi-domain spectral element discretization was chosen for the x and y directions, while a Fourier discretization was used for the z direction.

2.5.1 Fourier Discretization

The geometries to be analyzed all have a uniform x, y plane cross-section which extends infinitely in the z direction. This makes discretization by Fourier expansion in the z direction a natural choice. The forward and inverse Fourier transforms are given by

$$\hat{g}_k(x, y) = \frac{1}{L_z} \int_0^{L_z} g(x, y, z) e^{-i \frac{kz2\pi}{L_z}} dz \quad (2.39)$$

and

$$g(x, y, z) = \sum_{k=-\infty}^{\infty} \hat{g}_k(x, y) e^{i \frac{kz2\pi}{L_z}} \quad (2.40)$$

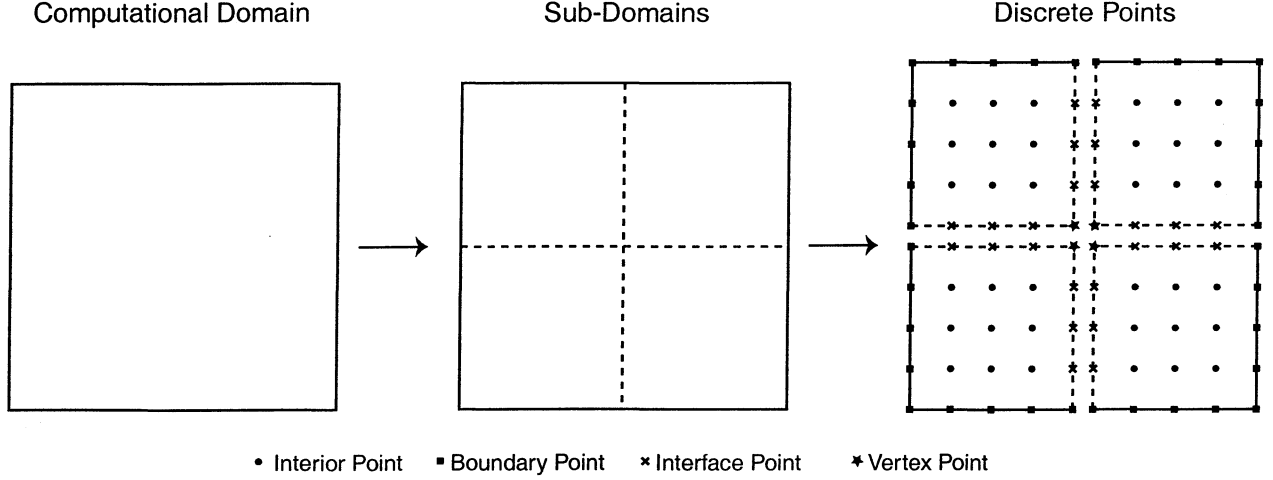


Figure 2.3: Multi Domain Discretization

k is the wavenumber of the Fourier mode, and L_z is the largest periodic wavelength in the z direction. Applying the expansion 2.40 to equation 2.38 produces

$$\left[f(x) \frac{\partial^2}{\partial x^2} + \frac{\partial^2}{\partial y^2} - \left(\sigma + \frac{k^2 4\pi^2}{L_z^2} \right) \right] \hat{g}_k(x, y) = \hat{h}_k(x, y) \quad (2.41)$$

where \hat{g}_k and \hat{h}_k are the Fourier coefficients after the z transform. The above equation is a two dimensional Helmholtz equation in x and y that may be solved by discretizing in those variables.

2.5.2 Multi-Domain Spectral Discretization

The spatial discretization in x and y is performed using a spectral multi-domain technique (Furnaro [15], Streett and Macaraeg [48], Carlenzoli and Gervasio [6]). In this technique the overall computational domain is subdivided into a number of smaller rectangular subdomains, as shown in Figure 2.3. Within each sub-domain a local spectral Chebyshev discretization is defined (Canuto et al. [5]). The discrete approximation of derivatives at each point in a domain utilizes only points within the same domain. The multi-domain discretization produces several distinct classes of points, as detailed in Figure 2.3. *Interior* points lie inside a sub-domain. *Boundary* points lie along a sub-domain edge at which a boundary condition is being applied, while *Interface* points lie along edges at the interface between two subdomains. Finally, *Vertex* points are points joining four subdomains.

For each point produced by the discretization a discretized equation must be applied. At *Interior* points the discrete collocated form of the governing equation is used. For *Boundary* points a discrete form of the appropriate analytic boundary condition is applied. The equations applied at the *Interface* and *Vertex* points are referred to as the patching equations. The governing second order elliptic equations require a patching condition which enforces either strong or weak C^1 continuity. For either patching method spectral convergence of the solution with increasing order of the basis function is achieved (Canuto et al. [5]).

The strong formulation requires continuity of the function and its normal derivative between two domains at *interface* points. Thus the following equations are applied for *interface* points, depending on the orientation of the *interface* edge

$$\text{Vertical Interface: } \frac{\partial \hat{g}_k^1(x,y)}{\partial x} - \frac{\partial \hat{g}_k^2(x,y)}{\partial x} = 0 \quad (2.42)$$

$$\text{Horizontal Interface: } \frac{\partial \hat{g}_k^1(x,y)}{\partial y} - \frac{\partial \hat{g}_k^2(x,y)}{\partial y} = 0 \quad (2.43)$$

The superscripts 1 and 2 denote the two different domains on either side of the *interface* edge. Identical equations can be written for the *vertex* points, where continuity of the function and its derivatives are also desired. However, only one derivative matching equation, either along x or along y , can be applied at each *vertex* point; therefore, continuity of the derivative along the other direction cannot be enforced. In practice the derivative mismatch in the unenforced direction is generally small and decreases exponentially as the discretization is refined. Furthermore, the solution at the vertex points is decoupled from the solution at the *interior* and *boundary* points, thus mismatch at the *vertex* points has no impact on the overall solution.

An alternative to the strong formulation is the weak formulation where the patching equations involve a combination of flux matching and enforcement of the governing equation. The collocation of the governing equations at the *interior* points and the handling of the boundary conditions remains the same as for the strong formulation. However, the patching equations are obtained from the variational formulation of the equations. For the weak form, at an interface, the following

equation is applied

$$\frac{\partial \hat{g}_k^1}{\partial n} - \frac{\partial \hat{g}_k^2}{\partial n} - \left(L \hat{g}_k^1 - \hat{h}_k \right) \omega_n^1 - \left(L \hat{g}_k^2 - \hat{h}_k \right) \omega_n^2 = 0 \quad (2.44)$$

where the operator L is defined as

$$L = \left[f(x) \frac{\partial^2}{\partial x^2} + \frac{\partial^2}{\partial y^2} - \left(\sigma + \frac{k^2 4\pi^2}{L_z^2} \right) \right] \quad (2.45)$$

n is the direction normal to the interface, and w_n^1 and w_n^2 are the proper Gauss - Lobatto quadrature weights as defined by Funaro [15]. Unlike the strong formulation, for the weak form, a well defined equation exists for the interface vertices. The vertex equation is a generalized form of equation 2.44 where weighted derivatives in the x and y directions and the collocated governing equations from the four surrounding domains are included. The weak form provides greater accuracy, while the strong formulation allows for easier implementation. For this work the strong formulation was chosen, but with minor modifications the weak form may be used.

Application of the multi-domain discretization produces a linear set of equations having the form

$$\begin{bmatrix} A_1 & 0 & \cdots & 0 & B_1 \\ 0 & A_2 & \cdots & 0 & B_2 \\ \vdots & \vdots & \ddots & \vdots & \vdots \\ 0 & 0 & \cdots & A_M & B_M \\ C_1 & C_2 & \cdots & C_M & D \end{bmatrix} \begin{Bmatrix} \mathbf{x}_1 \\ \mathbf{x}_2 \\ \vdots \\ \mathbf{x}_M \\ \mathbf{y} \end{Bmatrix} = \begin{Bmatrix} \mathbf{f}_1 \\ \mathbf{f}_2 \\ \vdots \\ \mathbf{f}_M \\ \mathbf{f}_{M+1} \end{Bmatrix} \quad (2.46)$$

where \mathbf{x}_i is an ordered vector of *interior* points for sub-domain i , M is the number of domains, and \mathbf{y} is an ordered vector of the *interface* and *vertex* points. The i th block row of the above equation enforces the discrete collocated form of the governing equations at all the interior points in the i th sub-domain. Thus the first M block rows of equation 2.46 complete the enforcement of the discrete version of equation 2.41 at all the interior points. The last block row of equation 2.46 enforces the interface and vertex matching conditions. Therefore matrices A and B are block matrices whose terms are generated by the discrete governing and boundary equations, while C and D result from

the interface and vertex equations. The particular form of this linear system lends itself to solution through an influence matrix technique, which is detailed in the following section.

2.6 Influence Matrix Method

Of critical importance to any numerical solution methodology is its efficiency, both in terms of CPU utilization and memory usage. A direct solution of the linear system of equations 2.46 would require the inversion of a matrix of approximate size $(N_x N_y M) \times (N_x N_y M)$, where N_x and N_y are the number of grid points in each domain along the x and y directions and M is the number of domains. One such system must be solved for each of the real and imaginary components of the $N_z/2$ number of Fourier modes along the z directions. This type of direct solution would fail to take advantage of the sparsity and structure of the matrix. A more efficient technique for solving the linear system of equations 2.46, referred to as the Influence Matrix Method, exploits the structure of the matrix (Quarteroni and Sacchi-Landriani [40] [41]). This technique performs the solution of the system of equations 2.46 in several steps.

In the first step, the Particular solution, is evaluated by assuming an arbitrary vector of unknown *interface* and *vertex* values \mathbf{y} . With \mathbf{y} a given value the first M block rows of equation 2.46 decouple and may be solved independently. For $\mathbf{y} = 0$, each of the first M block rows produces the equation

$$\tilde{\mathbf{x}}_i = A_i^{-1} \mathbf{f}_i \quad (2.47)$$

This is equivalent to solving the Helmholtz problem locally and independently in each sub-domain with the *interface* and *vertex* points associated with each domain having a value of zero. The method of solving the Helmholtz problem on an individual sub-domain is detailed in section 2.7.

The second step in the solution involves the calculation of the residual, \mathbf{r} , which is the derivative mismatch at the *interface* and *vertex* points for the Particular solution, and the solution of the Influence equation for the *interface* - *vertex* vector, \mathbf{y} . The residual is calculated from the equation

$$\mathbf{r} = \mathbf{f}_{M+1} - \sum_{i=1}^M C_i \tilde{\mathbf{x}}_i \quad (2.48)$$

and is then used as the right hand side in the influence equation

$$G\mathbf{y} = \mathbf{r} \quad (2.49)$$

where G is the influence matrix, which is defined as

$$G = \left[D - \sum_{i=1}^M C_i A_i^{-1} B_i \right] \quad (2.50)$$

Equations 2.48 - 2.50 can be derived by solving the first M block rows of equation 2.46 for \mathbf{x}_i in terms of \mathbf{y} , substituting for \mathbf{x}_i in the last block row equation, and using the definition of the Particular solution 2.47.

The influence matrix, G , is defined above in terms of block sub-matrices. However, in practice this definition is neither convenient nor practical. As an alternative, the influence matrix may be constructed on a column-by-column basis. This can be seen by examining the results of multiplying the influence matrix with the j th column of the identity matrix, I_j .

$$G_j = GI_j = \left[D - \sum_{i=1}^M C_i A_i^{-1} B_i \right] I_j \quad (2.51)$$

$$= \sum_{i=1}^M C_i \mathbf{x}_i^j + DI_j \quad (2.52)$$

Here G_j is the j th column of the influence matrix, and \mathbf{x}_i^j is the solution in sub-domain i for the Helmholtz equation with zero forcing, zero boundary condition, and all *interface - vertex* values set to zero, except for the j th *interface - vertex* point which is set to one. The j th influence matrix column is then an evaluation of the derivative mismatch at each *interface - vertex* point for this Helmholtz equation solution. In this manner each column of the Influence Matrix is computed and assembled to form the complete matrix, G .

Once the *interface - vertex* values, \mathbf{y} , have been calculated by solving the Influence equation the third and final step in the solution of equation 2.46 is the calculation of the Homogeneous solution

given by

$$\bar{\mathbf{x}}_i = -A_i^{-1}B_i\mathbf{y} \quad (2.53)$$

This is the solution of the Helmholtz equation in each sub-domain for zero forcing, zero boundary constants, and the *interface* and *vertex* points having their proper values, as obtained from the solution of equation 2.49. The final solution is then the sum of the Particular and Homogeneous solutions

$$\mathbf{x}_i = \tilde{\mathbf{x}}_i + \bar{\mathbf{x}}_i \quad (2.54)$$

along with the *interface* - *vertex* values, \mathbf{y} .

Overall, the Influence Matrix technique requires two solutions of a Helmholtz equation for each sub-domain. One for the Particular solution, equation 2.47, and the other for the Homogeneous solution, equation 2.53. In addition, it requires the solution of the Influence matrix problem; however, this need only involve a simple matrix vector product, since the influence matrix may be precomputed and inverted once at the outset.

A difficulty arises in the inversion of the influence matrix utilized in solving the pressure Poisson problem. As posed, the equation for pressure is a Poisson equation with a Neumann condition on the boundaries. The solution of this system of equations is indeterminate to an arbitrary additive constant. The discrete linear system for this problem, therefore, cannot be solved through direct inversion of the influence matrix since its condition number is infinite, and correspondingly the matrix has a null eigen mode. The solution of the linear system can be determined, with the arbitrary constant set to zero, through an eigen decomposition of the influence matrix and elimination of the null mode. The influence matrix may be eigen decomposed as

$$G = V\Lambda V^{-1} \quad (2.55)$$

where V is a matrix composed of the eigenvectors of G and Λ is a diagonal matrix of eigenvalues.

The inverse of G may then be calculated as

$$G^{-1} = V\Lambda^{-1}V^{-1} \quad (2.56)$$

Since Λ is a diagonal matrix its inverse simply contains the inverted diagonal elements. The eigenvalue of the null mode is zero and its eigenvector is a constant. The inverse of the influence matrix, as defined by equation 2.56, may be determined by setting the inverted null mode eigenvalue in Λ^{-1} equal to zero. This allows the linear system to be solved with the unknown constant value set to zero.

The advantage to the influence matrix technique lies in the fact that it reduces a single large problem into many much smaller problems. The solutions to the Particular and Homogeneous problems may be performed independently in each sub-domain using the fast Helmholtz solver algorithm detailed in the following section. This domain-wise independence allows for very efficient implementation under parallel architectures, since each sub-domain may be handled independently by a different processor. Communication amongst processors only occurs when solving the influence matrix equation. This communication is limited to collecting the components of the residual vector and distributing the solution for the *interface - vertex* points across the processors. Furthermore, the Influence Matrix technique greatly reduces overall memory usage since a single large solution matrix is never formed. The largest remaining matrix, the influence matrix, is generally an order of magnitude smaller in size.

2.7 Sub-domain Solver

Through the use of the Influence Matrix technique the problem of determining the solution to the set of governing equations over the entire computational domain is essentially reduced to multiple solutions of a Helmholtz or Poisson problem in each sub-domain. The efficiency with which the solution in each sub-domain is calculated, therefore, has a significant impact on the overall performance of the numerical implementation. A Fast Helmholtz Solution algorithm has been implemented to provide highly efficient solution of the sub-domain problems.

The sub-domain problem involves solving a Helmholtz or Poisson equation in the form of Equa-

tion 2.41 over a rectangular domain with a generally mixed set of Dirichlet and Neumann boundary conditions applied to the four boundaries. Each sub-domain is discretized into $Nx \times Ny$ collocation points. At the interior points a discrete form of the governing equation is applied, and similarly at the boundaries a discrete form of the appropriate boundary condition is used. This produces a linear system of $(Nx \cdot Ny) \times (Nx \cdot Ny)$ equations. The discrete equations at the interior points have the form

$$\sum_{l=1}^{Nx} DX_{(i,l)}^2 \hat{g}_{k(l,j)} + \sum_{l=1}^{Ny} \hat{g}_{k(i,l)} DY_{(l,j)}^2 - \left(\sigma + \frac{k^2 4\pi^2}{L_z^2} \right) \hat{g}_{k(i,j)} = \hat{h}_{k(i,j)} \quad \begin{cases} i=2 \rightarrow Nx-1 \\ j=2 \rightarrow Ny-1 \end{cases} \quad (2.57)$$

while at a boundary in the x direction the equations are

$$\text{or} \quad \begin{cases} \hat{g}_{k(i,j)} = c_{(i,j)} \\ \sum_{l=1}^{Nx} DX_{(i,l)}^2 \hat{g}_{k(l,j)} = c_{(i,j)} \end{cases} \quad \begin{cases} i=1, Nx \\ j=2 \rightarrow Ny-1 \end{cases} \quad (2.58)$$

and for a y boundary

$$\text{or} \quad \begin{cases} \hat{g}_{k(i,j)} = c_{(i,j)} \\ \sum_{l=1}^{Ny} \hat{g}_{k(i,l)} DY_{(l,j)}^2 = c_{(i,j)} \end{cases} \quad \begin{cases} i=2 \rightarrow Nx-1 \\ j=1, Ny \end{cases} \quad (2.59)$$

In the equations above DX^2 and DY^2 are respectively $Nx \times Nx$ and $Ny \times Ny$ discrete second derivative matrices (Canuto et al. [5]) and $c_{(i,j)}$ is the boundary condition value applied at the point i, j .

The set of equations above may be solved as a simple linear system of the form, $Ax = b$, where x is the entire list of unknown values and the operator, A , is of size $(NxNy \times NxNy)$, but sparse. However an alternative solution method, the Fast Helmholtz Solver, may be utilized to reduce the number of operations and the amount of memory required to produce the solution. As the first step in the implementation of the Fast Helmholtz Solver, the system of equations is reduced through the elimination of the boundary equations and unknown solution values on the boundary. This is accomplished by combining equations 2.58 and 2.59 with equation 2.57 to produce a system of

equations of the form

$$D\tilde{X}^2\tilde{g}_k + \tilde{g}_k D\tilde{Y}^2 - \tilde{\sigma}\tilde{g}_k = \tilde{h}_k \quad (2.60)$$

\tilde{g}_k is the reduced solution matrix containing only interior point values of \hat{g}_k and therefore of size $(Nx - 2) \times (Ny - 2)$. Similarly \tilde{h}_k is the interior portion of \hat{h}_k of size $(Nx - 2) \times (Ny - 2)$ modified by the incorporation of the boundary condition equations. $D\tilde{X}^2$ and $D\tilde{Y}^2$ are reduced second derivative matrices of sizes $(Nx - 2) \times (Nx - 2)$ and $(Ny - 2) \times (Ny - 2)$ which have been modified by the incorporation of the boundary equations. Finally, $\tilde{\sigma}$ is a redefined constant, $\tilde{\sigma} = \sigma + k^2 4\pi^2 / L_z^2$.

The system of equations in equation 2.60 may be solved efficiently through the eigen decomposition of the reduced derivative matrices $D\tilde{X}^2$ and $D\tilde{Y}^2$. These matrices may be written as

$$D\tilde{X}^2 = M\Lambda_x M^{-1} \quad (2.61)$$

$$D\tilde{Y}^2 = N\Lambda_y N^{-1} \quad (2.62)$$

where M and N are matrices whose columns are the eigenvectors of $D\tilde{X}^2$ and $D\tilde{Y}^2$ respectively, and Λ_x and Λ_y are a diagonal matrices containing the corresponding eigenvalues. Using the definitions

$$\tilde{g}_k = MGN^{-1} \quad (2.63)$$

$$\tilde{h}_k = MHN^{-1} \quad (2.64)$$

and the decompositions 2.61 and 2.62 allows the system of equations 2.60 to be solved for \hat{G} as

$$G_{(i,j)} = \frac{H_{(i,j)}}{\Lambda_{x(i,i)} + \Lambda_{y(j,j)} - \tilde{\sigma}} \begin{cases} i=1 \rightarrow Nx-2 \\ j=1 \rightarrow Ny-2 \end{cases} \quad (2.65)$$

The final solution on the sub-domain interior points, \tilde{g}_k , may then be computed from Equation 2.63, after which the solution at the boundary points may be determined from equations 2.58 and 2.59.

The advantage of the Fast Helmholtz algorithm is that once the eigen decomposition, which can be done once at the outset, has been performed the number of operations to obtain the solution

scale as $O(Nx^2Ny + NxNy^2)$ and the required storage involves only $Nx \times Nx$, $Ny \times Ny$, and $Nx \times Ny$ matrices. The alternative direct solution technique would require $O(Nx^2Ny^2)$ operations, assuming initial inversion of the solution matrix, and storage of an $NxNy \times NxNy$ matrix for each sub-domain. As a consequence the Fast Helmholtz algorithm produces a substantial improvement in operation and memory cost over the direct solution method.

2.8 Program Features

The choice and implementation of the algorithms described in this chapter was done with the intent of producing a computer code which is highly accurate, efficient, and flexible. The spectral multi-domain technique provides a highly accurate spatial discretization. It shares the characteristics of a single domain spectral method in that it provides high resolution at a given level of discretization and has a spectral, or exponential, rate of convergence to the exact solution as the discretization is increased. The use of the multi-domain technique along with the Influence Matrix method, and the Fast Helmholtz solver allow for efficient solution of the discrete problem. Memory utilization and operation count is reduced by converting the discrete linear equations from a single large matrix equation to many smaller sets of equations. Matrix size then scales with the square of the sub-domain discretization, as opposed to the square of the complete computational domain discretization. Virtually all computational operations are performed on a sub-domain-wise basis utilizing only data local to that sub-domain. This allows the code to run efficiently under parallel architectures, which at present are the dominant architectures for high performance computing. On multi-processor machines, each processor handles an equal number of domains, with near perfect scalability to the point where a single processor handles only a single domain. The code has shown near linear speedup for a properly optimized parallel implementation of the algorithm (Joseph [21]).

For the present work, an important consideration was the flexibility of the implementation. It was important that the implemented code be capable of solving a range of problems containing different geometries and utilizing different boundary conditions. With the multi-domain algorithm, it is possible to implement the code in a way that allows for easy reconfiguration of the geometry within the computational domain. Given a rectangular computational domain the number and size of the subdomains can easily be set by specifying a set of horizontal dividers spaced along

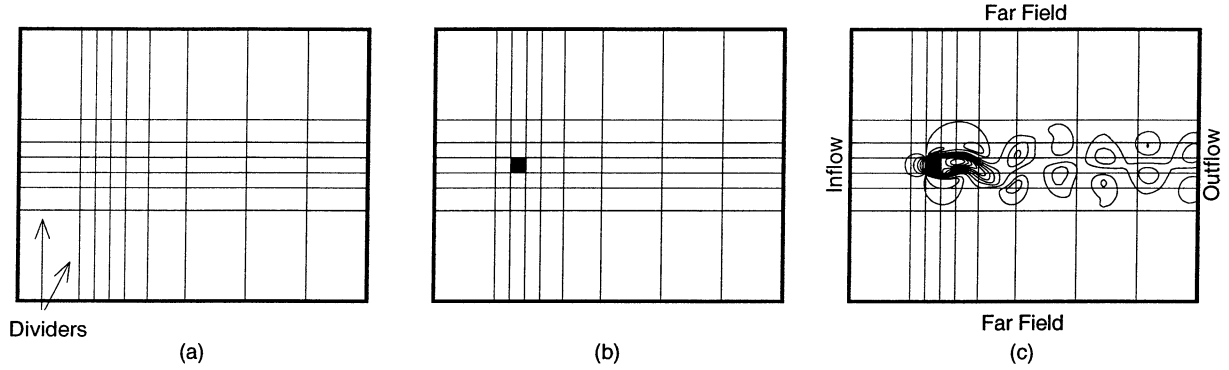


Figure 2.4: Discretization and Solution of Isolated Rectangular Cylinder

the y axis along with a group of vertical dividers along the x axis. This defines an initial grid for partitioning the computational domain into subdomains as shown in Figure 2.4 (a). Once the basic subdomains are defined the interior geometry can be specified by removing subdomains and specifying one of the different velocity or temperature boundary conditions defined earlier along their periphery, as shown in Figure 2.4 (b). Finally, the boundary conditions along the border of the computational domain may be set to be either a solid wall, inflow, outflow, periodic, or far field condition. Figure 2.4 (c) shows the solution to a case with inflow, outflow, and far field conditions, while Figure 2.5 shows the solution for a fully periodic case. The existing code may also be readily reconfigured to handle a wide range of problem cases, such as simple channel flow, channel flow with rectangular irregularities along the channel walls, channel flow with interior objects, or flow about more general shaped bluff bodies such as T or L shaped objects. At present the principal restriction on the geometry is that the subdomains must be rectangular. More general four sided curvilinear domains may also be handled within the general framework outlined above, with the only major modification required in the sub-domain Helmholtz solver.

With simple modifications the code can be adapted to handle an even broader range of problems. Yoon [56] has performed modifications that allow the solution of problems in cylindrical coordinates. The modified code has been applied to solving the flow in a mixing tank stirred by a Rushton turbine blade, show in Figure 2.6. Each vertical cross section about the tanks center line is rectangular and has the applied boundary conditions shown in Figure 2.6. The physical turbine blade itself is not modeled, but instead a theoretical model of the blade tip velocity is applied along an edge

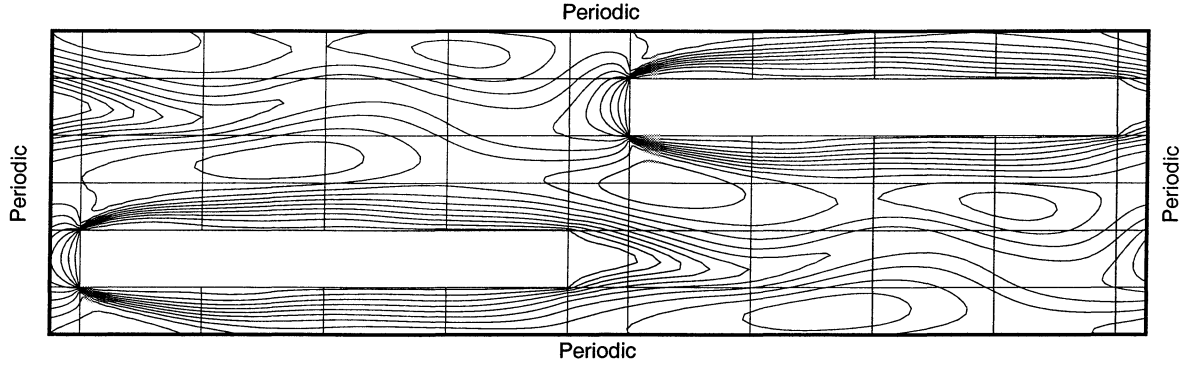


Figure 2.5: Discretization and Solution for a Periodic Array of Staggered Bodies

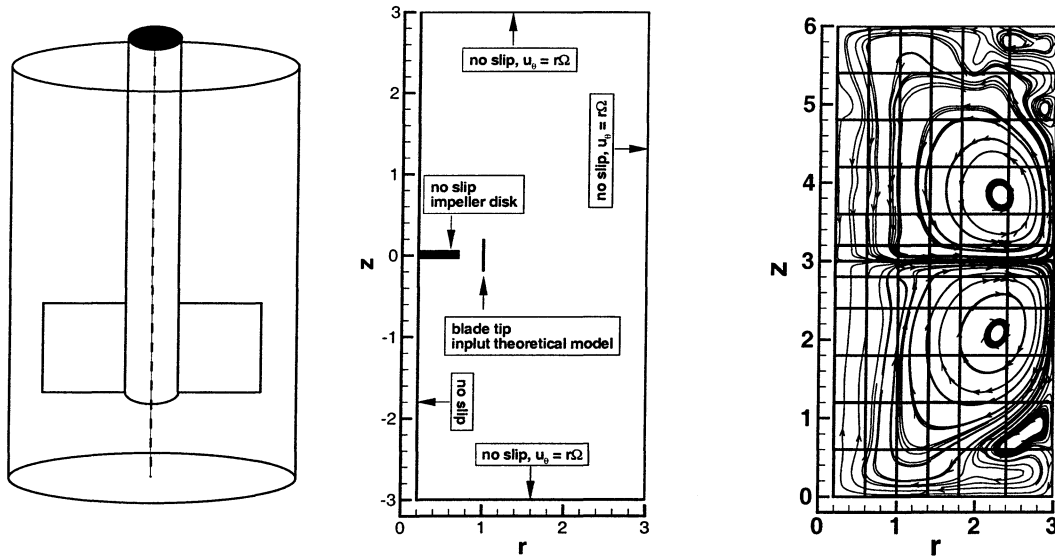


Figure 2.6: Simulation of Mixing Tank with Rushton Turbine Blade

between subdomains just beyond the physical location of the tip of the blade. The ability to apply boundary conditions along edges between subdomains is a feature of the original code that allows the specification of the velocity along lines within the computational domain. Figure 2.6 shows the multi-domain discretization for a cross section, along with the stream lines of the solution.

Another problem for which the present code has been used is the case of buoyant thermal convection between parallel plates with an internal isothermal body. Here a Boussinesq approximation has been used to model the buoyancy induced flow. The geometry is shown in Figure 2.7. In this model the upper and lower walls are isothermal with a temperature of $T = 1$ and $T = 0$, respectively. A periodic boundary condition is applied on the left and right boundaries, modeling

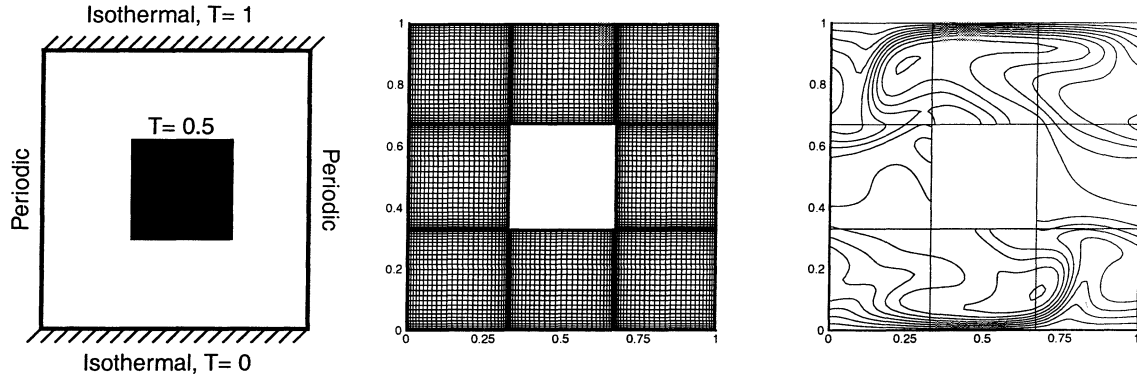


Figure 2.7: Convection Simulation

the case of an infinitely periodic array of square isothermal bodies placed between a hot lower, and a cold upper plate. Figure 2.7 shows the discretization used, along with the streamlines of the solution for the case when the rectangular object in the center is isothermal with a temperature of $T = 0.5$.

Chapter 3

Code Validation

3.1 Introduction

In this chapter the proper operation of the multi-domain spectral element code described in Chapter 2 is verified. The flow and temperature solutions produced by the present code will be evaluated by comparisons to two sets of independent numerical solutions. The first test case will compare to the results of Zhang [60] for flow through an infinite array of rectangular bodies in a staggered arrangement utilizing periodic boundary conditions. The second test case will compare to the results of Robichaux [42] for uniform flow over a square cylinder using inflow and outflow boundary conditions. The multi-domain code, as implemented, is capable of solving three dimensional problems; however, the cases considered in this chapter and throughout the rest of the text are two dimensional, since three dimensional effects play only a limited role for the Reynolds number range of interest. The following sections detail the results of these comparisons and demonstrate good agreement between the results of the present code and the test cases considered.

3.2 Infinite Staggered Array

This section compares the results from the present code with those of Zhang [60] for pressure driven flow through an infinite array of offset rectangular bodies. The basic geometry and associated parameters are shown in Figure 3.1, this is later referred to as the Staggered 1 case. To model an infinite geometry a basic periodic geometry or cell is defined, shown by the dotted lines in Figure 3.1, and periodic boundary conditions are applied along its boundary. The basic periodic

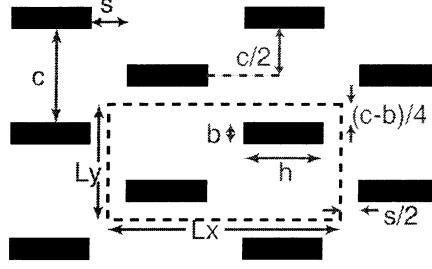


Figure 3.1: Staggered Array Geometric Parameters

b	0.75
h	6.41
s	0.79
c	3.25
Lx	14.4
Ly	4.0
X Bnd.	Per.
Y Bnd.	Per.
M	58
Nx	20
Ny	14
β_x	1.0
β_y	0.0

Table 3.1: Staggered 1 Parameter Values

cell can be seen to be composed of two rectangular bodies in a staggered formation. Repetition of the periodic cell produces an array of infinite extent in which every column of bodies is offset in the transverse direction from the column upstream.

The specific values of the parameters defining the test case are listed in Table 3.1. The discretization chosen produces 58 subdomains, each having 20 grid points in the x direction and 14 in the y . The discretization is shown in Figure 3.2. Periodic boundary conditions are employed on each edge and a fixed streamwise pressure gradient is imposed to drive the flow with $\beta_x = 1.0$.

With the value of β_x set to 1 the pressure scale is set by Equation 2.9 to

$$\mathcal{P} = \frac{\Delta p^*(L_x, 0, 0, 0)}{L_x} \quad (3.1)$$

where $\Delta p^*(L_x, 0, 0, 0)$ is the dimensional pressure drop over the streamwise length of the computational domain. The velocity scale is then $\mathcal{U} = (\mathcal{P}/\rho)^{1/2}$ and the length scale, \mathcal{L} , is a quarter of the

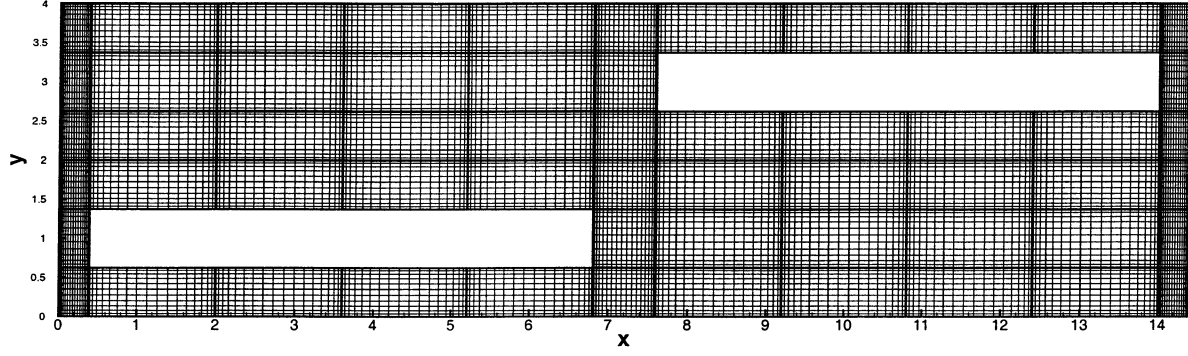


Figure 3.2: Staggered 1 Case Discretization

domain height. The Reynolds number, Re , in Equation 2.1 is therefore defined using these scales.

For the purposes of comparison to the results of Zhang an alternative Reynolds number, Re_{D_h} , may be defined based on the hydraulic diameter, D_h^* , and mean flow velocity at the minimum cross sectional area, \bar{U}_{min}^* . This Reynolds number is then defined as

$$Re_{D_h} = \frac{\bar{U}_{min}^* D_h^*}{\nu} \quad (3.2)$$

where the dimensional (as denoted by the superscript *) hydraulic diameter and mean velocity, are given by

$$D_h^* = \frac{4A_{min}^* L_x^*}{\Omega_f^*} \quad (3.3)$$

$$\bar{U}_{min}^* = \frac{\bar{Q}_x^*}{A_{min}^*} \quad (3.4)$$

In the above equations A_{min}^* is the effective minimum cross flow area defined as $A_{min}^* = (L_y^* - 2b^*)L_z^*$, Ω_f^* is the combined surface area of the bodies within the computational domain given by $\Omega_f^* = 4(h^* + b^*)L_z^*$, and \bar{Q}_x^* is the average volumetric flow rate in the x direction. In addition, we will also define the Darcy friction factor, f , and the Colburn j factor as

$$f = \frac{\Delta p^*}{\frac{1}{2}\rho \bar{U}_{min}^{*2}} \frac{D_h^*}{4L_x^*} = \frac{D_h}{2} \frac{1}{\bar{U}_{min}^2} \quad (3.5)$$

Re	Re_{D_h}	$Re_{D_h,Zhang}$	$\%Diff$	f	f_{Zhang}	$\%Diff$	j	j_{Zhang}	$\%Diff$
15	471	474	0.6	0.0645	0.0634	1.7	0.0335	0.0338	0.9
20	709	720	1.5	0.0506	0.0490	3.3	0.0253	0.0253	0.0
25	986	1018	3.1	0.0409	0.0383	6.8	0.0206	0.0191	7.9
30	1227	1246	1.5	0.0380	0.0368	3.3	0.0184	0.0188	2.1

Table 3.2: Comparison of Staggered 1 Flow Values

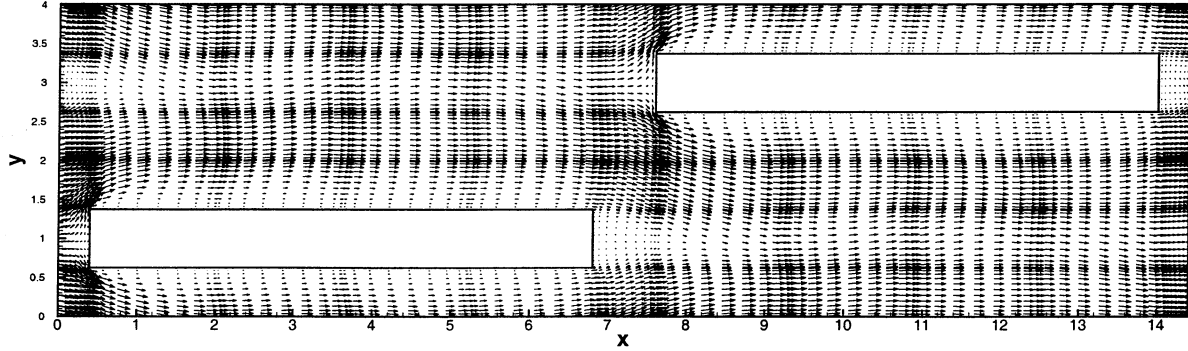


Figure 3.3: Instantaneous flow solution for Staggered 1 case at $Re = 20$

$$j = \frac{\langle \bar{Nu} \rangle}{RePr^{0.4}} \quad (3.6)$$

where $\langle \bar{Nu} \rangle$ is the global time averaged Nusselt number for a body, based on the hydraulic diameter as defined by Equation 3.3.

Comparisons of these quantities with the results of Zhang [60] have been made for flow solutions obtained at four different Reynolds numbers. The values and the relative differences are presented in Table 3.2. The results show a good agreement in all quantities for all of the Reynolds numbers considered. A vector plot of an instantaneous flow solution for Reynolds number, $Re = 20$, is shown in Figure 3.3. The expected flow features may be observed; developing boundary layers along the top and bottom surface of each body, a stagnation point on the front face, a low velocity recirculating wake region directly behind the body, and waviness in the downstream wake indicative of shed wake vortices. Figure 3.4 shows the contours of the temperature solution at the same instant for $Re = 20$. Thermal boundary layers are seen to develop along the surfaces of the bodies, with the waviness of the temperature contours in the wake also indicative of the presence of shed wake vortices. The effects of the periodic vortex shedding phenomena are also manifest in the signatures of the coefficients of lift and drag, given by equations 3.7 and 3.8, shown in Figure 3.5 for $Re = 20$.

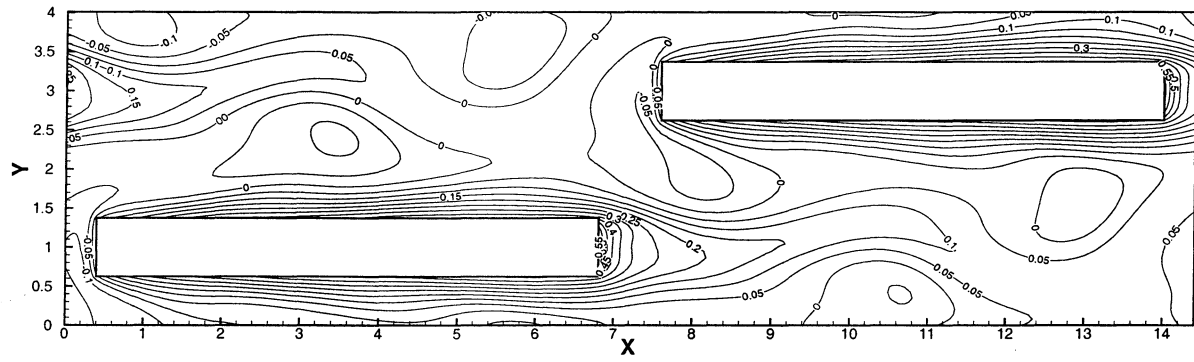


Figure 3.4: Instantaneous temperature solution for Staggered 1 case at $Re=20$

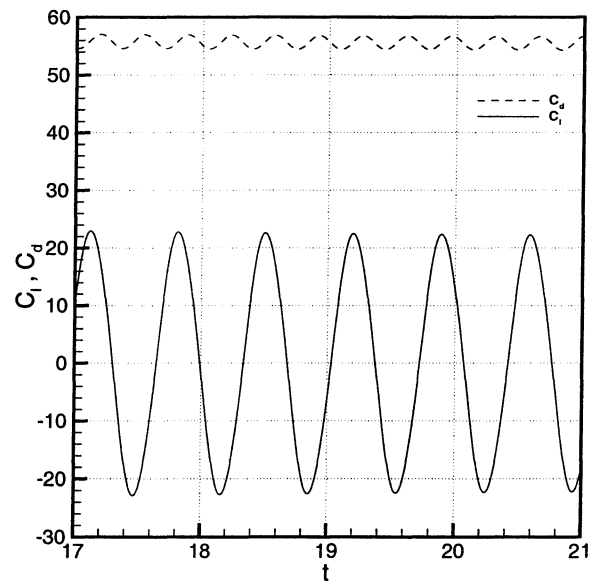


Figure 3.5: Lift and Drag Coefficients for the Staggered 1 case at $Re=20$

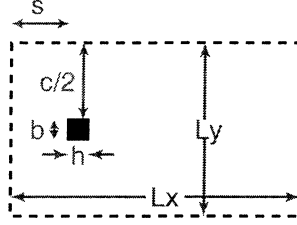


Figure 3.6: XY Non-Periodic Geometric Parameters

b	1.0
h	1.0
s	5.0
c	17.0
Lx	23.0
Ly	18.0
X Bnd.	In/Out
Y Bnd.	In/In
M	62
Nx	16
Ny	16
β_x	0.0
β_y	0.0

Table 3.3: Square XY Non-Periodic Parameter Values

3.3 Square Cylinder

This section presents a comparison of results with those of Robichaux [42] for two dimensional uniform flow over a square cylinder. The basic geometry of this flow case is depicted in Figure 3.6. This case is later referred to as the Square XY Non-periodic case. Table 3.3 lists the values of the parameters used and the discretization is shown in Figure 3.7, which employs 62 subdomains with 16 grid points in the x and y directions in each domain. An inflow boundary condition is utilized at the left boundary with a uniform streamwise flow specified. The velocity along the upper and lower boundaries is fixed and set the same as the velocity on the inflow boundary. The right boundary is specified as an outflow boundary condition of the type described in Section 2.2.3. No streamwise pressure gradient is imposed for this flow thus the values of β_x and β_y are set to zero. The velocity scale chosen was the velocity of the oncoming flow, U_∞^* , and the length scale set to the object height, b^* . The Reynolds number is therefore defined as $Re = U_\infty^* b^* / \nu$

The flow quantities compared to those obtained by Robichaux are the coefficients of lift and

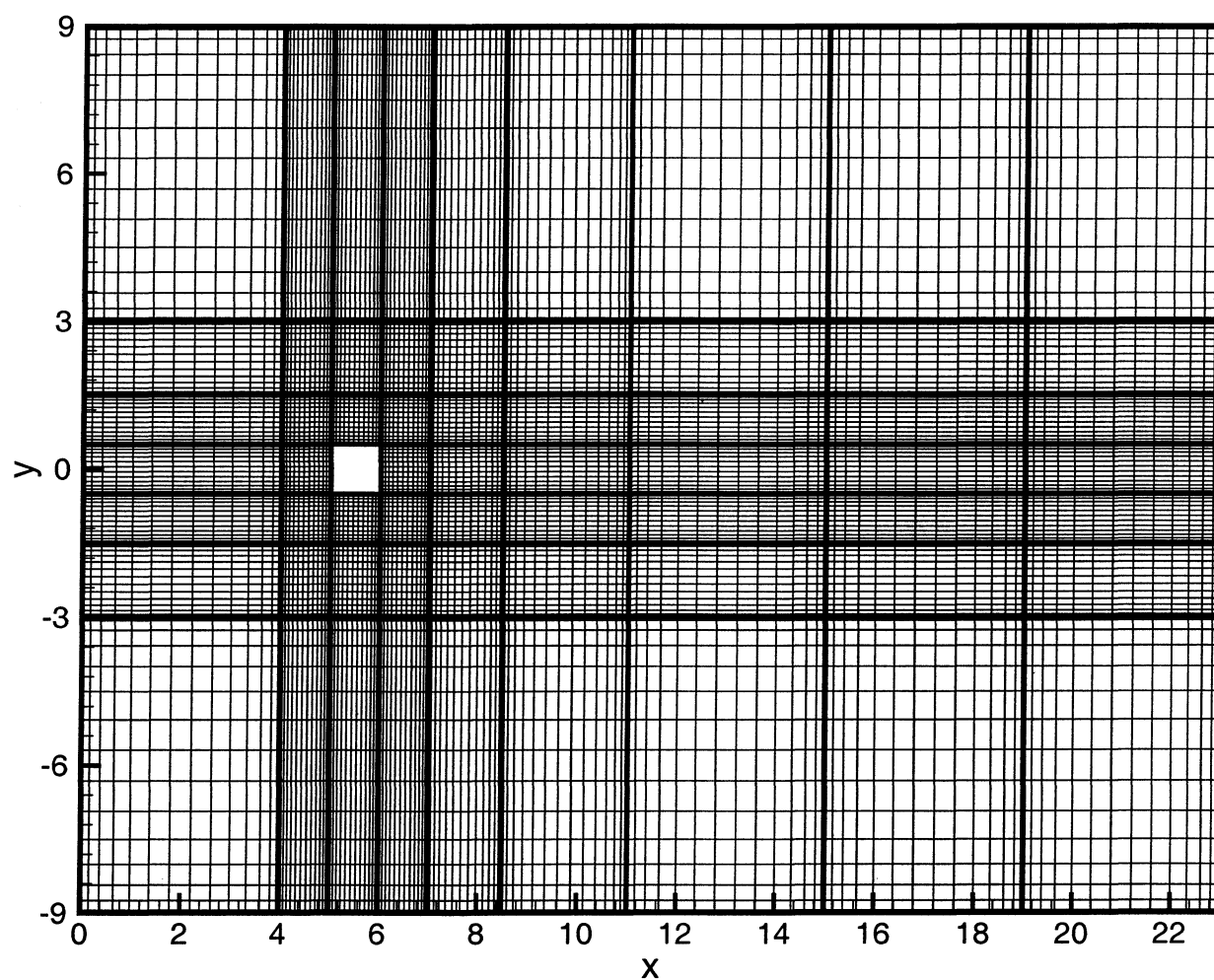


Figure 3.7: Square XY Non-Periodic Discretization

Re	\bar{C}_d	$\bar{C}_{d,R}$	$\%Diff$	C'_d	$C'_{d,R}$	$\%Diff$	C'_l	$C'_{l,R}$	$\%Diff$	St	St_R	$\%Err$
100	1.56	1.53	1.9	0.007	0.007	0.0	0.27	0.23	17.4	0.152	0.154	1.3
150	1.54	1.57	1.9	0.029	0.024	20.0	0.42	0.38	10.5	0.164	0.166	1.2

Table 3.4: Comparison of Square XY Non-Periodic Flow Values

drag, along with the Strouhal number. These quantities are defined as follows

$$C_d = \frac{F_x}{\frac{1}{2}U_\infty^2 b L_z} \quad (3.7)$$

$$C_l = \frac{F_y}{\frac{1}{2}U_\infty^2 b L_z} \quad (3.8)$$

$$St = \frac{f_s b}{U_\infty} \quad (3.9)$$

where F_x and F_y are the net force on the body in the corresponding directions and f_s is the primary frequency of the lift oscillation. The values of these quantities have been determined at two Reynolds numbers where the flow is unsteady and are compared with the values reported by Robichaux [42] in Table 3.4. The value \bar{C}_d is the mean value of the drag fluctuation and C'_d and C'_l are the amplitude of the drag and lift fluctuations. Generally good agreement may be seen between the two sets of results, with the largest differences occurring in the values of the oscillation amplitudes.

A vector plot of the instantaneous flow solution for $Re = 150$ is shown in Figure 3.8. The flow is seen to be relatively undisturbed upstream of the body and away from the body in the transverse direction. A wake region is observed, with recirculating flow directly behind the body and downstream waviness indicative of shed vortices. The vortices may be visualized through calculation of the swirling strength at each point in the flow field. The swirl, as described by Zhou [61] is plotted in Figure 3.9 for the same instantaneous solution. Distinct regions of concentrically increasing swirling strength are observed and represent individually shed vortices. In this plot the presence of the well known Karman Vortex street may be readily observed, with vortices periodically shed from alternating surfaces of the body and convecting directly downstream. Smooth convection of the

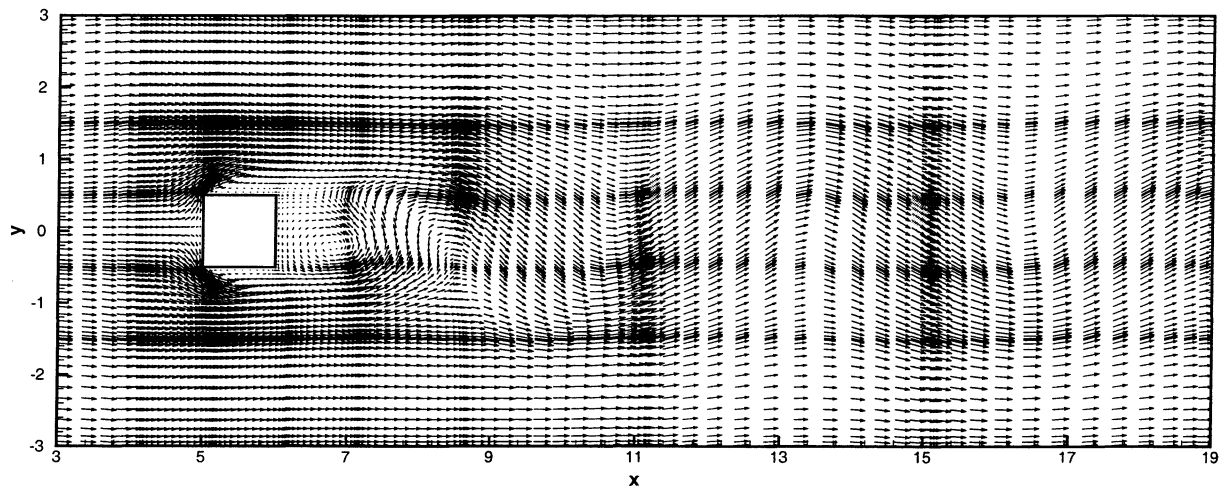


Figure 3.8: Instantaneous Flow Solutions for Square XY Non-Periodic at $Re= 150$

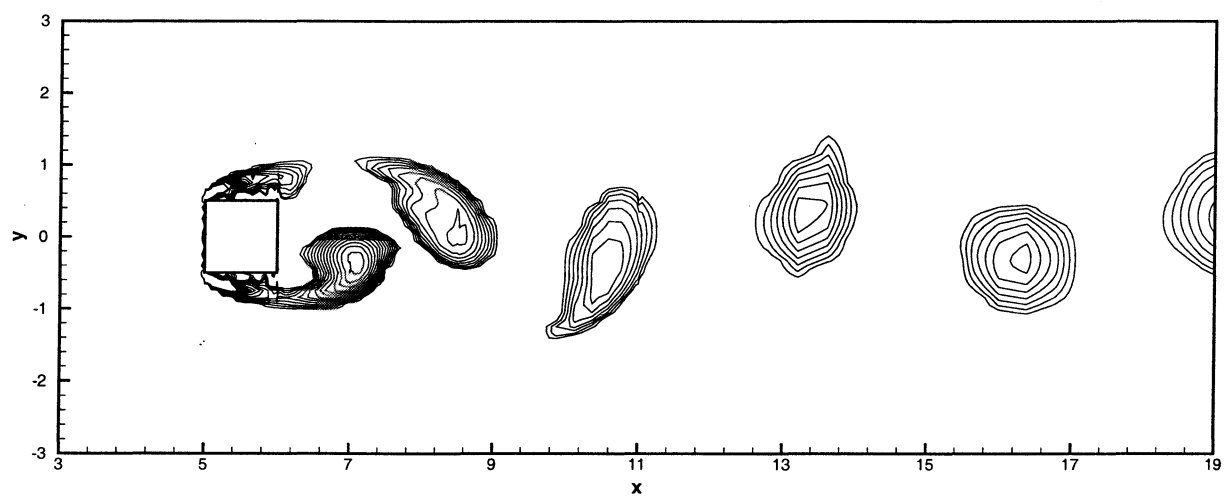


Figure 3.9: Instantaneous Swirl for Square XY Non-Periodic at $Re= 150$

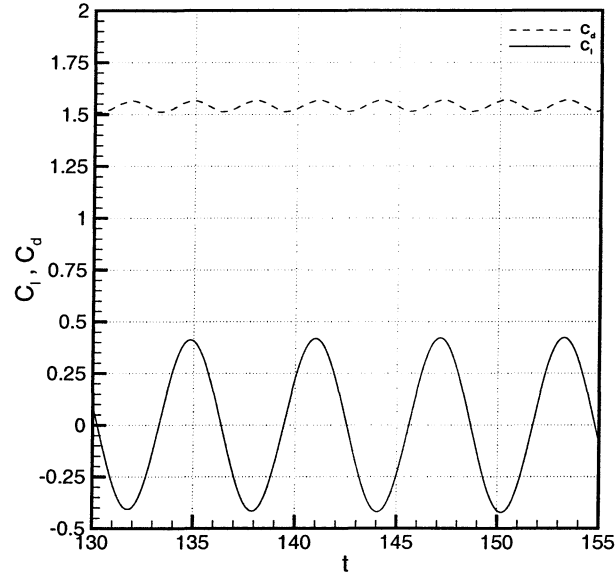


Figure 3.10: Lift and Drag Coefficients for Square XY Non-Periodic at $Re=150$

vortices from the computational domain is observed with the implemented buffer domain outflow boundary condition. The effect of the vortex shedding on the lift and drag experienced by the object are shown in Figure 3.10.

Chapter 4

Stability of Bluff Body Arrays

4.1 Introduction

This section discusses the numerical and analytic stability results obtained for flow over several different arrangements of rectangular cylinders. Presented are the numeric laminar base flows, instability growth rates, critical Reynolds Numbers, and eigenfunctions for the various cases considered. A simplified one-dimensional stability analysis for Inline arrays is also presented. Based on the two-dimensional numeric and one-dimensional analytic results the effect of the various geometric parameters on the flow stability is discussed.

The solution cases considered are listed and described in Table 4.1 and Figure 4.1. The cases fall into three general classes, as indicated in Figure 4.1. The extent of the computational domain for all three cases is denoted by the dashed lines and the parameters L_x and L_y . The Inline and Staggered cases implement periodic boundary conditions in the x and y directions, making the computational domain a single cell in an infinite array. The Non-periodic cases have an Inflow condition at the left x boundary and an Outflow condition at the right x boundary. Both X Non-periodic cases use a periodic condition at the y boundaries to produce a vertical column of bodies. The Rectangular XY Non-periodic case used a far - field condition in the y direction for simulation of flow around an isolated body. The Square XY Non-periodic case, however, used an Inflow condition to apply a fixed velocity equal to the inlet free stream velocity along the y boundaries. For both of the XY Non-periodic cases, the y extent of the computational domain was enlarged to reduce the influence of the y boundary conditions on the solution. The object frontal height, and streamwise length, are given by the parameters b and h , respectively. While the streamwise and transverse spacing

Case	b	h	s	c	Lx	Ly	X Bnd.	Y Bnd.
Inline 1	0.90	10.00	10.00	1.10	20.0	2.0	Per.	Per.
Inline 2	0.90	10.00	10.00	3.10	20.0	4.0	Per.	Per.
Inline 3	0.90	10.00	20.00	1.10	30.0	2.0	Per.	Per.
Inline 4	0.90	10.00	20.00	3.10	30.0	4.0	Per.	Per.
Staggered 1	0.75	6.41	0.79	3.25	14.4	4.0	Per.	Per.
Staggered 2	0.90	10.00	0.00	3.10	20.0	4.0	Per.	Per.
Staggered 3	0.90	10.00	0.00	9.10	20.0	10.0	Per.	Per.
Rect. XY Non-periodic	0.90	10.00	5.00	19.10	30.0	20.0	In/Out	Far
Rect. X Non-periodic	0.90	10.00	5.00	1.10	60.0	2.0	In/Out	Per.
Square XY Non-periodic	1.00	1.00	5.00	17.0	23.0	18.0	In/Out	In
Square X Non-periodic	1.00	1.00	5.00	1.00	23.0	2.0	In/Out	Per.

Table 4.1: Numerical Solution Cases

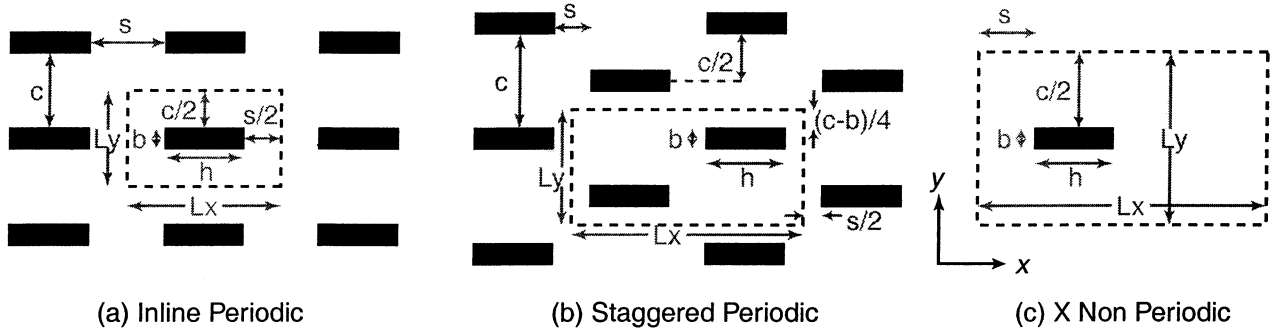


Figure 4.1: Inline, Staggered, and Non-periodic Geometries

between objects is given by s and c .

Two basic arrangements of rectangular bodies in an array have been studied: the Inline array, and the Staggered array. For these two basic cases, variation of the parameters governing the array geometry allows an assessment of the impact of the array geometry on the onset of unsteadiness and the resulting Karman vortex shedding process. Most of the existing literature, and correspondingly our understanding, has been limited to the case of instability of the flow over an isolated cylinder. In order to place the present results for the inline and staggered arrays in proper context, the case of an isolated rectangular cylinder has also been considered and is presented as the Rectangular XY Non-periodic case. The Rectangular XY Non-periodic case may be viewed as the limiting case of a periodic array with a very large domain of periodicity along x and y , thus permitting homogenization of the flow from one cylinder to the next. With the flow approaching each element, therefore, considered to be nearly uniform.

The inline and staggered cases model an array of infinite extent by assuming flow periodicity along the streamwise and transverse directions. A consequence of this assumption is that the disturbance exiting the computational domain is fed back into the domain at the inlet. To discern what, if any, impact this feedback may have upon the stability results the Rectangular X Non-periodic case has been considered. This non-periodic case avoids the application of a periodic boundary condition in the streamwise direction and utilizes an outflow condition at the downstream boundary along with a uniform inflow condition at the upstream boundary. A comparison of these results to the inline and staggered array results allows an evaluation of the feedback effect, and also yields information on the stability of the developing flow in the entry region of a finite array. Finally two cases employing objects with a square cross-section were examined, Square X Non-periodic and Square XY Non-periodic, in order to assess the impact of the bodies aspect ratio, h/b , on flow stability.

4.2 Numerical Two-Dimensional Stability Analysis

The DNS code described in Chapter 2 was utilized to study the stability of the laminar flow solutions when subjected to a generalized disturbance. The first step in the stability analysis was the generation of a steady laminar flow solution, \vec{U} , at a given Reynolds number, herein referred to as the laminar base flow. A valid laminar flow solution may be found at any Reynolds number through direct solution of the Navier - Stokes equations, provided no disturbance is introduced to destabilize the flow. The numerical accuracy of the solution methodology was generally sufficient to allow the direct calculation of laminar flow solutions at super critical Reynolds numbers. However, the generation of a laminar solution at these Reynolds numbers was further assured by the application of a symmetry condition to the flow about each body. The relevant instability is of a form possessing anti-symmetry about a line, parallel to the streamwise direction, passing through the center of each body. The application of a symmetry condition about each body, having the form

$$\begin{aligned} u(x, y_c + y', z, t) &= u(x, y_c - y', z, t) \\ v(x, y_c + y', z, t) &= -v(x, y_c - y', z, t) \\ p(x, y_c + y', z, t) &= p(x, y_c - y', z, t) \end{aligned} \tag{4.1}$$

where y_c is the coordinate of the body centerline and y' is the distance from the center line, prevents the existence of any anti-symmetric disturbance and thus insures a steady laminar flow. A streamline plot of the laminar flow solution for each of the general solution cases is show in Section 4.3.

After a laminar flow solution is obtained, the symmetry condition is removed and a small anti-symmetric disturbance is added. The added disturbance consists of a small streamwise pressure gradient, which varies in the y direction from positive to negative. The disturbance is applied over a fraction of a non-dimensional time unit and its magnitude and sign is varied smoothly over time so that at the final instant of its application it has the opposite sign of its initial application. Following the introduction of the disturbance the flow is allowed to evolve in time, with the disturbance growing in unstable flows and decaying for stable flows. To insure that the base flow remains constant as the disturbance evolves the flow solution is split at each time step into symmetric and anti-symmetric components. The symmetric base component is held constant over time by fixing it to the initial laminar base flow solution, thus allowing only the anti-symmetric component to evolve in time. This procedure allows for more efficient extraction of the linear instability growth rate, and as a secondary effect prevents non-linear saturation of the disturbance. The growth of the disturbance is measured by calculating the Frobenius norm of the difference between the disturbed, \vec{u} , and base, \vec{U} , velocity fields,

$$\|\vec{u}'\| = \|\vec{u} - \vec{U}\| = \left\{ \sum_{i=1}^{N_x} \sum_{j=1}^{N_y} \left[(u_{i,j} - U_{i,j})^2 + (v_{i,j} - V_{i,j})^2 \right] \right\}^{1/2} \quad (4.2)$$

Figure 4.2 shows the disturbance growth as measured by Equation 4.2 for the Inline 2 case. All of the other infinite arrays exhibit similar behavior. Below the critical Reynolds number the perturbation can be seen to decay exponentially. Similarly, above the critical Reynolds number, the perturbation experiences exponential growth at a constant rate for a given Reynolds number. The exponential growth constant, or growth rate, can be extracted from these simulations as the value of the slope of the linear perturbation energy curve on a log linear plot. Under normal circumstances the perturbation growth would saturate, ceasing to be exponential, once the perturbation had grown to sufficient size to interact with the base flow in a non-linear fashion. In this analysis,

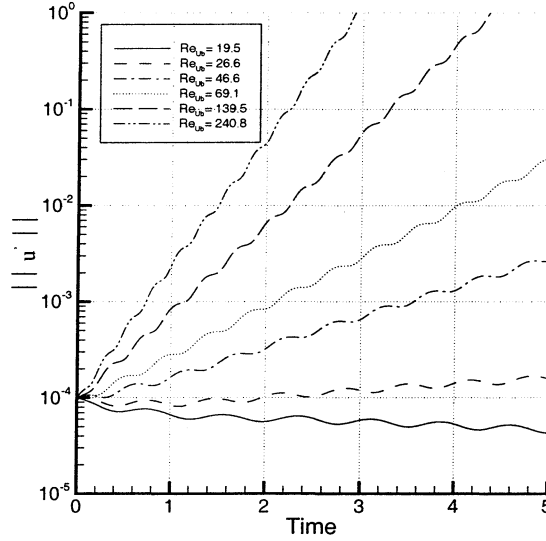


Figure 4.2: Growth of Perturbation for Inline 2 Case

however, the base flow is held fixed preventing non-linear interaction and thus saturation.

The results shown in Figure 4.2 provide a global measure of the perturbation growth. An alternative is to measure the perturbation growth locally at a single point. Figure 4.3 plots on a log-linear scale the absolute value of the streamwise perturbation velocity at a point near the upper surface of a body, just beyond the trailing edge, for the Inline 2 case with $Re_{\bar{U}_b} = 69.1$. The perturbation velocity has an initial value of zero and oscillates sinusoidally in time with an exponentially growing amplitude. Measuring the growth of the oscillation amplitude, which is shown as a straight line in Figure 4.3, yields a growth rate value that agrees to within one percent with the value obtained through the global measure. Similarly, growth rates calculated at other points in the flow have the same value, confirming the global nature of the instability and the uniform growth of the disturbance over the entire domain. The oscillatory behavior seen in Figures 4.2 and 4.3 is a consequence of the unsteady nature of the disturbance, with the steady base flow being unstable to a periodic state through a Hopf bifurcation.

With the perturbation growth rate, ω_i , determined at several different Reynolds numbers the critical value of the Reynolds number, at which the perturbation neither grows nor decays, may be determined for the solution case. Figure 4.4 shows the extracted growth rates from Figure 4.2

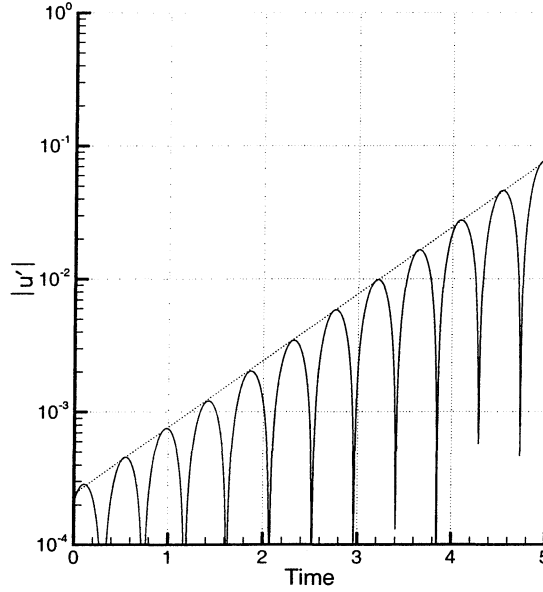


Figure 4.3: Growth of Perturbation for Inline 2 Case with $Re_{\bar{U}b} = 69.1$

plotted against the Reynolds number for the Inline 2 case. The value of the the Reynolds number at which the growth rate becomes zero is the critical value, for this case the value is $Re_{\bar{U}b} = 22.6$.

In addition to calculating the linear growth rate of the disturbance, the disturbance velocity field can be determined by subtracting the laminar base flow solution from the disturbed flow solution. These results are shown for the Inline 2 case in Figure 4.7. The form of the disturbance was calculated by subtracting the base flow solution, \vec{U} , from the disturbed velocity field, \vec{u} , after the disturbance was given sufficient time to grow in amplitude. This procedure yields the perturbations velocity fields, $\vec{u}' = \vec{U} - \vec{u}$ which is plotted in this figure. The perturbation velocity field calculated in this manner is analogous to the eigenfunction determined through normal mode analysis. Plotted in part (c) of the figure is the swirling strength of the perturbation field. Swirl is the magnitude of the imaginary part of the eigenvalue of the local velocity gradient tensor. This method is a frame invariant technique of identifying vortices, where high values of swirl occur in regions of strong rotary motion. As such, swirling strength is an effective tool for the visualization of vortices (Zhou [61]) with an isolated region of concentrated swirl generally indicative of the presence of a vortex in that area.

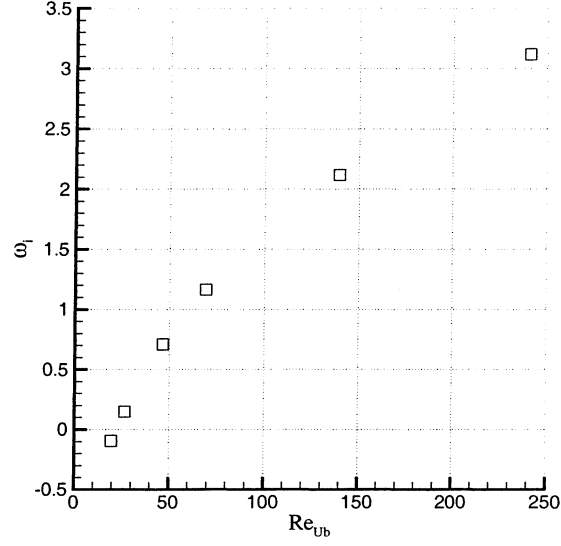


Figure 4.4: Growth Rate Values for Inline 2 Case

4.3 Two Dimensional Stability Results

This section presents the results of the two dimensional stability analysis for each of the solution cases described in Figure 4.1 and Table 4.1. For each of the general solution classes: Inline Arrays, Staggered Arrays, and Non-Periodic, examples of the laminar base flow solution are shown, along with profiles of the U velocity and examples of the eigenfunction. For each solution case, the critical Reynolds number has been determined and is presented in Table 4.2. This table shows the critical value of $Re_{\bar{U}b}$, which is the critical Reynolds number based on an average flow velocity defined as

$$\bar{U} = \frac{\bar{Q}_x}{L_y} \quad (4.3)$$

where \bar{Q}_x is the net volumetric flow rate through the computational domain in the x direction and b is the frontal height of the object. This Reynolds number, defined by the choice of velocity and length scales, is neither the only one possible or even the most natural for a given solution case. However, it is useful for comparing stability results among the different solution cases and for that purpose is used in this section. Later, in Sections 4.4 and 4.5 an alternative form of the Reynolds number is defined which better characterizes the flow in Inline and Staggered arrays. Also shown

Case	$Re_{\bar{U}b,crit}$	λ_x
Inline 1	31.4	3.3
Inline 2	22.6	6.0
Inline 3	33.8	3.3
Inline 4	21.8	6.9
Staggered 1	48.6	4.3
Staggered 2	60.9	3.7
Staggered 3	25.8	7.2
Rect. X Non-periodic	31.5	3.4
Rect. XY Non-periodic	111.6	6.5
Square X Non-periodic	28.0	3.3
Square XY Non-periodic	43.5	6.0

Table 4.2: Critical Reynolds Number for Numerical Solution Cases

in Table 4.2 is the approximate streamwise wavelength, λ_x , of the disturbance, which has been obtained from the disturbance eigenfunctions. Table 4.3 presents a detailed listing of the growth rate, ω_i , and frequency, ω_r , of the disturbance at each Reynolds number, for each of the cases considered.

4.3.1 Inline Array Results

Numerical stability results have been obtained for each of the four Inline array cases listed in Table 4.1. In each case, a computational domain with periodic boundary conditions containing a single rectangular body has been utilized to model an inline array of infinite extent. Each solution case employs a body of the same dimensions. Two different horizontal, s , and vertical, c , spacings have been used to construct the four cases and evaluate the effects of these parameters on the flow stability.

The laminar base flow solution is qualitatively similar for all of the Inline solution cases. Figure 4.5 shows the flow solution for the Inline 2 case at a $Re_{\bar{U}b}$ number of 26.6, which is close to and slightly above the critical value. In this figure the laminar flow streamlines around four elements of an infinite array are shown for clarity of visualization, with the actual flow solution obtained for only one element. The flow about each body is identical and symmetrical, with a stagnation point on the front face of the body, and a steady recirculation region behind the trailing edge.

Of particular interest is the flow in the wake region behind the trailing edge of each body. It will later be shown that the primary instability is a wake instability, and thus strongly influenced by

Case	Re	ω_i	ω_r
Inline 1			
	20.0	4.94×10^{-3}	0.976
	25.0	3.28×10^{-1}	0.811
	30.0	5.91×10^{-1}	0.689
	35.0	9.06×10^{-1}	0.625
Inline 2			
	5.0	-9.45×10^{-2}	0.754
	6.0	1.49×10^{-1}	0.668
	8.0	7.10×10^{-1}	0.519
	10.0	1.16×10^0	0.444
	15.0	2.11×10^0	0.336
	20.0	3.11×10^0	0.266
Inline 3			
	15.0	-3.23×10^{-1}	0.805
	16.5	-7.90×10^{-2}	0.840
	17.5	1.18×10^{-1}	0.758
	20.0	3.49×10^{-1}	0.694
	25.0	7.40×10^{-1}	0.584
	30.0	1.14×10^0	0.508
Inline 4			
	5.0	1.47×10^{-1}	0.591
	5.5	2.64×10^{-1}	0.576
	6.0	4.17×10^{-1}	0.534
	8.0	1.59×10^0	0.371
Staggered 1			
	15.0	-1.00×10^{-1}	0.394
	17.0	8.57×10^{-2}	0.365
	18.0	1.95×10^{-1}	0.348
	20.0	3.43×10^{-1}	0.334
	25.0	6.82×10^{-1}	0.289
	30.0	1.12×10^0	0.253
Staggered 2			
	10.0	-3.13×10^{-1}	0.0
	20.0	-3.14×10^{-2}	0.346
	21.0	8.01×10^{-2}	0.327
	23.0	2.56×10^{-1}	0.300
	30.0	9.43×10^{-1}	0.249
Staggered 3			
	4.0	3.25×10^{-3}	0.761
	5.0	3.24×10^{-1}	0.585
	6.0	5.39×10^{-1}	0.501

Table 4.3: Perturbation Growth Rates and Frequencies

Case	Re	ω_i	ω_r
Rect. X Non Per.			
	30.0	-5.01×10^{-2}	1.739
	35.0	-4.83×10^{-4}	1.724
	38.0	4.33×10^{-2}	1.707
	40.0	6.56×10^{-2}	1.700
Rect. XY Non Per.			
	80.0	-6.11×10^{-5}	9.066
	100.0	7.30×10^{-6}	8.545
	125.0	1.11×10^{-3}	8.269
	150.0	1.61×10^{-2}	7.997
	175.0	3.98×10^{-2}	7.668
	200.0	5.39×10^{-2}	7.563
Square X Non Per			
	25.0	-6.77×10^{-2}	1.772
	28.0	1.43×10^{-3}	1.746
	30.0	3.75×10^{-2}	1.729
	45.0	2.22×10^{-1}	1.685
	55.0	3.07×10^{-1}	1.626
Square XY Non Per			
	35.0	-3.36×10^{-2}	4.479
	41.0	-8.28×10^{-3}	4.404
	45.0	7.72×10^{-3}	4.337
	55.0	4.21×10^{-2}	4.309

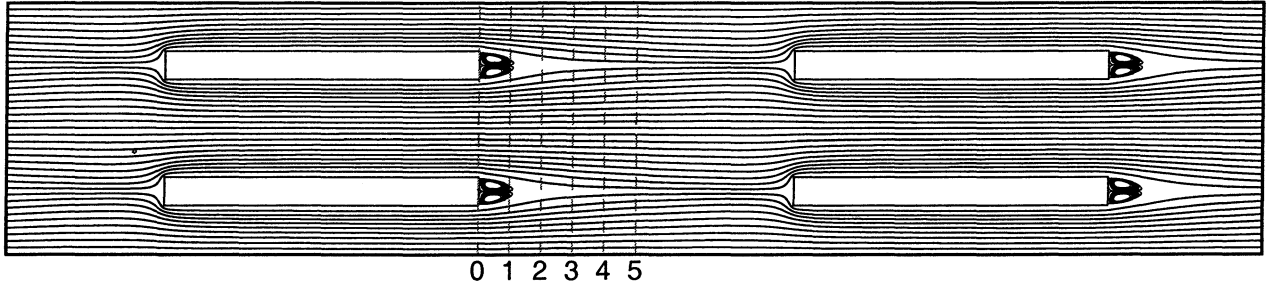


Figure 4.5: Streamlines for Case Inline 2 at $Re_{\bar{U}_b} = 26.6$

Coefficient	Profile 0	Profile 1	Profile 2	Profile 3	Profile 4	Profile 5
0	4.933	4.934	4.934	4.934	4.934	4.934
1	4.979	4.591	4.090	3.702	3.322	3.037
2	-0.589	-0.500	-0.353	-0.260	-0.184	-0.136
3	-0.178	-0.016	-0.006	-0.006	-0.005	-0.005
4	0.278	0.028	0.006	0.002	0.001	0.001

Table 4.4: Expansion Coefficients for Case Inline 2 u Velocity Profiles

the nature of the flow in this region. Profiles of the u velocity in this region are shown for the four solution cases in Figure 4.6. The profiles are located along the dashed lines shown in Figure 4.5 and spaced approximately one non dimensional unit apart in the x direction, with the first at the trailing edge of the body. The profile is centered along the body centerline and extends over a single computational domain. From Figure 4.6, the profiles in all four cases may be seen to be similar. For each case, the profiles are symmetric and with the exception of the profile at the trailing edge, nearly sinusoidal with amplitude decaying in the x direction.

To quantify the sinusoidal nature of the profiles a Fourier analysis was performed. This analysis showed that, due to the symmetry of the flow, the profiles may be represented as a cosine series expansion of the form

$$u(y) = c_0 + \sum_{k=1}^{\infty} c_k \cos\left(\frac{k2\pi y}{L_y}\right) \quad (4.4)$$

with the coefficients, c_k , given in Table 4.4. It can be seen that the first coefficient c_0 , which is the mean flow rate, remains the same for each of the profiles. The second coefficient, which produces the sinusoidal shape of the profiles, decays as the profiles move downstream. For all profiles, except the first, the higher coefficients of the expansion decay, rapidly with increasing k , with the third coefficient generally an order of magnitude smaller than the second. Given this rapid decay the profiles could be well represented by an expansion consisting of just the first two coefficients, and therefore as a simple sinusoid without higher harmonics.

The sinusoidal profile is a result of the channel region existing between each set of paired bodies. As the oncoming flow enters the region between the two bodies it develops into the parabolic profile found in Poiseuille flow. If the length of the channel region is sufficient the exiting profile becomes precisely parabolic, as is shown by the four 0 Profiles in Figure 4.6. At the trailing edge of a column

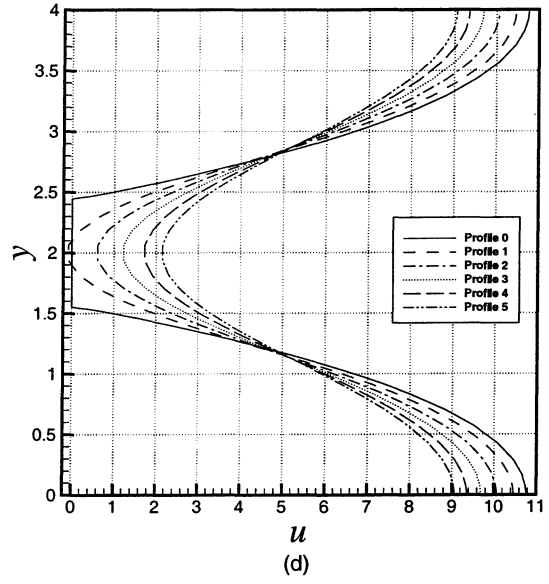
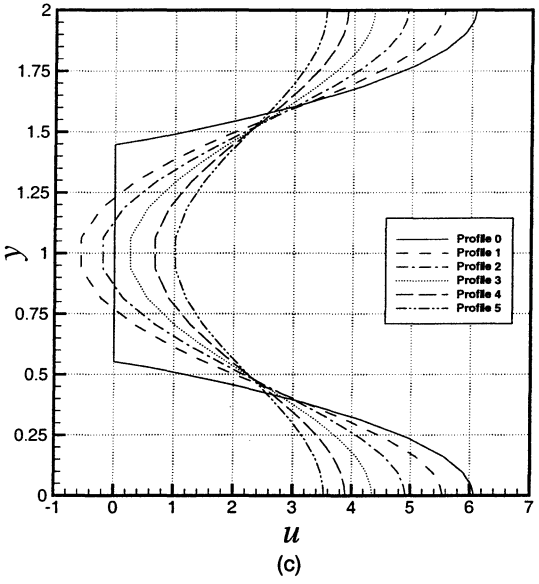
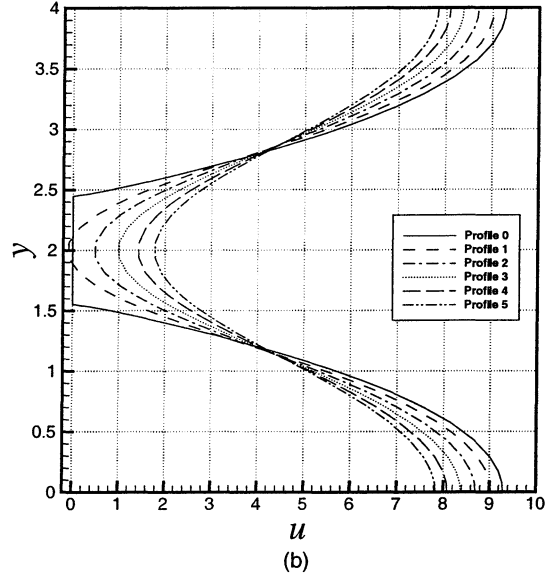
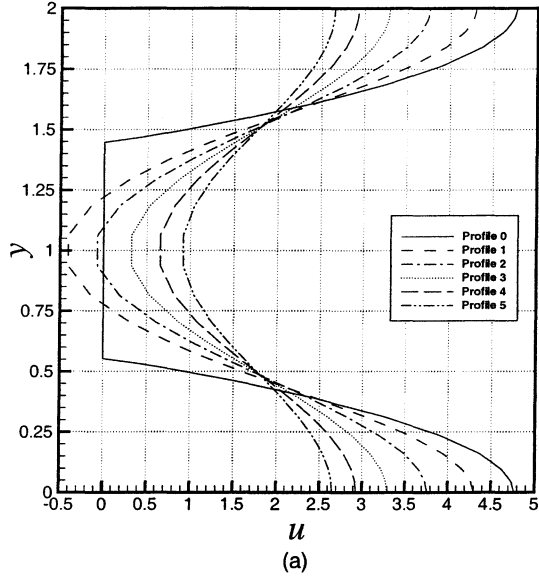


Figure 4.6: Profiles of u velocity for Cases (a) Inline 1 at $Re_{\bar{U}_b} = 31.9$, (b) Inline 2 at $Re_{\bar{U}_b} = 26.6$, (c) Inline 3 at $Re_{\bar{U}_b} = 35.5$, and (d) Inline 4 at $Re_{\bar{U}_b} = 25.9$

of bodies the set of parabolic profiles rapidly join together in the downstream direction to produce the sinusoidal profile. In cases where the length of the channel region, which is the length of the fin, is not of sufficient for the parabolic profile to develop the simple sinusoidal profile will not exist. However, the parabolic profile need not be fully developed in the classical sense, with a reasonable approximation to the parabolic shape sufficient to produce an essentially sinusoidal profile in the wake region. Furthermore, in an inline array the oncoming flow entering a channel region will retain an imprint of the parabolic profile produced by the upstream bodies, which greatly reduces the length of the channel region needed to produce a sufficiently parabolic profile. Thus, in general, a large vertical spacing to channel length ratio is needed to generate non sinusoidal profiles. The cases considered here had an inter-fin channel height to body height, ratio, c/b , range of 1.2 - 3.4. Within this range all of the solution cases considered produced similar sinusoidal profiles. Beyond this range, flows will still have velocity profiles of the form given in Equation 4.4, however the decay of the higher coefficient may be delayed.

Overall the velocity field in the wake regions of an Inline array has a simple description. The u velocity profiles are of a simple sinusoidal nature. The v velocity profiles are similarly sinusoidal, with a magnitude which is small in comparison to that of the u velocity. Such velocity fields have been the subject of one-dimensional stability analysis with useful results and Section 4.4 presents the results of this type of analysis for the Inline flow cases.

The numerical two-dimensional stability analysis described in section 4.2 was applied to the laminar flow solutions obtained for the Inline array cases. The resulting critical values of the Reynolds number are shown in Table 4.2. The critical value of the Reynolds number for arrays Inline 1 and Inline 3 can be seen to be approximately 32, while the critical value for arrays Inline 2 and 4 is approximately 22. It is therefore clear that the value of the Reynolds number, when defined using average flow velocity \bar{U} and body thickness b , is not the sole parameter determining the stability of the flow. Other parameters that may play a role are the aspect ratio of the body, h/b , the streamwise spacing, s , and the transverse spacing, c .

The critical Reynolds number data in Table 4.2 show that the streamwise spacing does not effect the value of the critical Reynolds number at which the onset of instability occurs for these cases. This is demonstrated by the fact that solution cases Inline 1 and Inline 3, which are identical

except for differing values of the streamwise spacing, have nearly the same value of the critical Reynolds number. The same observation can be made from the results for the Inline 2 and Inline 4 cases. Therefore, in general, the streamwise spacing, s , would appear to play little role in the stability of inline arrays. The instability possesses a wave like nature in the streamwise direction with wavelengths λ_x , which are given in Table 4.2 for the Inline cases. This suggests a condition under which the streamwise spacing could effect the critical Reynolds number. Small enough values of the streamwise spacing would prevent the instability from existing at the least stable wavelength, λ_x , and would likely shift the instability to a smaller, more stable wavelength, thus increasing the critical Reynolds number.

The data of Table 4.2 show that the transverse spacing, unlike the streamwise spacing does have a significant impact on the value of the critical Reynolds number. The Inline 1 and Inline 3 cases, which have the same transverse spacing are seen to have nearly the same critical Reynolds number, $Re_{\bar{U}b}$, of approximately 32. When the value of the transverse spacing is increased to produce the cases Inline 2 and Inline 4, the value of the critical Reynolds number falls to approximately 22. This shows a strong dependence of the critical Reynolds number for an Inline array on the value of the transverse spacing. In addition, the streamwise wavelength of the disturbance can also be seen to be effected, with the value of λ_x increasing from 3.3 to over 6 with the increase in transverse spacing.

Along with the value of the critical Reynolds number the form, or eigenfunction, of the instability has been determined for each of the Inline solution cases. The form of the disturbance yields further information about its nature. The eigenfunction for the Inline 2 case at $Re_{\bar{U}b} = 64.6$ is shown in Figure 4.7, with all of the inline array disturbances possessing a qualitatively similar form. The form of the instability consists primarily of a line of vortices formed behind the trailing edge of each body, which grow in strength in the downstream direction until the next set of bodies is encountered. This is seen most clearly in the swirl visualization, part (c) of Figure 4.7, where the regions of concentrated swirl contours represent individual vortices. A second weaker set of vortices can be seen to form between the primary vortices behind each body. The secondary vortices persist downstream into the channel regions formed by the trailing set bodies, where they appear to be damped out. The disturbance form is wave like in nature in the streamwise direction with

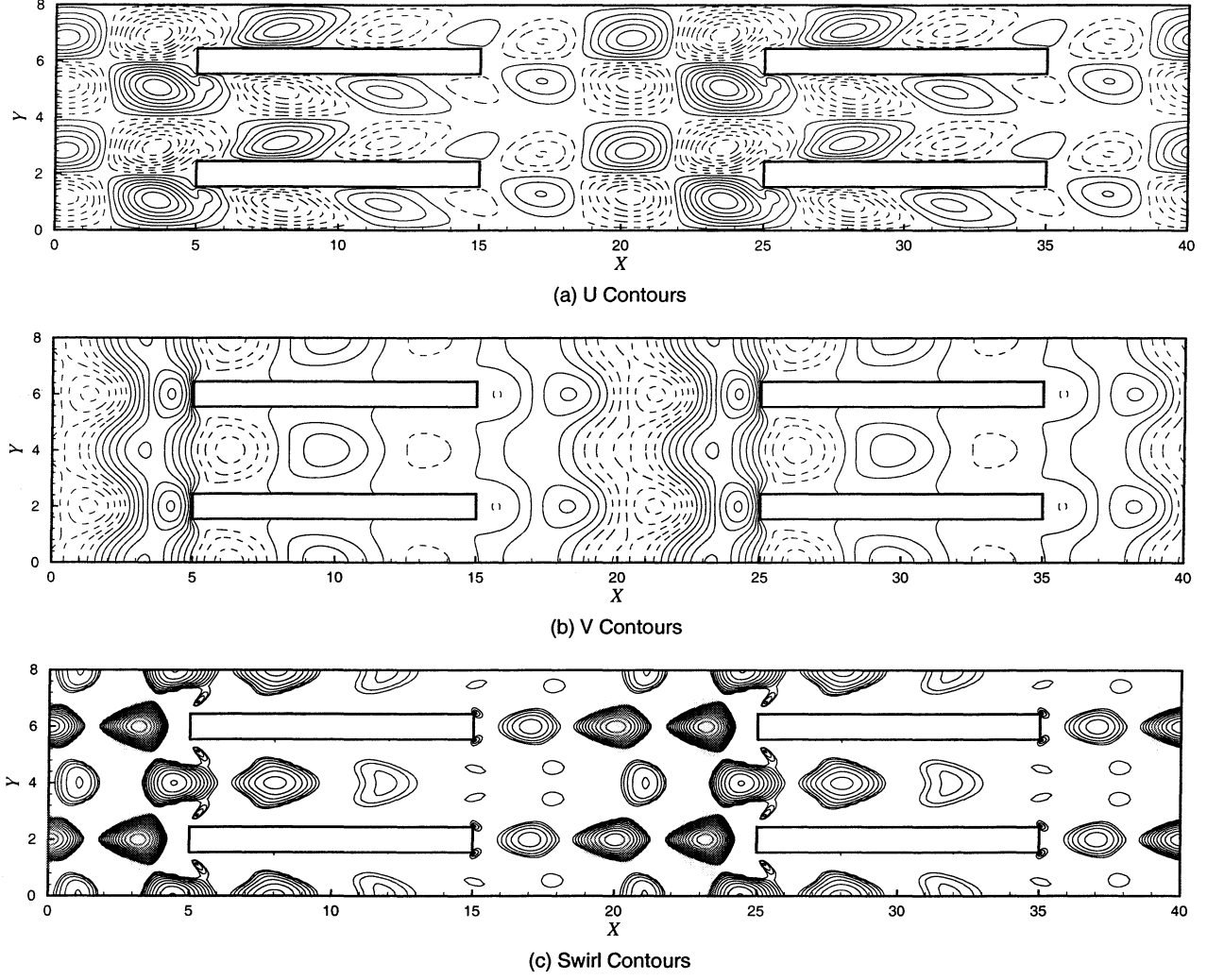


Figure 4.7: Perturbation for Inline 2 Case at $Re_{\bar{U}_b} = 26.6$

a wavelength set to integer divisions of the streamwise distance between bodies. This form of the eigenfunction is characteristic of those seen in wake instabilities and may be compared with the eigenfunctions for isolated bodies with a uniform oncoming stream shown later in Figures 4.15 and 4.16 which show a similar pattern of vortices. Note that what is shown is the form of the disturbance while still small in amplitude and before the effects of non linear saturation. After saturation the disturbance assumes a form similar to the well known Karman vortex street, with vortices shed from alternating sides of the objects trailing edge.

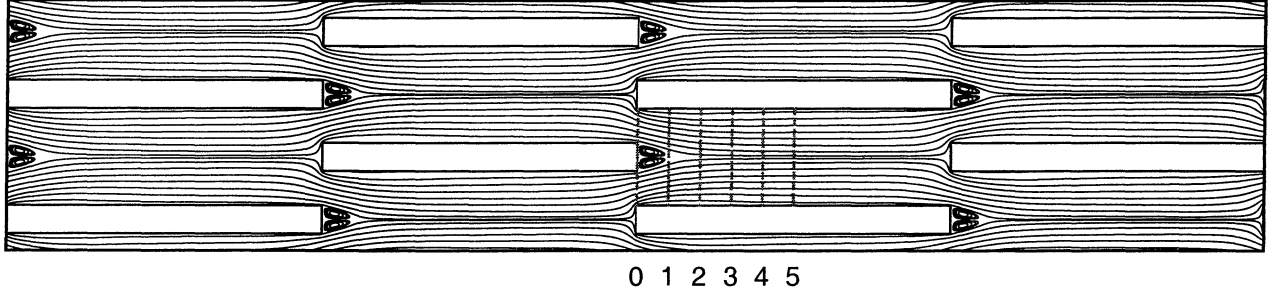


Figure 4.8: Streamlines for Case Staggered 2 at $Re_{\bar{U}b} = 64.4$

4.3.2 Staggered Array Results

In addition to the four Inline array geometries, three Staggered array geometries were considered. These geometries are described in Table 4.1 and Figure 4.1. In each case the simulation was performed on a computational domain containing two bodies and using periodic boundary conditions to model an infinite array. It should be observed that the bodies used in the Staggered 1 array are of slightly different dimension than those used for the Inline and remaining Staggered cases.

A streamline plot of the laminar base flow solution for the Staggered 2 array at $Re_{\bar{U}b} = 64.4$ is shown in Figure 4.8. For clarity the solution is plotted over four computational cells. The laminar flow solutions for the other two staggered cases are qualitatively similar. It may be observed that, as for the Inline arrays, the laminar flow solution is steady, symmetric about each body, has a stagnation point along the front face, and a recirculation region behind each body. However significant differences between the Inline and Staggered arrays exist in the wake region, as shown by the profiles of u velocity in Figure 4.9. These profiles can be seen to lack the simple sinusoidal shape observed for the Inline arrays. This is a result of the wake region of each body being bracketed by a pair of bodies in the downstream column of the array. The resulting profile of the u velocity in the wake region is double peaked with a velocity defect in the center produced by the upstream body. The streamwise velocity in the initial profile (Profile 0) along the trailing edge of the body is very close to zero in the defect region. However, the magnitude of the velocity defect decreases as the profile is moved downstream.

Table 4.2 lists the critical value of the Reynolds number calculated for each of the three Staggered Array geometries. In comparison to the inline cases the staggered arrangement is observed to be

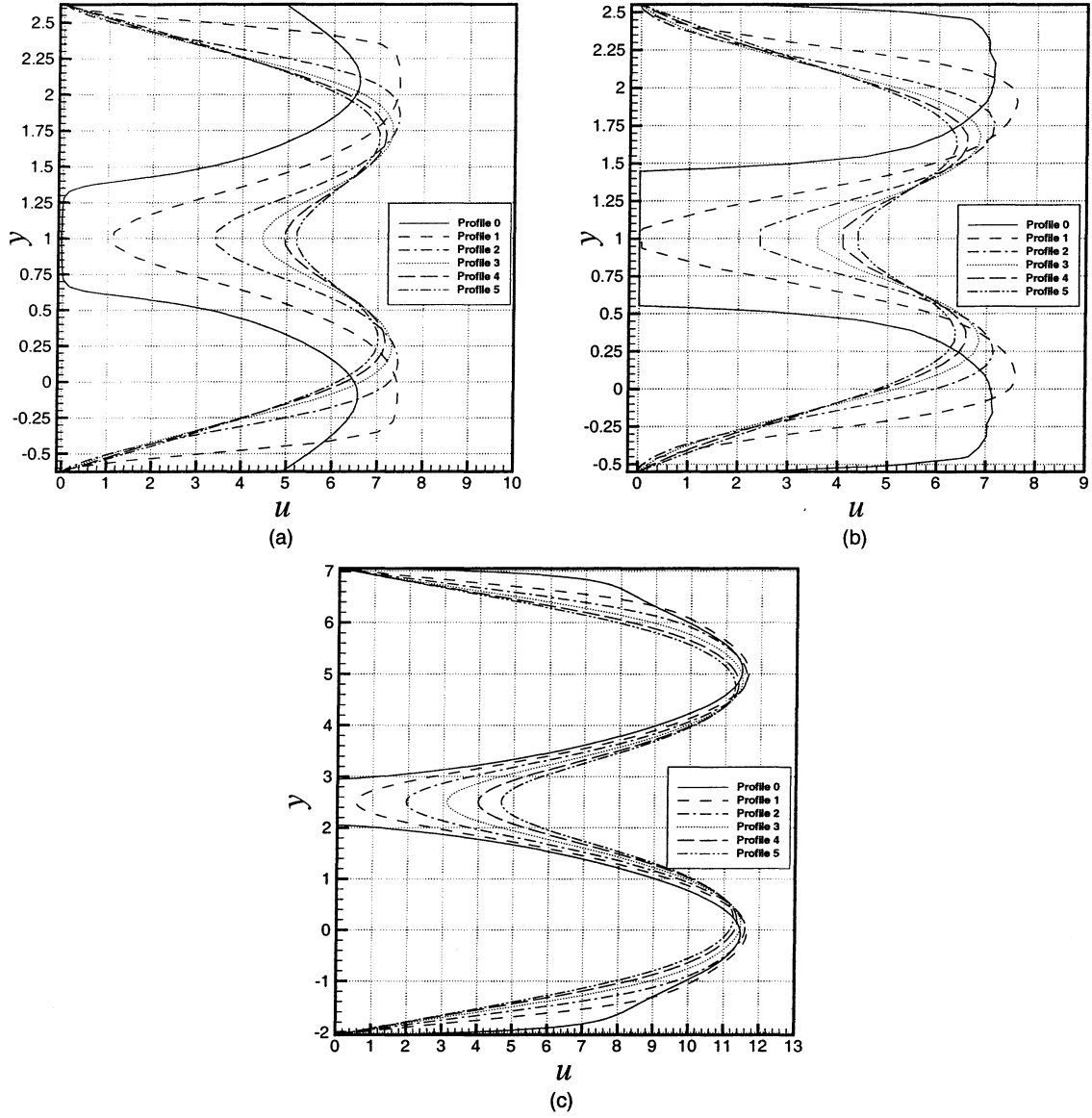


Figure 4.9: Profiles of u velocity for Cases (a) Staggered 1 at $Re_{\bar{U}_b} = 53.4$, (b) Staggered 2 at $Re_{\bar{U}_b} = 64.4$, and (c) Staggered 3 at $Re_{\bar{U}_b} = 25.8$

generally more stable, with a critical Reynolds numbers, $Re_{\bar{U}b}$, of 48.6, 60.9, and 25.8 for cases Staggered 1, Staggered 2, and Staggered 3, respectively. The Staggered 2 geometry is essentially the Inline 1 geometry, but with every other row of bodies offset by a body length in the streamwise direction. The body dimensions and transverse spacing are otherwise the same for the two cases. The Staggered 2 case has a critical Reynolds number of 60.9 and is significantly more stable the Inline 1 case, which has a critical Reynolds number of 31.4.

As with an Inline array the Reynolds number, defined using average flow velocity \bar{U} and body thickness b , is not the only parameter which determines the onset of flow instability in a staggered array. In comparing the values of the critical Reynolds number for the Staggered 2 and Staggered 3 arrays it can be seen that, as with the Inline arrays, the transverse spacing of the bodies has a significant impact on the value of the critical Reynolds number. The increased transverse spacing of the Staggered 3 array over the Staggered 2 array causes a more than fifty percent drop in the value of the critical Reynolds number, $Re_{\bar{U}b}$, from 60.9 to 25.8. The change in transverse spacing is also effects the value of the streamwise wavelength, λ_x , which is 3.7 for the Staggered 2 array and 7.2 for the Staggered 3 array.

The eigenfunctions for the two staggered array cases Staggered 2 and Staggered 3 are shown in Figures 4.10 and 4.11. Both eigenfunctions posses the characteristics of a wake instability, with a line of vortices formed behind the trailing edge of each object- as is seen in the disturbance form for the isolated bodies shown in Figures 4.15 and 4.16. In addition to the primary set of wake vortices, the eigenfunction for the Staggered 2 case shows a weak set of secondary vortices occurring near the primary vortices, similar to what is seen for the Inline array and isolated body disturbances. Furthermore, a third set of vortices is present and appear to be generated from the leading edge of the body. In contrast the Staggered 3 eigenfunction has a somewhat different form. In addition to the primary wake vortices a second set of vortices are present which line up in the streamwise direction between each row of bodies in the staggered array. Again it should be noted that the eigenfunctions represents the form of the disturbance while it is small in amplitude, and before the effects of non linear saturation.

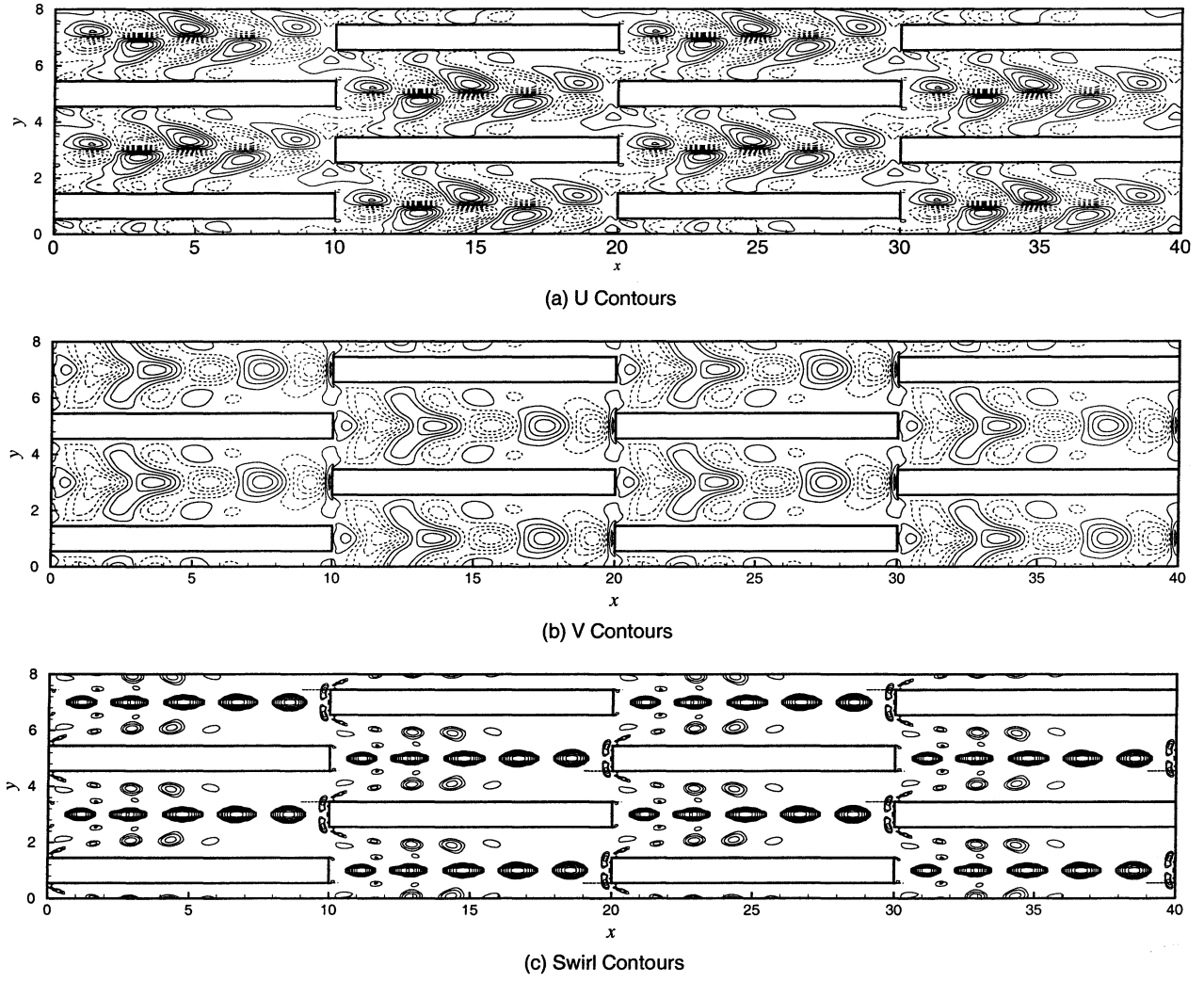
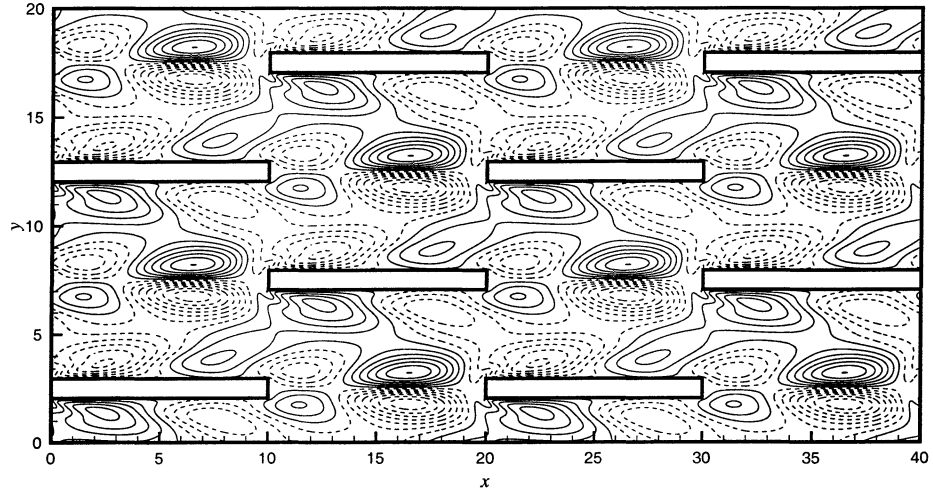
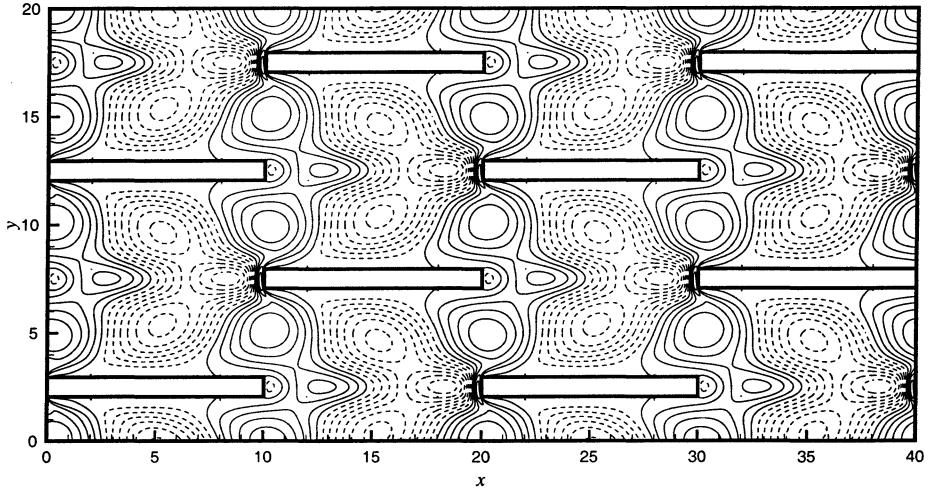


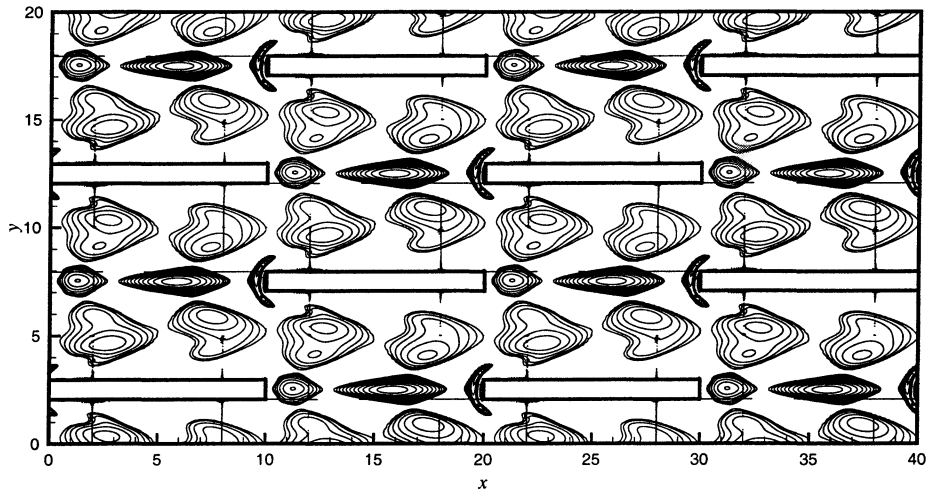
Figure 4.10: Perturbation for Staggered 2 Case at $Re_{\bar{U}b} = 64.4$



(a) U Contours



(a) V Contours



(c) Swirl Contours

Figure 4.11: Perturbation for Staggered 3 Case at $Re_{\bar{U}b} = 41.8$

4.3.3 Non-periodic Results

In addition to the Inline and Staggered array cases, stability results have also been computed for four Non-periodic cases. These cases serve to provide information on the stability of developing flow through arrays and allow the similarities and differences of the flow stability of arrays and isolated objects to be examined.

Two of the four Non-Periodic cases involve flow over a single isolated object. These cases are labeled Rectangular XY Non-Periodic and Square XY Non-Periodic in Table 4.1, where the details of their geometry are described. The case Rectangular XY Non-Periodic involves flow over an isolated body having the same dimensions as the Inline array bodies. The computational domain was chosen to be finite, but large enough to minimize its effect on the flow solution. For this flow a uniform inflow condition is applied along the upstream boundary, while the outflow boundary condition described in Section 2.2.3 is used at the downstream boundary. Along the transverse boundaries the far field boundary condition given by Equation 2.3 is applied. Similarly, the case Square XY Non-periodic involves flow around an isolated square object. This case utilizes the same inflow and outflow conditions applied to Rectangular XY Non-periodic; however, along the transverse boundaries the velocity is set to the free stream velocity. In the context of array flow stability, these isolated cases may be viewed as the limiting case of an array with infinite extent for periodicity along both the streamwise and transverse direction. Further the two cases allow for the assessment of the effect of the body aspect ratio, h/b , on flow stability.

The stability analysis for the isolated cases follows the same procedure applied to the arrays. Streamline plots of the base flows obtained for the two XY Non-periodic cases are shown in Figures 4.12 and 4.13. Both flows demonstrate the symmetry, front face stagnation point, and wake recirculation region observed in all of the array flows. A major difference for the laminar flow around an isolated body can be seen in the profiles of the u velocity in the wake region, which are shown in Figure 4.14. Both solutions show a similar set of velocity profiles which are also similar to the profiles in the wake of a flat plate (Hannemann and Oertel [17]). In each profile a pronounced velocity defect is observed in the region directly behind the object. Moving out of the defect region in the transverse direction, the u velocity rapidly increases until it reaches a peak value moderately above the free stream velocity. Continuing away from the body in the transverse direction the

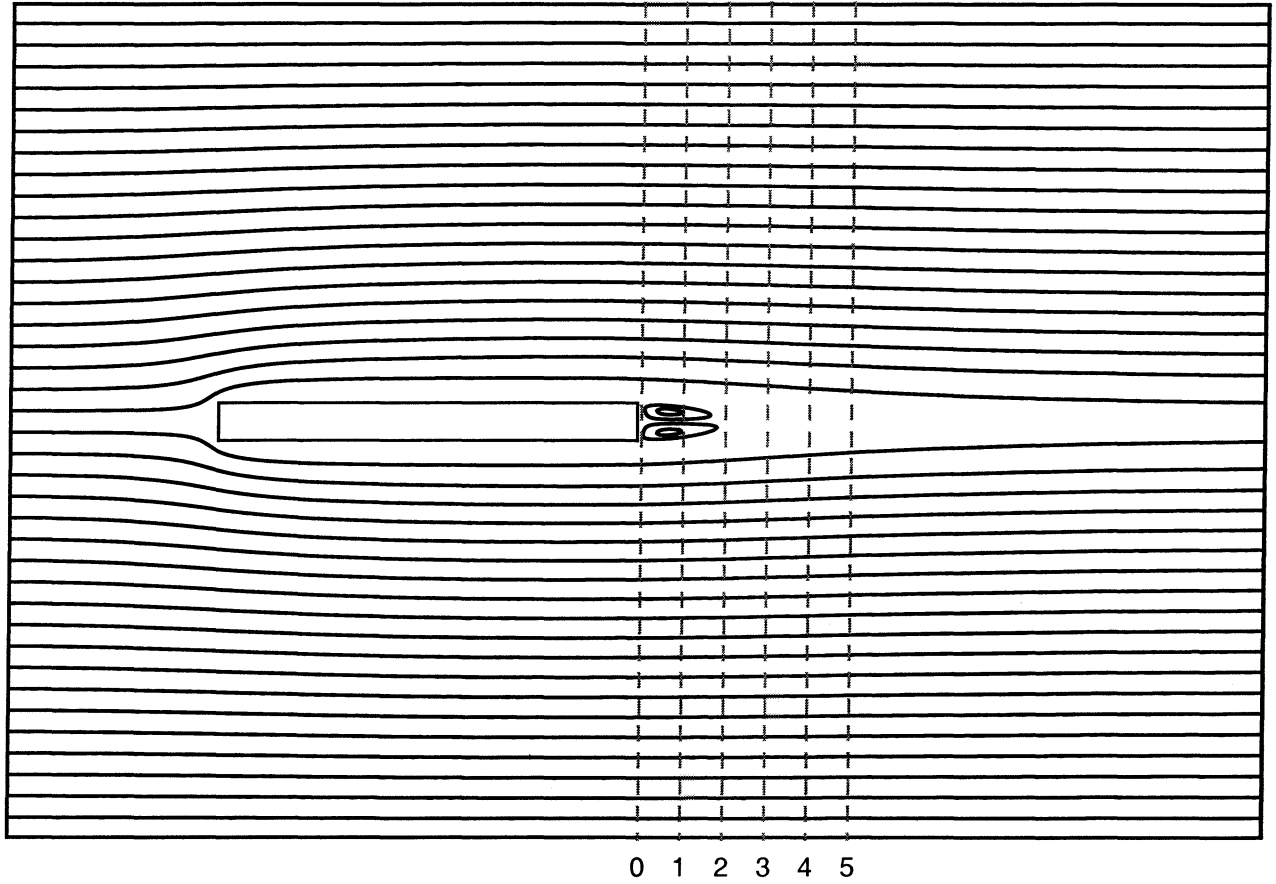


Figure 4.12: Streamlines for Case Rectangular XY Non-Periodic at $Re_{\bar{U}b} = 112.5$

velocity slowly decreases to approach the free stream value. These profiles contrast with those seen for the Inline and Staggered arrays as they lack either sinusoidal periodicity of the Inline arrays or the double peaked shape observed for the Staggered cases. Since the shape of the velocity profile in the wake region plays a significant role in determining the stability of the flow, difference in the stability of isolated bodies and array flows are expected.

The critical Reynolds numbers for the two cases were calculated and determined to be $Re_{\bar{U}b} = 111.6$ for the Rectangular XY Non-periodic case, and 43.5 Square XY Non-periodic case. It is evident that the aspect ratio of the body has a strong influence on the stability of the flow. Furthermore, comparing the Reynolds numbers listed in Table 4.2, it is quite clear that an array of rectangular cylinders is far less stable than an isolated rectangular cylinder. This difference in stability is not unexpected given the differences in the base flow profiles between the arrays and the isolated cases. These critical values of the Reynolds number for an isolated body establish a

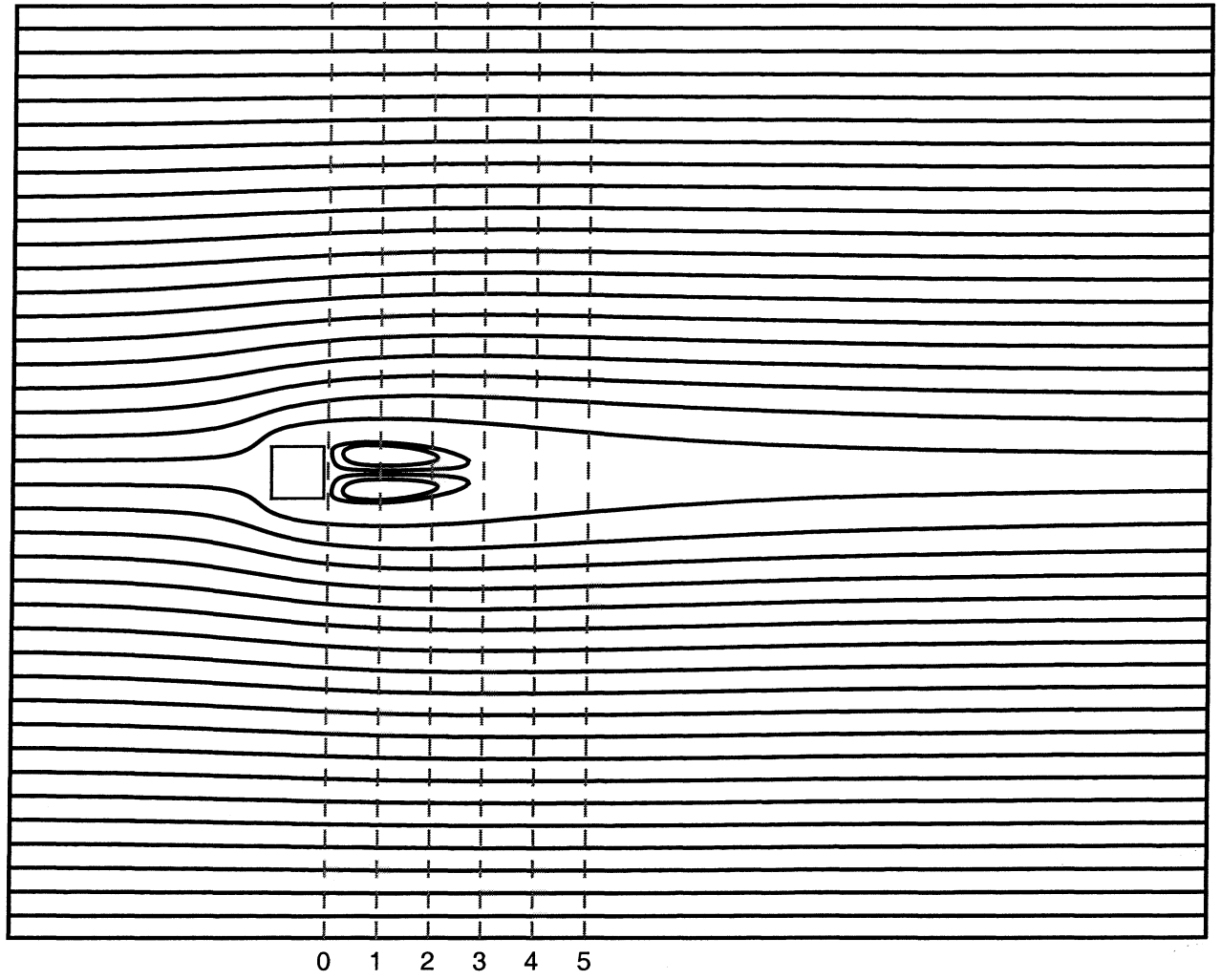


Figure 4.13: Streamlines for Case Square XY Non-Periodic at $Re_{\bar{U}b} = 45.0$

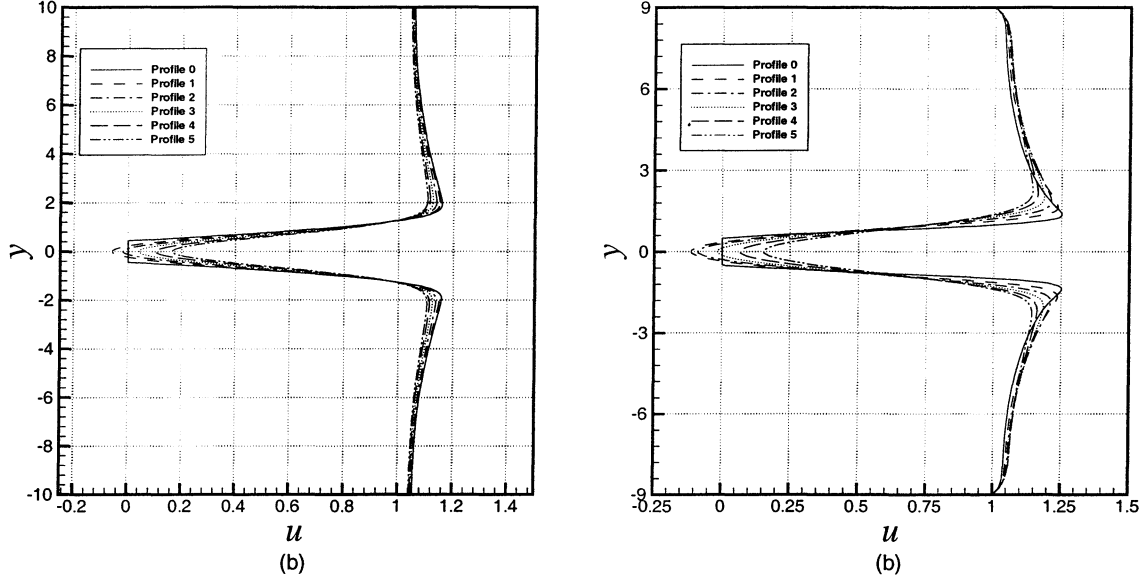
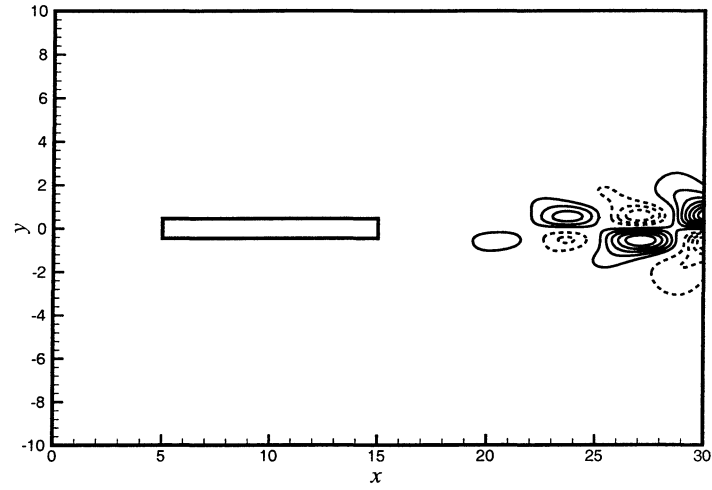


Figure 4.14: Profiles of u velocity for Cases (a) Rectangular XY Non-Periodic at $Re_{\bar{U}b} = 112.5$ (b) Square XY Non-Periodic at $Re_{\bar{U}b} = 45.0$

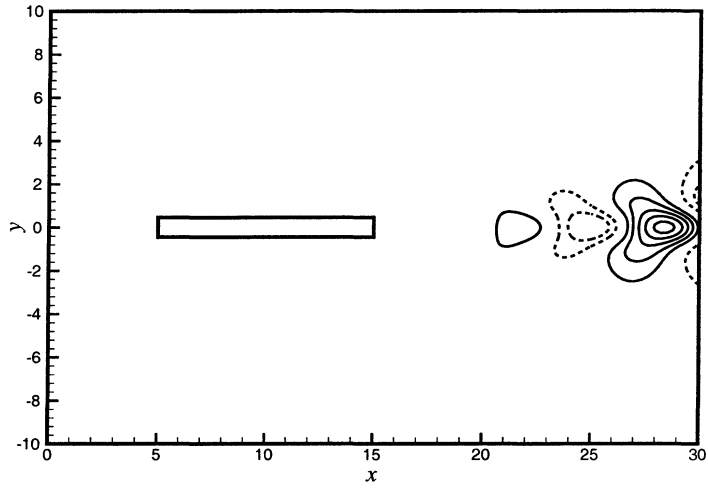
limiting value for the critical Reynolds number of an array of similar objects in the limiting case of very large streamwise and transverse spacing.

The eigenfunctions of the instabilities for the two isolated cases are shown in Figures 4.15 and 4.16. Despite the differences in the critical Reynolds numbers the eigenfunctions for the two isolated cases show a high degree of similarity to each other, and to the eigenfunctions of the Inline and Staggered arrays. For both eigenfunctions the plots of the swirl contours show a distinct image of vortices lined up in the streamwise direction and beginning directly behind the body. Additionally both eigenfunctions show second, smaller, and weaker set of vortices slightly above and below the principal set of vortices. An eigenfunction of this form is characteristic of a wake instability and has also been observed, in terms of disturbance streamlines, for circular cylinders (Jackson [20]) and flat plates (Hannemann and Oertel [17]). Figure 4.17 shows a streamline plot of the disturbance for the case Square XY Non-periodic.

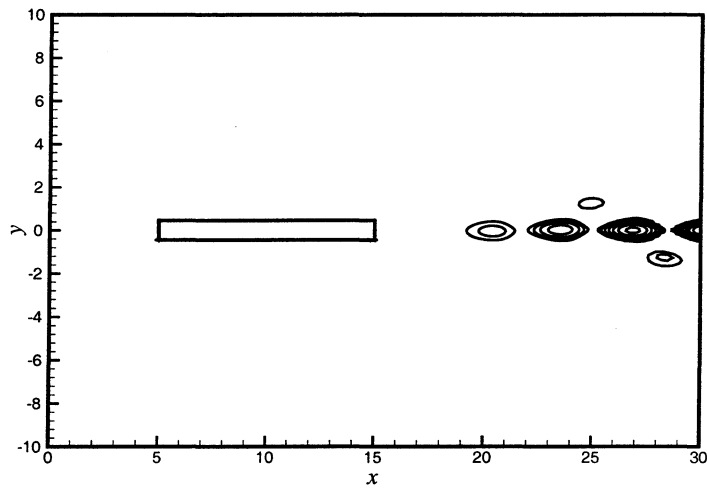
The pronounced variation in critical Reynolds number for the two isolated bodies of differing aspect ratios is consistent with previous observations. The critical Reynolds number for an isolated circular cylinder in cross flow has been well established to be about 47 (Jackson [20]). The corresponding critical Reynolds number for an isolated square cylinder has been found to be about 51 (Sohankar et al [44], Robichaux [42]). In fact, Jackson [20] has considered the onset of periodic



(a) U Contours



(b) V Contours



(c) Swirl Contours

Figure 4.15: Perturbation for Rectangular XY Non-Periodic Case at $Re_{\bar{U}b} = 112.5$

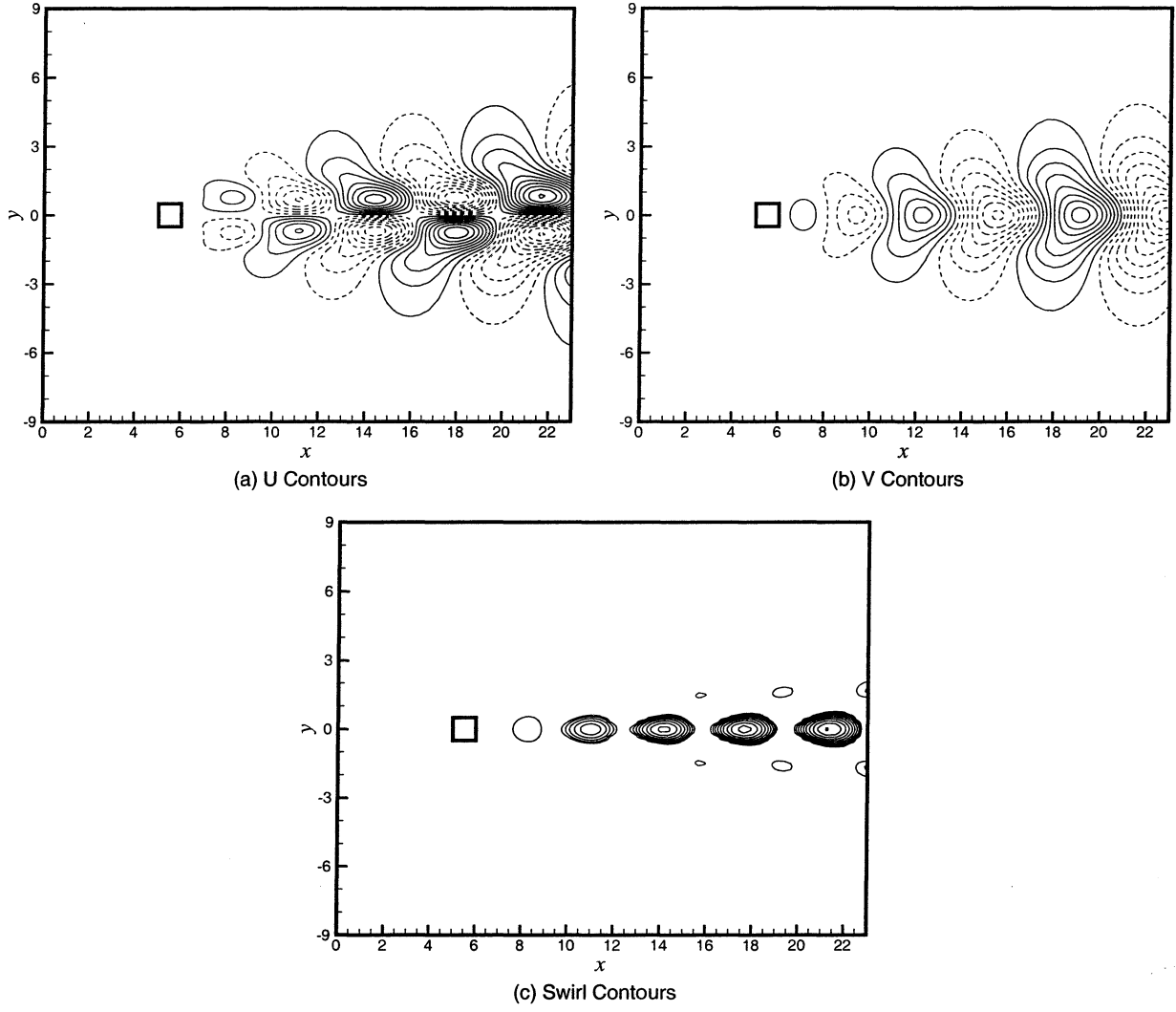


Figure 4.16: Perturbation for Square XY Non-Periodic Case at $Re_{\bar{U}_b} = 45.0$

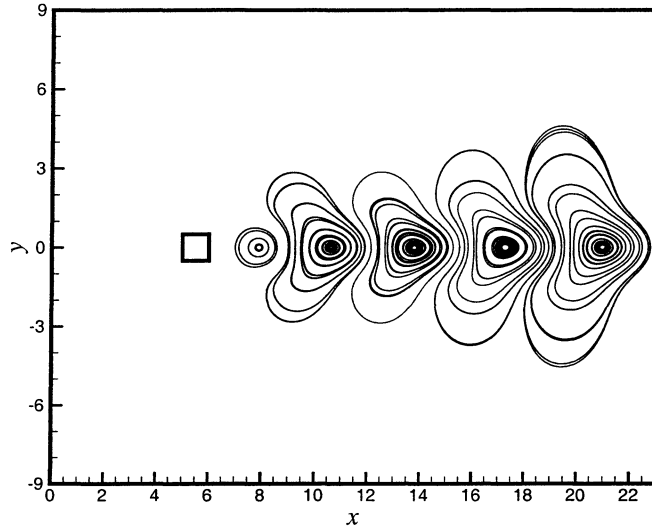


Figure 4.17: Streamline of the perturbation for Square XY Non-Periodic Case at $Re_{\bar{U}_b} = 45.0$

shedding in a series of elliptic cylinders, whose aspect ratio (streamwise length to cross-stream thickness) was varied from 0 (normal plate) to 2 in a systematic way. For the case of a normal plate the critical Reynolds number was found to be 27.7, and quickly increases as the bluffness of the body decreases to a value of 76.8 for an aspect ratio of 2. The increased stability of the flow with decreasing bluffness of the cylinder is due to the thicker boundary layer compared to the thickness of the body at the point of separation.

This behavior is likely to be the same for rectangular cylinders, such as the ones considered in this work. Therefore, for rectangular cylinders the critical Reynolds number is expected to increase with increasing aspect ratio. In fact, in the limit of the aspect ratio becoming very large we have the case of very thick boundary layers compared to the thickness of the plate. The flow in the wake approaches that of a plane wake and it is well established that a plane wake is only convectively unstable and not absolutely unstable.

In addition to the two isolated body cases, two other Non-periodic cases were considered. These two cases, listed in Table 4.1 as Rectangular X Non-periodic and Square Non-periodic, use an inflow condition at the upstream boundary and an outflow condition at the downstream boundary. In the transverse direction a periodic boundary condition is applied. This produces a simulation of flow over single infinitely long column of bodies. The Rectangular case employs the same rectangular

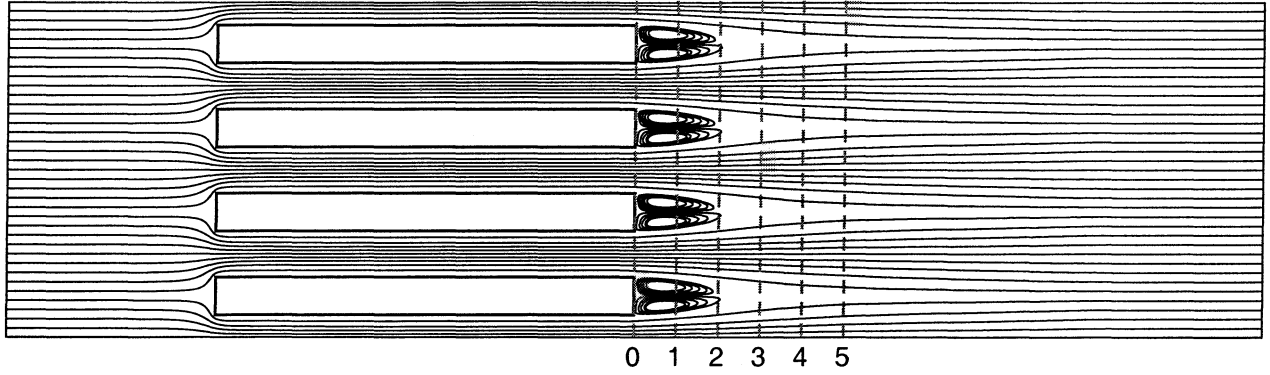


Figure 4.18: Streamlines for Case Rectangular X Non-Periodic at $Re_{\bar{U}b} = 31.5$

body used in the Inline, Staggered 2, and Staggered 3 cases, while the Square case uses a square body.

These cases allow for further investigation into the effects of streamwise spacing and body aspect ratio on the stability of the flow. Furthermore, a consideration in the interpretation of the Inline and Staggered results is that the application of the streamwise periodic boundary condition used in the simulation has the effect of feeding-back the disturbance from the exit of the computational domain to the inlet. It must, therefore, be ascertained that the absolute instability observed in the array cases is a genuine property of the wake flow and not an artifact of the periodic boundary condition imposed. These X Non-periodic cases will serve to validate the origin of the absolute instability, as there is no explicit feed-back of the disturbance from the outflow to the inlet.

Figures 4.18 and 4.19 show the streamline of the laminar base flow for the two cases. While Figure 4.20 shows the wake velocity profiles. These profiles may be seen to be very similar to each other, and to the profiles of the Inline 1 and Inline 3 cases shown in Figure 4.6. This is principally a result of the rapid development of the parabolic velocity profile formed in the channel region between the bodies. The parabolic profile may be seen to be well developed even for the Square X Non-periodic case where the oncoming flow is uniform and channel height is the same as the channel width.

Given the similarity of the wake velocity profiles it is not surprising that the critical Reynolds numbers for the two cases are close in value to each other, and to those of the Inline 1 and Inline 3 cases. The Rectangular X Non-periodic case was found to have a critical Reynolds number, $Re_{\bar{U}b}$, of 31.5, while the Square X Non-periodic case has a critical Reynolds number 28.0. This may be

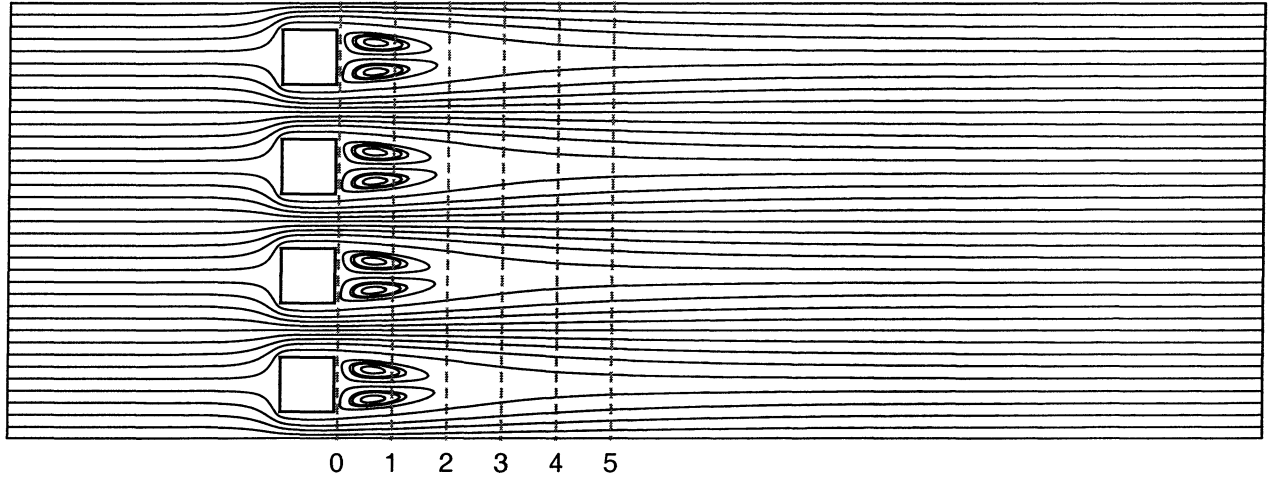


Figure 4.19: Streamlines for Case Square X Non-Periodic at $Re_{\bar{U}_b} = 28.0$

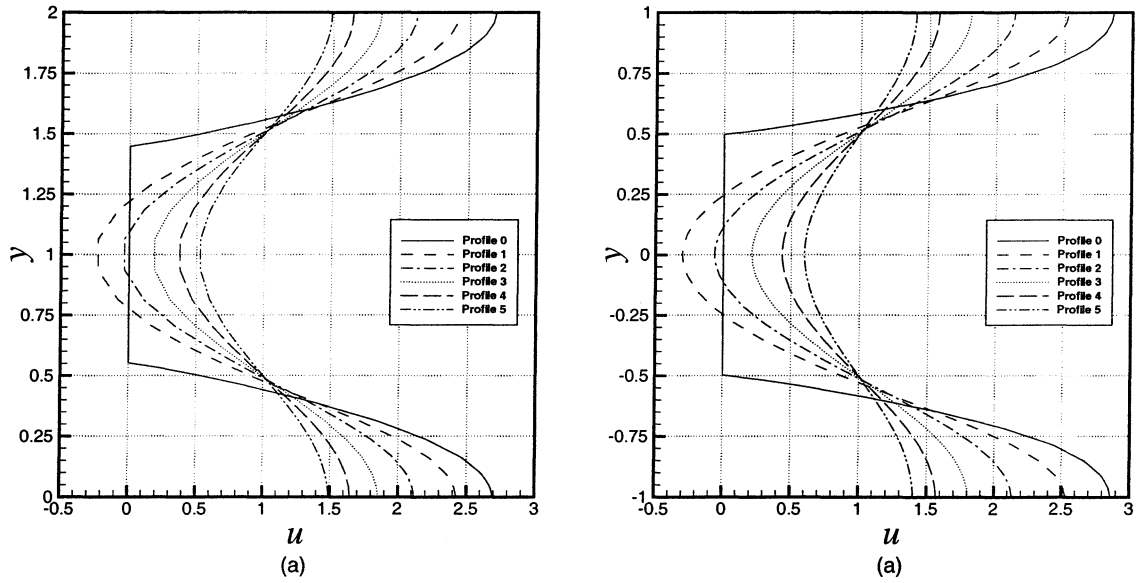


Figure 4.20: Profiles of u velocity for Cases (a) Rectangular X Non-Periodic at $Re_{\bar{U}_b} = 31.5$, and (b) Square X Non-Periodic at $Re_{\bar{U}_b} = 28.0$

compared to the critical Reynolds numbers of 31.4 and 33.8 for the Inline 1 and 3 cases. Since the Rectangular X Non-periodic case may be viewed as a variant of the Inline 1 and Inline 3 cases with infinite streamwise spacing, these results further demonstrate the independence of $Re_{\bar{U}b,crit}$ and λ_x on the streamwise spacing of the array.

The influence of streamwise periodicity on the instability of the base flow can also be assessed. Since the values of the critical Reynolds number of the Rectangular X Non-periodic case are nearly identical to those observed for the Inline 1 and Inline 3 cases, the absolute instability observed in the Inline and Staggered arrays is physical and not due to artificial feedback through the periodic boundary condition. In addition, the influence of the aspect ratio, h/b , on the critical value of the Reynolds number would appear to be minimal as the value of the critical Reynolds number for the Square X Non-periodic case is close to the value for the Rectangular X Non-periodic case, despite an order of magnitude difference in the aspect ratios. Finally, the eigenfunctions for the two cases are shown in Figures 4.21 and 4.22 and can be seen to be similar to those of the isolated bodies and Inline arrays.

4.4 One Dimensional Floquet Stability Analysis

The simplicity of the base flow for the Inline solution cases noted in Section 4.3.1 suggests the possibility of a one dimensional stability analysis of these flows. In this analysis we assume that the base u velocity has the form given in Equation 4.4 and that the base v velocity is identically zero. Given the rapid decay of the Fourier coefficients, consideration will be limited to at most 3 terms in the u velocity expansion. The form of the base velocity in dimensional variables is then

$$\begin{aligned} U^*(y^*) &= c_0^* + c_1^* \cos\left(\frac{2\pi y^*}{L_y^*}\right) + c_2^* \cos\left(\frac{4\pi y^*}{L_y^*}\right) \\ V^*(y^*) &= 0 \end{aligned} \tag{4.5}$$

Furthermore, variation of the base flow in the streamwise direction is neglected. It should be noted that the classical one dimensional stability analysis of wall bounded flows with similar sinusoidal profiles shows that these flows are stable (Drazin and Reid [14]). However the current profile under

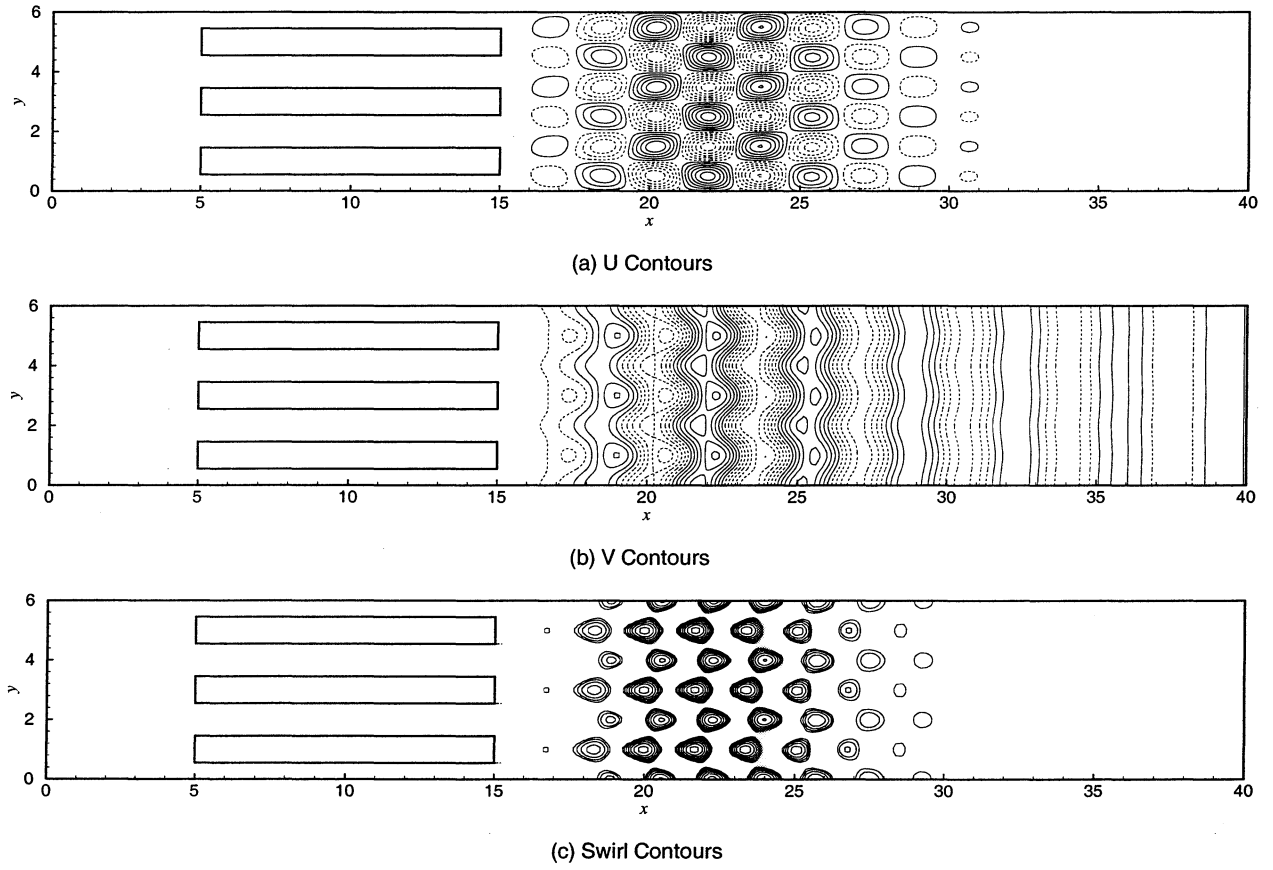
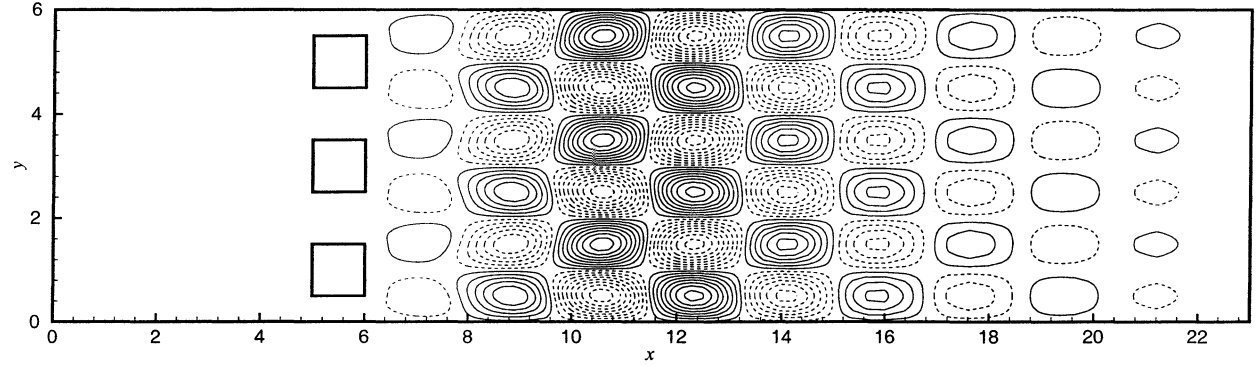
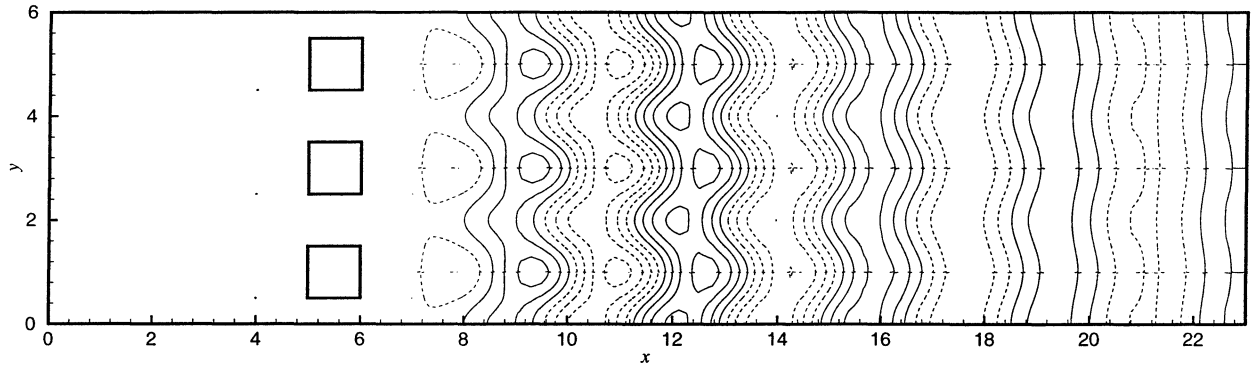


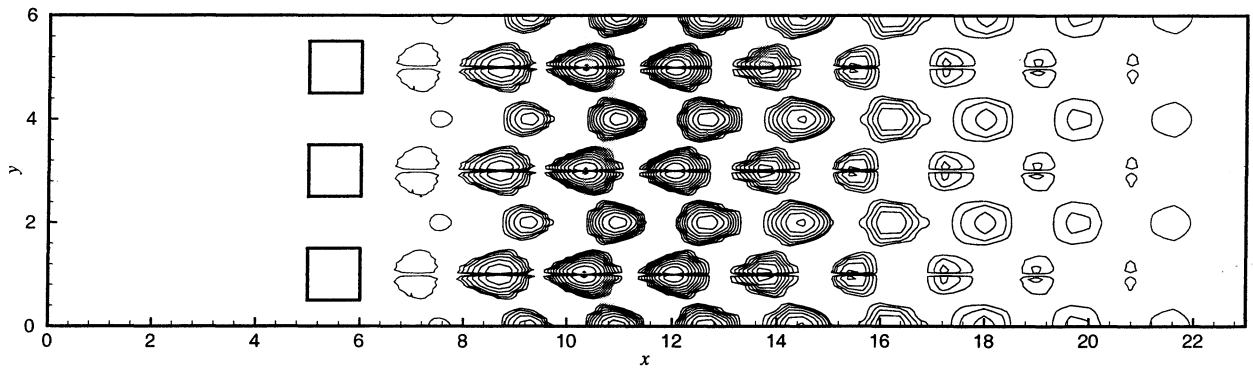
Figure 4.21: Perturbation for Rectangular X Non-Periodic Case at $Re_{\bar{U}_b} = 31.5$



(a) U Contours



(b) V Contours



(c) Swirl Contours

Figure 4.22: Perturbation for Square X Non-Periodic Case at $Re_{\bar{U}_b} = 28.0$

consideration is unbounded in the y direction and thus need not be stable.

Development of the stability equations for the Inline array wake velocity profile follows that of the standard Orr-Sommerfeld equation. The velocity is written as a base component plus a perturbation, as

$$\begin{aligned} u &= U + u' \\ v &= V + v' \end{aligned} \tag{4.6}$$

and the stream function is introduced, which is defined as

$$\begin{aligned} u' &= \frac{\partial \Psi}{\partial y} \\ v' &= -\frac{\partial \Psi}{\partial x} \end{aligned} \tag{4.7}$$

The equation resulting from the linearized non-dimensional Navier - Stokes equations is then

$$\frac{\partial}{\partial t} \nabla^2 \Psi + U \frac{\partial}{\partial x} \nabla^2 \Psi - \frac{\partial^2 U}{\partial y^2} \frac{\partial \Psi}{\partial x} = \frac{1}{Re_{1D}} \nabla^4 \Psi \tag{4.8}$$

The scales chosen for this equation are the amplitude of the sinusoidal oscillation of the streamwise velocity, c_1^* , as the velocity scale and half of the domain height, $L_y^*/2$, as the length scale. Therefore, the Reynolds number Re_{1D} is defined as $Re_{1D} = c_1^* L_y^*/2\nu$

The Normal Mode assumption is made for the stream function- exponential behavior along the streamwise direction and in time are assumed. The periodic nature of the base flow along the y direction allows for a Floquet expansion for the perturbation stream function. Owing to the symmetry of the base flow, the corresponding linear disturbance can be separated into odd and even modes about the centerline, $y = L_y/2$. The odd mode corresponds to an anti-symmetric stream function about $y = L_y/2$ and is given by a sine expansion in y . The corresponding u' and v' velocity distributions will be symmetric and anti-symmetric about $y = L_y/2$. The even mode corresponds to a symmetric stream function and is given by a cosine expansion in y . Instability is expected to appear in the form of a Hopf bifurcation followed by the onset of vortex shedding. Based on the literature on wake flow instability (Oertel [37]), we can expect the unstable mode to be even and

given by a cosine expansion for the stream function. Corresponding odd modes can be expected to be stable. Furthermore, the dominant unstable mode is expected to be two-dimensional, with no variation in the spanwise z direction. Thus, the present stability analysis will be restricted to a two-dimensional disturbance having the form

$$\Psi(x, y, t) = \sum_{j=0}^N (-1)^j \tilde{\Psi}_j \cos(j\pi y) e^{i(\alpha x - \omega t)} \quad (4.9)$$

Substituting the above expansion along with the three-term expansion for the base flow given in Equation 4.5 into Equation 4.8 yields the relation

$$\begin{aligned} & \frac{i\alpha c_2}{2} \left\{ \frac{-[\alpha^2 + (j-2)^2\pi^2] + 4\pi^2}{\alpha^2 + j^2\pi^2} \right\} \tilde{\Psi}_{j-2} \\ & + \frac{i\alpha}{2} \left\{ \frac{[\alpha^2 + (j-1)^2\pi^2] - \pi^2}{\alpha^2 + j^2\pi^2} \right\} \tilde{\Psi}_{j-1} \\ & - \frac{1}{Re_{1D}} \{ \alpha^2 + j^2\pi^2 \} \tilde{\Psi}_j \\ & + \frac{i\alpha}{2} \left\{ \frac{[\alpha^2 + (j+1)^2\pi^2] - \pi^2}{\alpha^2 + j^2\pi^2} \right\} \tilde{\Psi}_{j+1} \\ & + \frac{i\alpha c_2}{2} \left\{ \frac{-[\alpha^2 + (j+2)^2\pi^2] + 4\pi^2}{\alpha^2 + j^2\pi^2} \right\} \tilde{\Psi}_{j+2} = -i(\omega - \alpha c_0) \tilde{\Psi}_j \end{aligned} \quad (4.10)$$

For a temporal stability analysis the frequency of the disturbance, ω , is considered to be complex having real, ω_r and imaginary, ω_i components. The above algebraic system constitutes a regular eigenvalue problem for linear, temporal stability analysis, of the form

$$A\psi = \lambda\psi \quad (4.11)$$

where A is an $N \times N$ matrix, ψ is the vector of eigenmodes, and λ is the eigenvalue, defined as

$$\lambda = -i(\omega - \alpha c_0) \quad (4.12)$$

The existence of a growing mode is dependent on the eigenvalue of the matrix A which is characterized by the parameters α , $c_2 = c_2^*/c_1^*$, and Re_{1D} . The parameter α measures the streamwise wavenumber of the disturbance and the ratio c_2^*/c_1^* measures the level of higher harmonics present

c_2^*/c_1^*	$Re_{1D,crit}$
0.0	4.44
-0.1	4.44
-0.2	4.42
-0.4	4.36

Table 4.5: Critical Reynolds Number from One Dimensional Stability Analysis

in the base flow. The three term expansion for the base flow results in a penta-diagonal system for the eigenvalue problem shown in Equation 4.10. If we carefully ignore the higher harmonics, which are deviations from the pure sinusoidal profile, by setting $c_2 = 0$, then the first and the last terms on the left hand side of Equation 4.10 reduce to zero, thus resulting in a tridiagonal system for the eigenvalue problem. Alternatively, if the higher harmonics play an important role, then the base flow expansion needs to retain more terms and correspondingly the bandwidth of the eigenvalue system will increase. In the present case, we have already seen that the deviation from the pure sinusoidal profile for the base flow is not significant. Furthermore, we will show that below even modest values for the higher harmonic ratio c_2^*/c_1^* does not change the nature of the instability significantly.

Figure 4.23 shows the calculated instability growth rate as a function of α for several Re_{1D} numbers and two values of c_2 . From Figure 4.23 it can be seen that the value of c_2 has only marginal impact on the stability results, especially close to the critical Reynolds number. Further evidence of the independence of the results with respect to c_2^*/c_1^* can be seen in Table 4.5, which shows the critical Re_{1D} for several values of c_2 . The value of the critical Re_{1D} can be seen to vary little with the value of c_2 over the range considered. It is therefore possible to consider the flow stability to be determined by the pure sinusoidal base flow profile and controlled by the two remaining parameters α , and Re_{1D} .

It can be seen that for each Re_{1D} number the growth rate peaks at a specific α value. From Figure 4.23 data, the critical Re_{1D} number value is found to be 4.44 with an associated α value of approximately 0.2π . With the Reynolds number defined as $Re_{1D} = c_1^* L_y^* / 2\nu$, flow stability is governed by the amplitude of the U profiles variation in y , c_1^* , and not the average U velocity, c_0^* , which acts as the convective velocity of the perturbation. However, for the base flows considered the primary Fourier coefficient, c_0^* , and the secondary coefficient, c_1^* , are generally of similar value,

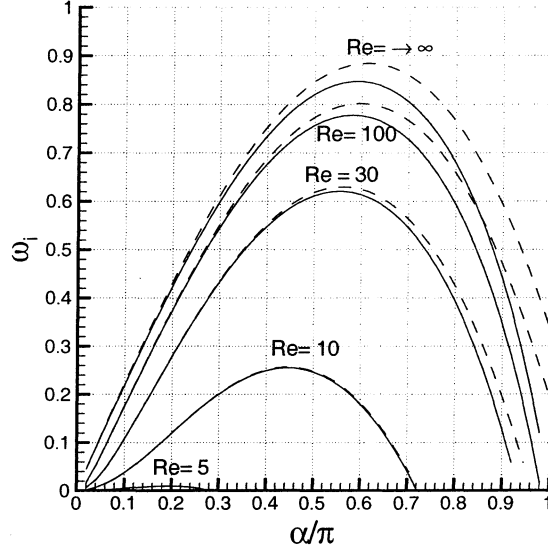


Figure 4.23: One Dimensional Stability Analysis Growth Rate for $c_2 = 0.0$ (Solid line), and $c_2 = -0.1$ (Dashed line)

particularly close to the trailing edge of a column of bodies, as is shown by Table 4.4. This will generally be true of any sinusoidal base flow generated by an array of bluff bodies, since the minimum streamwise velocity will be close to zero in the near wake region. Thus, the critical Reynolds number for this analysis will be a similar value whether c_0^* or c_1^* is used for the velocity scale.

It is also important to note that the length scale used is that of the periodic cell height, or maximum wavelength in the y direction, L_y^* , and not the body height b^* , which is commonly used for bluff body flows. As a consequence the body height b^* has no direct impact on the stability of a sinusoidal base flow. As mentioned in Section 4.3.1, extreme values of the ratio of the inter-body channel height to body height, c/b , and correspondingly L_y/b , could result in a base flow lacking a simple sinusoidal nature. However, these cases fall outside the range of cases considered for this work.

When proper scaling adjustments are made and the critical values of the Reynolds numbers from the 1D and 2D analysis are compared it is found that the critical Reynolds number determined from the one dimensional stability analysis is significantly lower than that found in the 2D analysis. Furthermore, the 1D analysis predicts a wavenumber of $\alpha = 0.2\pi$ for the perturbation, while the

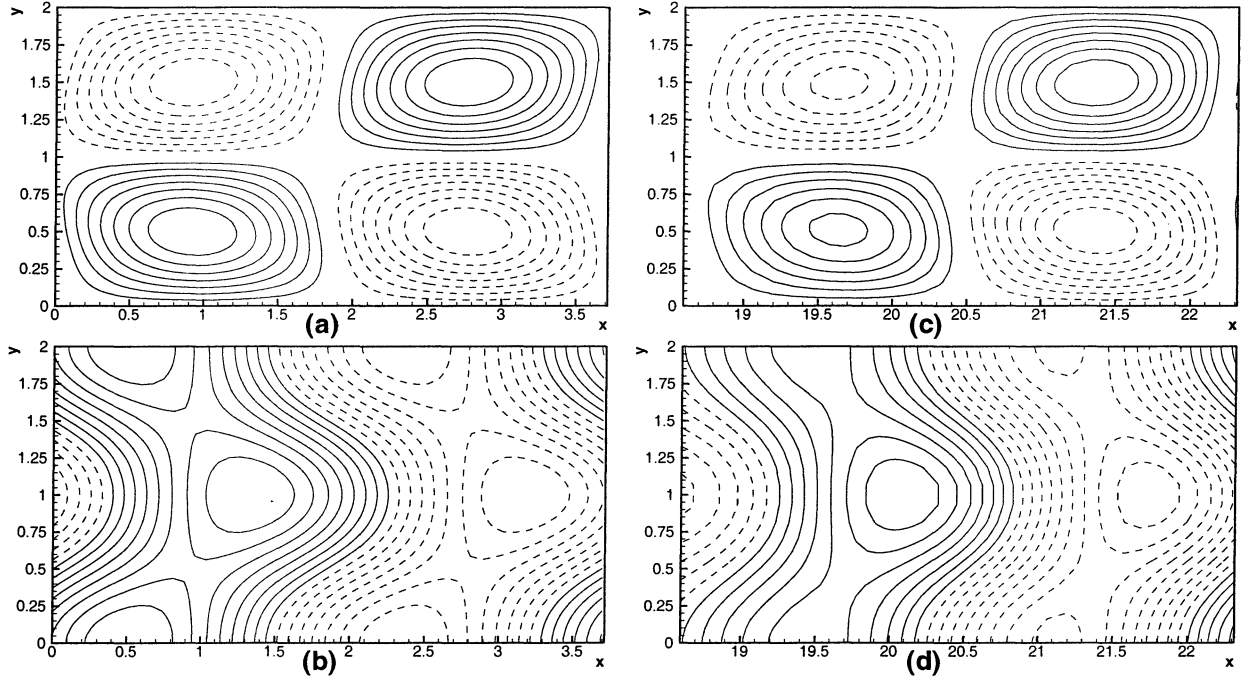


Figure 4.24: Stability Analysis Eigenfunction- Figures (a) and (b) show contours of the u and v velocities respectively for the 1D eigenfunction. Figure (c) and (d) show similar results for the 2D Inline 1 eigenfunction.

2D analysis shows a wavenumber of $\alpha = 0.55\pi$ for a similar scaling. However, the eigenfunction for the least stable mode in the 1D calculations is shown in Figure 4.24 and compared to the unstable mode found in the 2D results for the same values of Re and α . Shown are contours of u' and v' velocity, over a comparable $x - y$ range, with the dashed lines indicating negative contour values. The results show a nearly identical structure of the eigenfunction for the two different stability analyses. This would indicate that the one and two dimensional analyses are identifying the same fundamental instability. The discrepancy in the critical values of the Reynolds number and wave number between the two analysis is most likely due to the evolution of the base flow along the streamwise direction in the 2D case limiting the range in Reynolds number and wave number at which the instability can grow. Similar correspondence between the full two-dimensional and one-dimensional wake profile stability analysis can be seen in the case of an isolated bluff body. Thus, while not quantitatively predictive the one-dimensional stability analysis can be used to gain insight into the effect of various parameters on the stability of sinusoidal base flows of the type generate by in-line arrays.

Case	Re_{c_1, L_y}	$Re_{\bar{U}_{chan}, L_{wake}}$
Inline 1	93.5	127
Inline 2	98.4	129
Inline 3	103.7	137
Inline 4	94.8	125
Staggered 1	-	130
Staggered 2	-	135
Staggered 3	-	144
Rect. X Non-Periodic	92.8	127
Square X Non-Periodic	79.2	112

Table 4.6: Critical Reynolds Numbers for the Numerical Solution Cases

4.5 Rescaling and Parametric Dependence

In this section we will use the results of the two dimensional numerical stability analysis in Section 4.2 and the one dimensional analysis of Section 4.4 to develop a more general understanding of flow stability in Inline and Staggered arrays. An alternate scaling for use in Inline and Staggered arrays is developed and applied to the numerical stability results described earlier. After which the effect of each of the array parameters on the stability of the flow is discussed.

4.5.1 Rescaling

The one dimensional analysis of Section 4.4 suggests a possible alternate scaling that may be applied to the Inline array cases. Instead of a Reynolds number, $Re_{\bar{U}b}$, based on the average velocity \bar{U}^* , defined by Equation 4.3, and the body thickness b^* , a Reynolds number, Re_{1D} , based on the amplitude of the sinusoidal oscillation, c_1^* , and the transverse wavelength L_y^* may be used. Using this scaling, with the amplitude of the oscillation c_1 estimated from the second extracted velocity profile (Profile 1) for each case, the critical values of the Reynolds number for the Inline and X Non-periodic cases have been calculated and are shown in Table 4.6. The result is a close agreement in the value of the critical Reynolds for all of the rectangular body cases, with the average value being 96.6.

It should be noted that the value of c_1 is not well determined, since the amplitude of the sinusoidal oscillation decays as the profile moves downstream, as can be seen in Figure 4.6 and Table 4.4. Therefore the value of c_1 will vary with the choice of profile. An alternative is to make

a reasonable estimated of the oscillation amplitude based on the physics of laminar wake flow. For any flow over a bluff body, there will exist a recirculation region directly behind the body in which the streamwise velocity is close to zero. Furthermore for in any Inline or Staggered array the flow at the trailing edge of a body will be exiting a region of channel flow and therefore have an approximately parabolic profile. Given this parabolic profile, the peak velocity of the exiting channel flow is

$$\bar{U}_{max} = \frac{3\bar{U}_{chan}}{2} \quad (4.13)$$

with

$$\bar{U}_{chan} = \frac{\bar{Q}_x}{L_y - b} \quad (4.14)$$

where \bar{Q}_x is the net volumetric flow rate through the array. Therefore, with the flow at the trailing edge of each body having a peak velocity of \bar{U}_{max} and a minimum velocity of approximately zero in the recirculation region, a reasonable estimate of the amplitude of the sinusoidal oscillation is

$$c_1 \approx \frac{\bar{U}_{max}}{2} = \frac{3\bar{U}_{chan}}{4} \quad (4.15)$$

therefore

$$c_1 \propto \bar{U}_{chan} \quad (4.16)$$

Equation 4.16 says that the value of the oscillation amplitude, c_1 , scales like the average velocity in the region of channel flow, \bar{U}_{chan} . The velocity \bar{U}_{chan} may then be used as the scaling for the Reynolds number.

The results of the 1D theory have direct application only to the Inline array cases, where the flow in the wake region is periodic in the transverse direction. However, the flow in the wake region for the Staggered arrays shares important similarities with that of the Inline arrays, as may be seen by comparing the profiles of u velocity in Figures 4.6 and 4.9. In all of these cases a region of near zero velocity can be observed along the center line of the body, in the profiles close to the trailing

edge. Moving away from the center line in the transverse direction the velocity smoothly increases past a point of inflection and on to a peak value, from which it then decays back to a value close to zero. With the stability of the flow principally determined by the profile of the U velocity in the wake region, these similarities suggest the scalings applied to Inline arrays may also be applicable to Staggered geometries. Furthermore the eigenfunctions of the instabilities are most active along the body centerlines in the wake region, where the similarities in the profiles are most pronounced.

The Inline arrays use a length scale, L_y , corresponding to the wavelength of the primary sinusoidal oscillation in the U velocity along the transverse, y , direction. Since the profiles of the U velocity in the wake region of a Staggered array are not periodic a modified length scale must be considered. A reasonable choice for this scaling would be the distance between the peaks in the velocity profile of the staggered array. The precise value of the peak to peak distance in a staggered array is not easily determined as it varies depending on the location of the velocity profile, as is seen in Figure 4.9. However it may be argued that this distance should scale with the width of the channel region containing the wake profile.

Therefore, a Reynolds number may then be defined as

$$Re_{\bar{U}_{chan}, L_{wake}} = \frac{\bar{U}_{chan} L_{wake}}{\nu} \quad (4.17)$$

where

$$L_{wake} = \begin{cases} L_y & \text{Inline Array} \\ c/2 & \text{Staggered Array} \end{cases} \quad (4.18)$$

The critical Reynolds numbers for all of the non-isolated numeric solution cases have been recalculated using this definition of the Reynolds number and are shown in Table 4.6. The result of the rescaling is a good collapse of the value of the critical Reynolds number for the Inline and Non-periodic cases to a value of approximately 126, while the Staggered cases collapse to a similar value of approximately 136.

Case	$Re_{\bar{U}_{chan}, L_{wake}}$	h^*/L_{wake}^*	b^*/L_{wake}^*	s^*/L_{wake}^*
Inline 1	127	5.00	0.450	5.0
Inline 2	129	2.50	0.225	2.5
Inline 3	137	5.00	0.450	10.0
Inline 4	125	2.50	0.225	5.0
Staggered 1	130	1.97	0.231	0.243
Staggered 2	135	3.23	0.290	0.0
Staggered 3	144	1.10	0.099	0.0
Rect. X Non-Periodic	127	5.00	0.450	∞
Square X Non-Periodic	112	0.50	0.500	∞

Table 4.7: Values of the Non-dimensional parameters for the Inline, Staggered, and X Non-Periodic Cases

4.5.2 Parameter Dependence

From Figure 4.1 it is clear that a range of parameters are at play in the case of an array of rectangular cylinders. These parameters are the transverse pitch (s^*), the streamwise pitch (c^*), the body thickness (b^*), the body length (h^*), the type of arrangement (Inline or Staggered), as well as the flow rate through the array (\bar{Q}_x^*), and the physical properties of the fluid. Using the numerical results, the analytic one dimensional analysis, and the Reynolds number defined above we are now in a position to discern the role played by each of these parameters in determining the stability of the flow. The set of parameters listed above may be recast as a set of non-dimensional parameters determined by the choice of length and velocity scales. Based on the arguments presented above, \bar{U}_{chan}^* is chosen as the velocity scale and L_{wake}^* is chosen for the length scale. The set of non-dimensional parameters relevant to the stability of the flow is then $Re_{\bar{U}_{chan}, L_{wake}}$, s^*/L_{wake}^* , b^*/L_{wake}^* , and h^*/L_{wake}^* . The value of all of these non-dimensional quantities for each of the Inline, Staggered, and X Non-periodic solution cases is shown in Table 4.7.

The close agreement in the value of the critical Reynolds number for all of the Inline and Staggered cases indicates this is the dominant parameter in determining the stability of the flow. The similarity in the critical values of the Reynolds number for the Inline and Staggered cases indicates that both arrangements are subject to the same basic type of instability. As long as the wake profile remains approximately sinusoidal for the Inline cases, as shown in Figure 4.6, and double peaked for the Staggered, as shown in Figure 4.9, one can expect the Reynolds number to primarily control the stability of the flow.

The properties of the base flow are principally determined by the geometric parameters s^*/L_{wake}^* , b^*/L_{wake}^* , and h^*/L_{wake}^* . Of these, the parameter that has the most pronounced influence is the ratio h^*/L_{wake}^* . This parameter has the most direct effect on the degree to which the sinusoidal and double peaked velocity profiles are generated. For a fixed value of h^* , the sinusoidal and double peaked profiles (Regime I) can be expected to exist until a limiting transverse pitch, say L_{wake}^1 is reached. At transverse spacing larger than this limiting L_{wake}^1 the wake profile begins alter.

For values of L_{wake} greater than L_{wake}^1 the viscous effects along the channel wall do not propagate deeply enough across the channel to have a dominant influence on the flow. In this flow regime, Regime II with ($L_{wake} > L_{wake}^1$) the flow will become more stable, as one expects to recover the stability result for an isolate case in the limit of very large transverse pitch. Table 4.2 shows that isolated bodies are more stable, in terms of the Reynolds number $Re_{\bar{U}b}$ which is based on the body thickness (b). Finally a third regime (Regime III) can be defined for large values of transverse pitch, where the stability of the flow is no longer influenced by the value of the transverse pitch. The stability of the flow is now the same as for an isolated body, where only the geometric parameters h^* and b^* are applicable.

As shown by the results of Inline and X-Non-periodic cases, the streamwise pitch in general neither alters the critical Reynolds number, the structure of the eigenfunction, nor is it expected to greatly affect the base flow. The only exception could be when the streamwise gap (s^*) between two columns of bodies is not sufficient for the development of wake instability. As a rough estimate one can expect the instability to be suppressed when this streamwise gap becomes less than the transverse spacing between the bodies. It must be noted here that the streamwise wavelength of the disturbance obtained from both the one-dimensional theory and the two-dimensional stability computations scales with transverse spacing (provided $L_{wake} < L_{wake}^1$) and not with the body thickness. Thus for streamwise gap greater than transverse spacing, $s^*/L_{wake}^* > 1$, the influence of streamwise pitch is not likely to be significant.

It must be cautioned that the above discussion is pertaining to only the onset of wake vortex shedding. As will be shown in later chapters, the wake vortices once formed can trigger the formation of leading edge vortices when they encounter the leading edges of the next column of bodies. These leading edge vortices, are known to be most beneficial for heat transfer enhancement in

parallel plate heat exchangers (Zhang et al. [59]). The formation and strength of these leading edge vortices will critically depend both on the existence of wake instability and also on the streamwise gap between adjacent columns. If the streamwise gap is large, the wake vortices generated in the near wake of a column of bodies may decay before they encounter the leading edge of the next column, and thus may not result in the formation of leading edge vortices.

Chapter 5

Time-Periodic Flow Regime

5.1 Introduction

As discussed in the previous chapter, the Reynolds number plays an important role in determining the characteristics of the flow in an array of bluff bodies. A steady laminar flow solution of the type described in Chapter 4 exists for these flows at all Reynolds numbers. However, above a critical value of the Reynolds number the flow becomes unstable to even infinitesimal disturbances. Above the critical Reynolds number, any disturbance introduced will grow exponentially, until the disturbance becomes large enough that non-linear interactions act to damp and ultimately halt its growth. After the introduction and growth of the disturbance the flow will exist in a state distinctly altered from its preceding steady laminar state.

For flow over a bluff body the initial laminar flow state is steady and invariant in time. After the introduction of a disturbance, the flow, when above the critical value of the Reynolds number, undergoes a bifurcation, or transition, to an unsteady time periodic laminar flow regime. Commonly this regime is characterized by the regular shedding of vortices from surfaces of the bluff body. At moderate Reynolds numbers the state of the flow is such that it may be characterized by a single frequency or period. Further increases in the Reynolds number generally result in introduction of additional higher frequencies to the flow solution and three-dimensionality. Eventually, with the increase in Reynolds number, the flow will become chaotic and characterized as turbulent.

This chapter will primarily focus on the flow in the single frequency regime, which occurs above the critical Reynolds number but before the onset of subsequent bifurcations and three dimensionality. The fully developed time-periodic flow regime for an infinite array of rectangular

bluff bodies in both the Inline and Staggered arrangements has been investigated. Particular attention is paid to the nature of the vortex shedding and its effects on the flow.

5.2 Time Periodic Flow

The basic characteristics of the flow solutions in the time periodic regimes for the Inline 1 and Staggered 2 cases are discussed within this section, with a more detailed examination of the vortex shedding phenomena presented in Sections 5.3 and 5.4. For each of these cases the flow solution has been obtained over a range of Reynolds numbers. The geometry of each case is depicted in Figure 4.1, with the parameter values given in Table 4.1. The two cases may be seen to be similar, with the exception that the Staggered 2 case has every other row of bodies offset by half of the cell length, L_x , in the horizontal direction. The two geometries, therefore, possess the same surface area to volume ratios.

To model flow through an infinite array, a periodic boundary condition of the type described in section 2.2.2 was applied to the boundaries of the computational domain indicated by dashed lines in Figure 4.1. This condition requires the introduction of the modified pressure form, shown in Equation 2.5, and the specification of the pressure drop across the domain in terms of the parameters β_x and β_y . The values of β_x and β_y were set to one and zero respectively, producing a fixed pressure drop in the stream-wise direction which drives the flow. For this value of β_x the pressure scale is then set to

$$\mathcal{P} = \frac{\Delta p^*(L_x, 0, 0, 0)}{L_x} \quad (5.1)$$

where $\Delta p^*(L_x, 0, 0, 0)$ is the dimensional pressure drop over the streamwise length of the computational domain. The velocity scale is then $\mathcal{U} = (\mathcal{P}/\rho)^{1/2}$ and the length scale, \mathcal{L} , has been set to a fraction of the domain height, L_y^* . The Reynolds number, Re , and all the non-dimensional quantities in Equation 2.1 are then defined using these scales.

The energy relation, Equation 2.14, involves a second non-dimensional parameter in addition to the Reynolds number. This parameter, the Prandtl number, (Pr) will be set to a value of 0.7, the value for air. Additionally, the energy equation requires the specification of a thermal

boundary condition on each surface in the interior of the computational domain. The use of the periodic boundary condition requires a constant heat flux boundary condition of the form shown in Equation 2.17 be applied. This condition has been applied with the heat flux q'' set to a value of one, thus setting the heat flux scale \mathcal{Q} to q'' and therefore the temperature scale, to $\mathcal{E} = q''\mathcal{L}/k$.

The basic non-dimensionalization described above does not provide the most useful form of the Reynolds number for understanding and interpreting the results. An alternative, more commonly used form is based on the hydraulic diameter, D_h^* , and mean flow velocity at the minimum cross sectional area, \bar{U}_{min}^* . This Reynolds number, Re_{D_h} , is then defined as

$$Re_{D_h} = \frac{\bar{U}_{min}^* D_h^*}{\nu} \quad (5.2)$$

and is related to the original Reynolds number by

$$Re_{D_h} = \bar{U}_{min} D_h Re \quad (5.3)$$

The dimensional (as denoted by the superscript *) hydraulic diameter and mean velocity, are defined as

$$D_h^* = \frac{4A_{min}^* L_x^*}{\Omega_f^*} \quad (5.4)$$

$$\bar{U}_{min}^* = \frac{\bar{Q}_x^*}{A_{min}^*} \quad (5.5)$$

In the above equations A_{min}^* is the effective minimum cross flow area defined as $A_{min}^* = (L_y^* - b^*)L_z^*$ for the Inline 1 case and $A_{min}^* = (L_y^* - 2b^*)L_z^*$ for the Staggered 2 case. The net surface area within the computational domain, Ω_f^* , is given by $\Omega_f^* = 2(h^* + b^*)L_z^*$, for the Inline 1 case and $\Omega_f^* = 4(h^* + b^*)L_z^*$ for the Staggered 2 and \bar{Q}_x^* is the average volumetric flow rate in the x direction. The resulting hydraulic diameter for the two geometries is the same and has the value $D_h = 4.0367$.

Local heat transfer efficiency will be measured by the Nusselt number, defined as

$$Nu(s^*, t^*) = \frac{q''^*}{k \left(\frac{T_s^*(s^*, t^*) - T_{ref}^*(s^*, t^*)}{D_h^*} \right)} \quad (5.6)$$

with T_s^* and T_{ref}^* the dimensional local surface and reference temperatures respectively. The reference temperature is defined as

$$T_{ref}^*(s^*, t^*) = \frac{\int_0^{L_z^*} \int_0^{L_y^*} T^* |u^*| dy^* dz^*}{\int_0^{L_z^*} \int_0^{L_y^*} |u^*| dy^* dz^*} \quad (5.7)$$

The absolute value is used to properly represent regions of reverse flow following Patankar and Prakask [39] and Zhang et al. [59]. Using the basic scaling and the modified form of the temperature, Equation 2.19, the above equations may be recast as

$$Nu(s, t) = \frac{D_h}{\Theta_s(s, t) - \Theta_{ref}(s, t)} \quad (5.8)$$

$$\Theta_{ref}(s, t) = \frac{\int_0^{L_z} \int_0^{L_y} \Theta |u| dy dz}{\int_0^{L_z} \int_0^{L_y} |u| dy dz} \quad (5.9)$$

From the above definition of the local Nusselt number the global Nusselt number may be defined as

$$\langle Nu(t) \rangle = \frac{\Omega_f D_h}{\int_{\Omega_f} (\Theta_s(s, t) - \Theta_{ref}(s, t)) ds} \quad (5.10)$$

Finally, the time averaged global Nusselt number, $\langle \bar{Nu} \rangle$, may be calculated by averaging the global Nusselt number over time.

The Nusselt number may be used to define a modified Colburn j factor,

$$j = \frac{\langle \bar{Nu} \rangle}{Re_{D_h} Pr^{0.4}} \quad (5.11)$$

which is a measure of the overall system performance. Along with the j factor the friction factor,

f , is defined as

$$f = \frac{\Delta p^*}{\frac{1}{2}\rho \bar{U}_{min}^2} \frac{D_h^*}{4L_x^*} = \frac{D_h}{2} \frac{1}{\bar{U}_{min}^2} \quad (5.12)$$

where Δp^* is the dimensional pressure drop across the computational domain in the streamwise direction. Finally, the definitions of the coefficient of lift, coefficient of drag, and the Strouhal number are given as follows

$$C_d = \frac{F_x}{\frac{1}{2}\bar{U}_{min}^2 b L_z} \quad (5.13)$$

$$C_l = \frac{F_y}{\frac{1}{2}\bar{U}_{min}^2 b L_z} \quad (5.14)$$

$$St = \frac{f_s b}{\bar{U}_{min}} \quad (5.15)$$

where F_x and F_y are the net force on the body in the corresponding directions and f_s is the primary vortex shedding frequency.

In order to asses the effects of the bifurcation and the resulting time periodic phenomena on the flow, the calculated time periodic flow quantities were compared to those of a laminar flow at approximately the same Reynolds number. Laminar flows solutions at supercritical Reynolds numbers were obtained by preventing the growth of the primary instability. The primary instability for these cases possesses anti-symmetry about a line passing through the center of each body and parallel to the streamwise direction. Therefore, the symmetry condition described in Section 4.2 was applied about each body, which prevented the existence of any anti-symmetric disturbance and thus the growth of the primary instability.

5.2.1 Inline Array

In this section we examine the basic characteristics of the time-periodic flow regime for the Inline 1 geometry. The results of Chapter 4 show that this flow is laminar up to a $Re_{\bar{U}_b}$ of 31.4, or to a

$Re_{\bar{U}_{min}b}$ of 57, where the velocity scales are the average flow velocity and the average flow velocity at the minimum cross sectional area respectively. Above this Reynolds number the flow becomes time periodic. Flow solutions have been obtained for several Reynolds numbers, starting in the laminar regime and continuing up to the transition to chaotic flow.

The basic nature of the flow in the time periodic regime may be examined by consideration of the flow solutions at different time instances. A vector plot of the flow solution about a single body in an infinite array is shown in Figure 5.1 at a $Re_{\bar{U}_{min}b}$ of 179. This figure shows the solution at five different time instances which are 0.23 non-dimensional time units apart. Due to the periodic nature of the flow, the first frame (a) follows the last frame (e) in a repeating sequence. The unsteady nature of the flow is readily apparent, particular in the wake region. The velocities in the wake region may be seen to have a substantial component in the transverse direction that was not present in the laminar flow solution.

The difference in the wake flow is primarily due to the generation of vortices at the trailing edge of the body. Figure 5.2 shows a plot of the swirl contours of the solution at the same time instances as Figure 5.1. Alternate generation and shedding of vortices at the upper and lower corners along the trailing edge of the body may clearly be observed. Furthermore, the alternating generation of vortices along the upper and lower surfaces at the leading edge of the body is also seen. This basic pattern of vortex shedding is observed for all of the supercritical Reynolds numbers considered. The characteristics and effects of the vortex shedding are examined in greater detail in Sections 5.3 and 5.4.

In addition to the flow solution, the temperature solution has also been obtained and is shown in Figure 5.3. Development of a thermal boundary layer along the top and bottom surfaces of the body is observed. Regions where the thermal boundary is thick, followed by regions of thin thermal boundary layer are observed along the top and bottom surfaces and are well correlated to the location of the leading edge vortices seen in Figure 5.2.

While the flow remains qualitatively similar through out the Reynolds number range considered, many aspects of it vary as the Reynolds number changes. Table 5.1 shows the variation in the various flow quantities computed at different Reynolds numbers. The variation in the Strouhal number shows the basic frequency to the vortex shedding to increase with increasing Reynolds number.

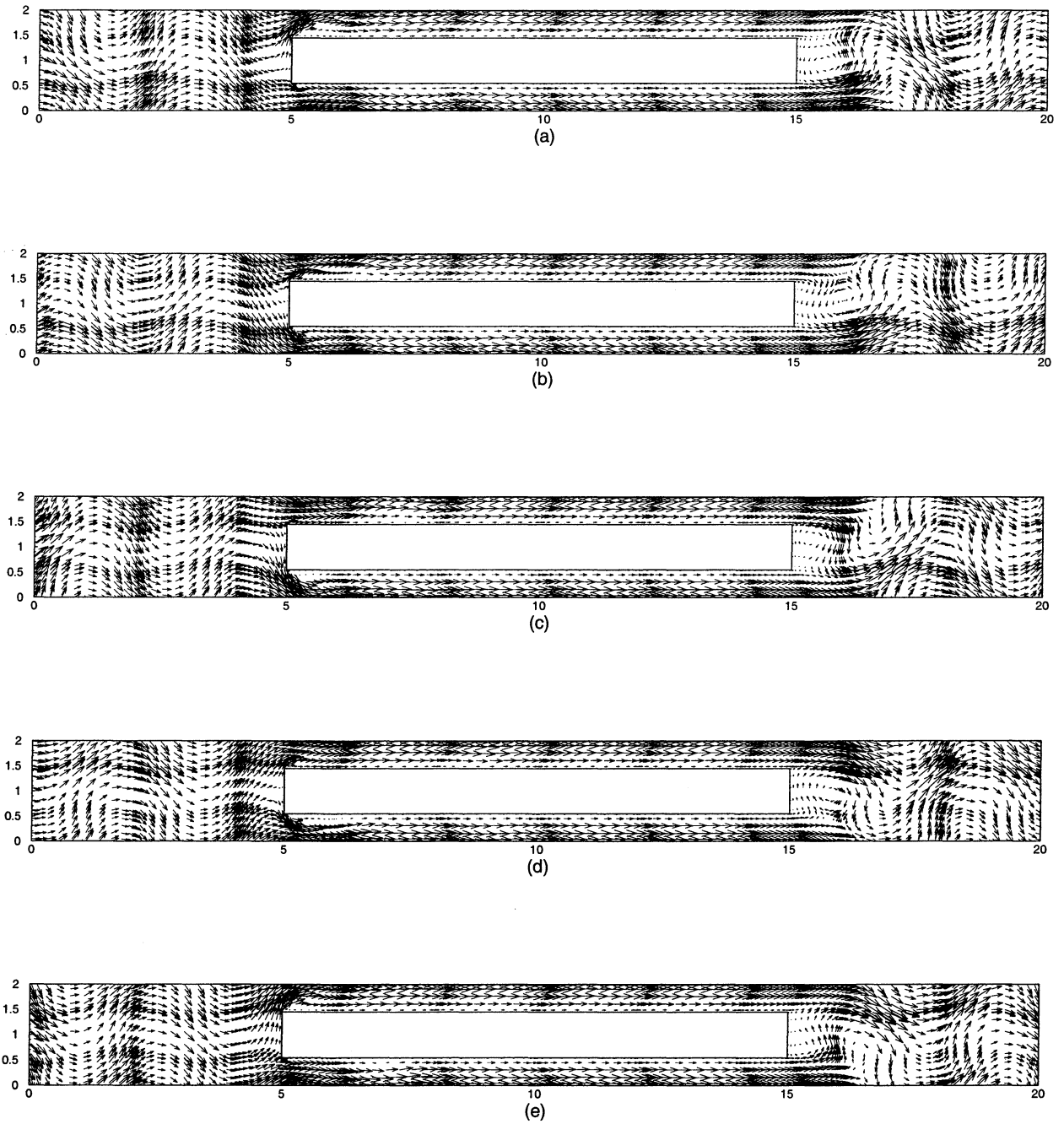


Figure 5.1: Vector plot of the flow solution for case Inline 1 at $Re_{U_b} = 179$ showing 5 time instances 0.23 time increments apart

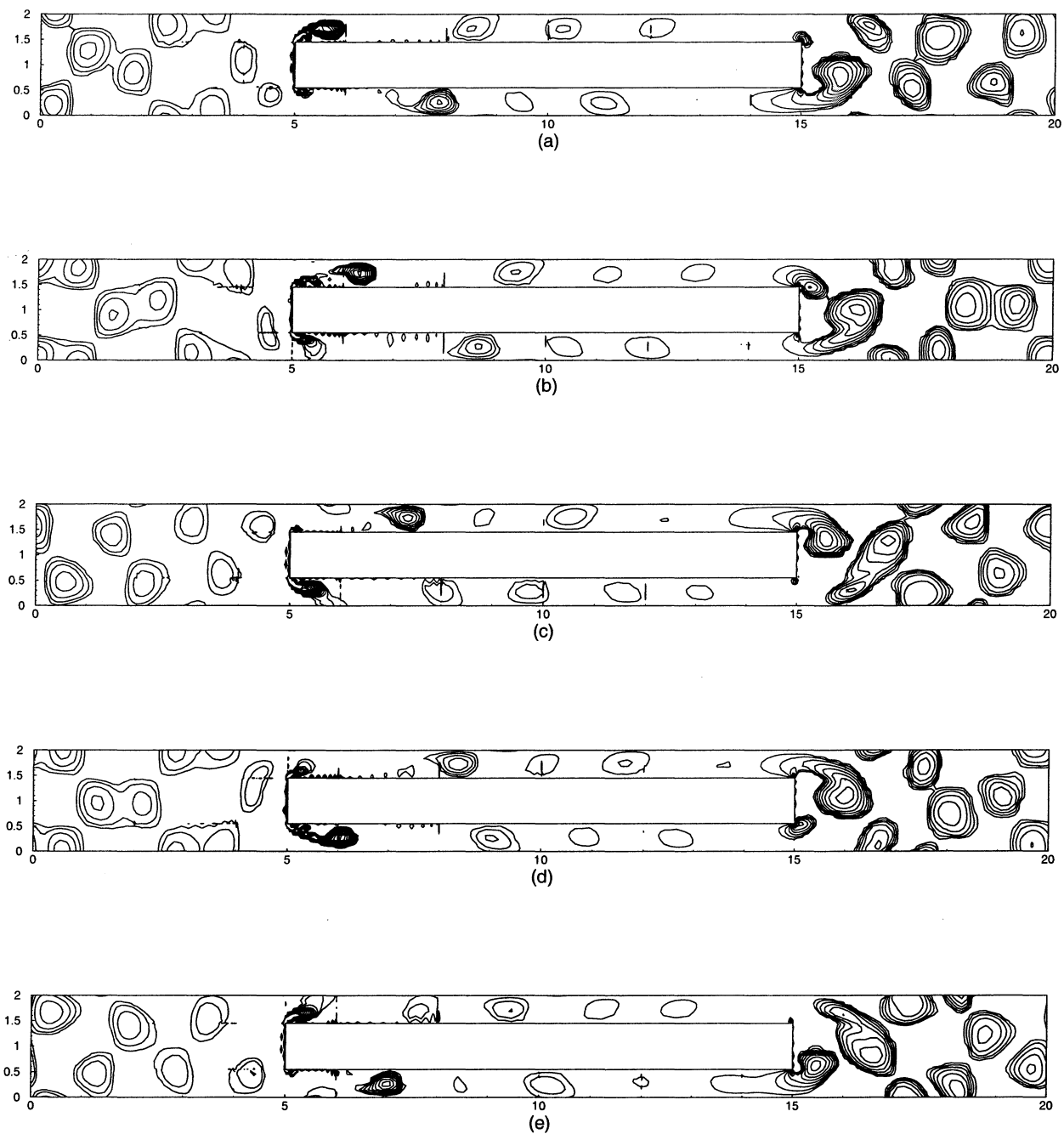


Figure 5.2: Plot of the swirl contours for case Inline 1 at $Re_{\bar{U}_b} = 179$ showing 5 time instances 0.23 time increments apart

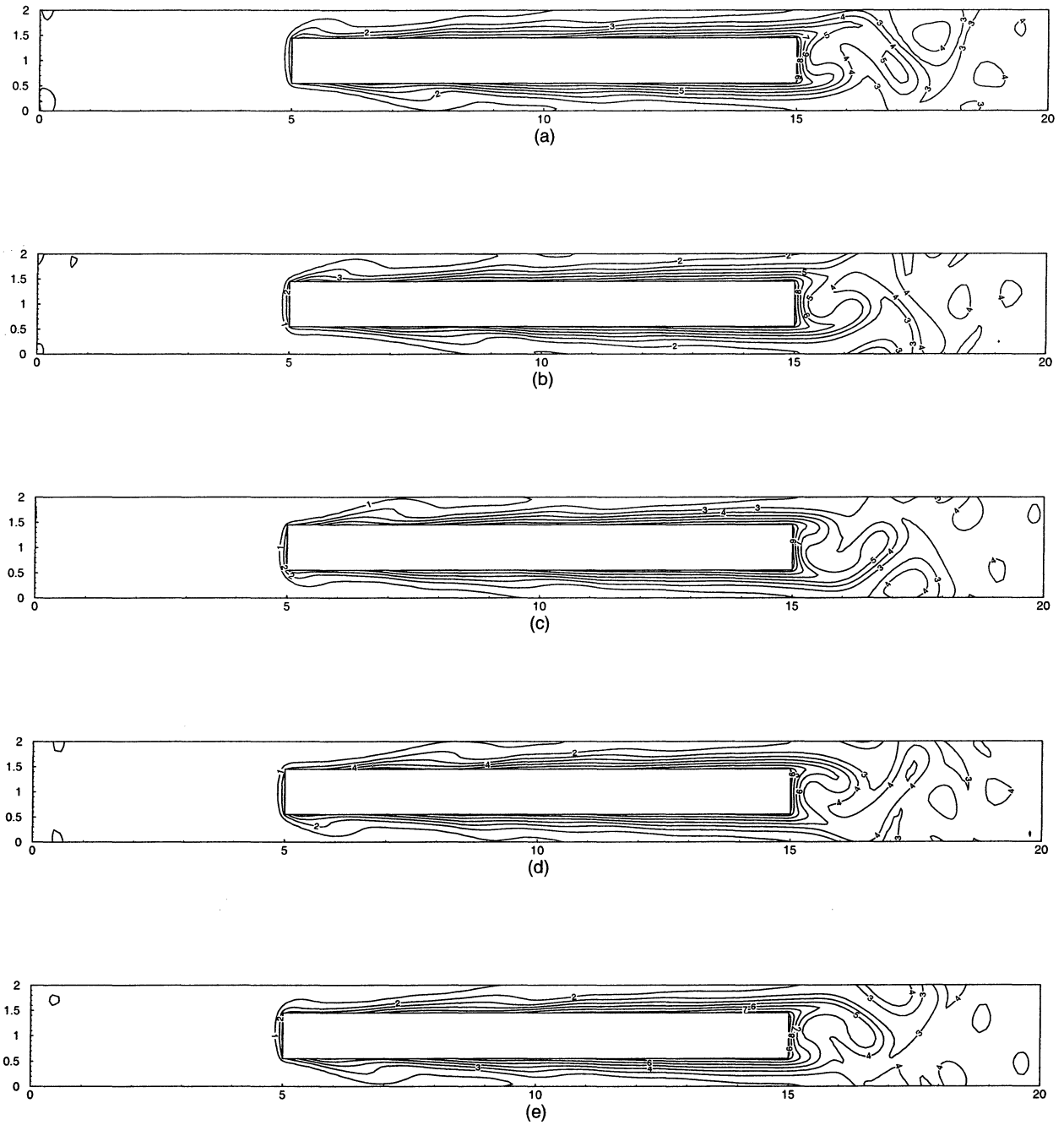


Figure 5.3: Plot of the temperature contours for case Inline 1 at $Re_{\bar{U}_b} = 179$ showing 5 time instances 0.23 time increments apart

Re	Re_{D_h}	$Re_{U_{min}b}$	\bar{C}_d	C'_l	$\langle Nu \rangle$	St	f	j
15	156	35	13.380	0.000	15.14	-	0.305	0.112
20	257	57	8.714	0.307	15.57	0.141	0.199	0.070
30	505	113	5.071	0.907	16.91	0.154	0.116	0.039
40	802	179	3.571	1.095	18.81	0.157	0.082	0.027
50	1071	239	3.121	1.375	21.56	0.158	0.072	0.023
80	1935	431	2.446	1.610	30.60	0.167	0.056	0.018

Table 5.1: Calculated values for the time varying flow of case Inline 1

Re	Re_{D_h}	$Re_{U_{min}b}$	\bar{C}_d	$\langle Nu \rangle$	f	j
20	260	58	8.549	15.53	0.195	0.069
30	523	117	4.743	16.48	0.108	0.036
40	862	192	3.096	17.44	0.071	0.023
45	1062	237	2.583	17.84	0.059	0.019
60	1784	398	1.626	19.29	0.037	0.013

Table 5.2: Calculated values for case Inline 1 with imposed symmetry

The fluctuation in the lift coefficient C'_l is associated with the strength of the shed vortices and is seen to increase as the Reynolds number increases. The variation in both these quantities may be observed by comparing Figures 5.4 and 5.5 which plot the lift coefficient for $Re_{U_{min}b}$ equal to 57 and 431. In Figure 5.4 a single frequency of oscillation may be observed while at the higher Reynolds number in Figure 5.5 more than one frequency is present. Generally the onset of higher frequency oscillation is associated with the onset of transition to chaos.

The change in quantities such as the Nusselt number with Reynolds number may be associated with both the increase in flow rate at higher Reynolds number and the effect of vortex shedding. To isolate the effect of vortex shedding, the data in Table 5.1 may be compared to the data of Table 5.2 which show the relevant quantities for supercritical laminar flow found with imposed symmetry. At Reynolds numbers close the critical value, the value of the Nusselt number may be seen to be similar for both the symmeterized and un-symmeterized cases. However, as the Reynolds number increases, the Nusselt number for the time varying flow may be seen to increase significantly over that of the laminar solution, until it is approximately fifty percent higher at a $Re_{\bar{U}_{min}b}$ of around 400. A comparison of the friction factor f between the time periodic and laminar flows is shown in Figure 5.6. An increase in the friction factor and therefore pressure drop may be seen to be produced by vortex shedding. The figure also shows the increased heat transfer, as measured by

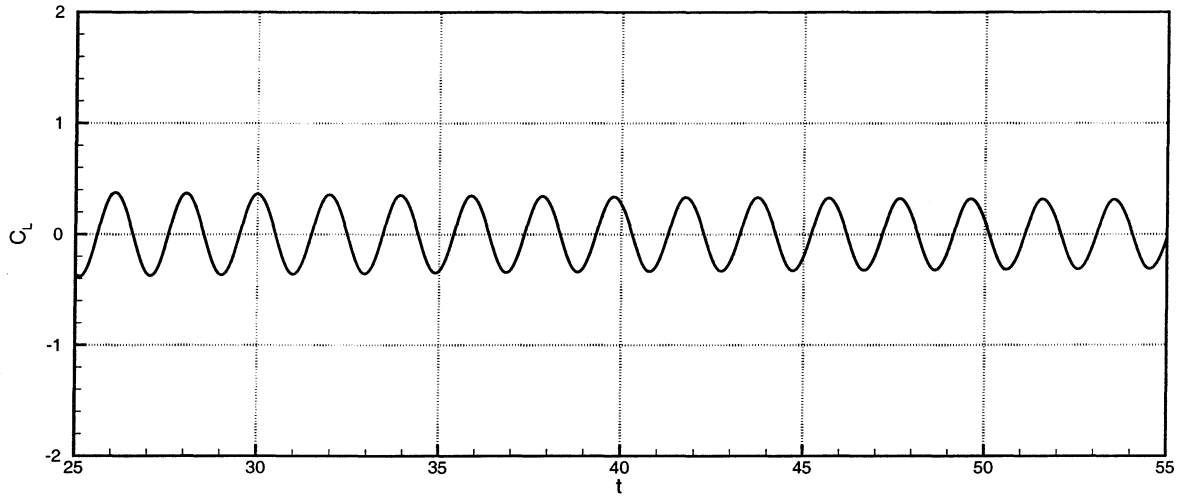


Figure 5.4: Plot of the Coefficient of Lift for Inline 1 at $Re_{\bar{U}_b} = 57$

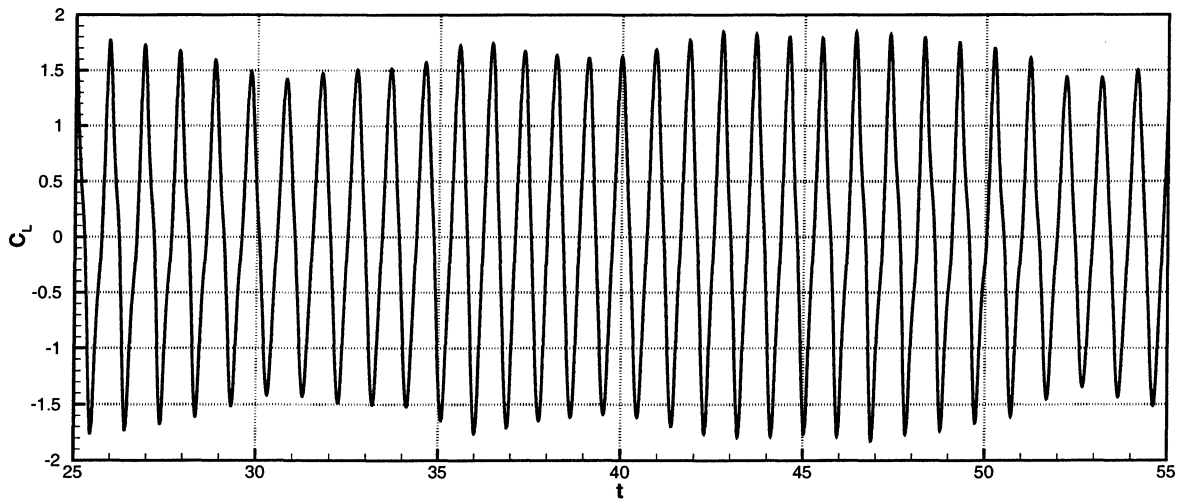


Figure 5.5: Plot of the Coefficient of Lift for Inline 1 at $Re_{\bar{U}_b} = 431$

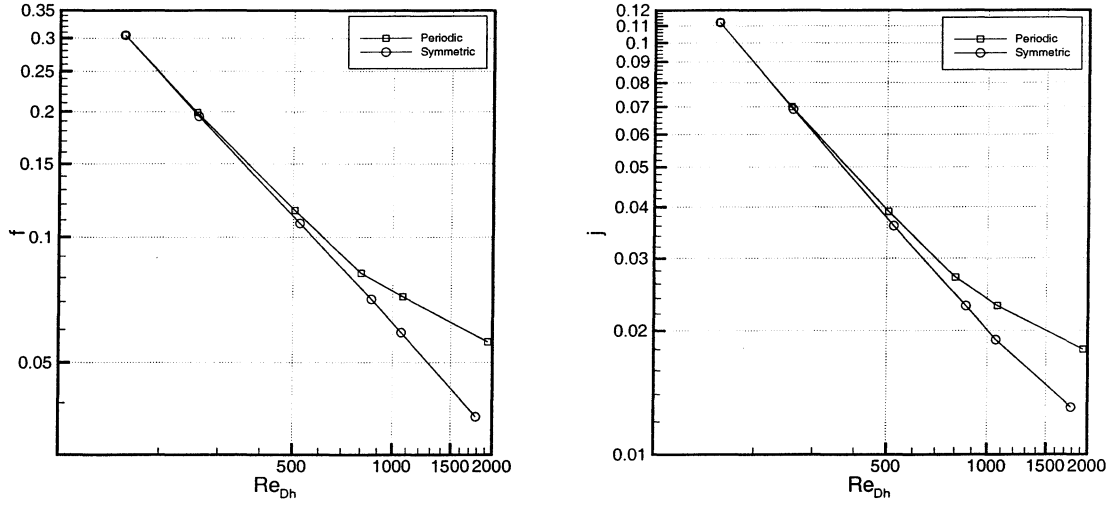


Figure 5.6: f and j factors as a function of Reynolds number for the Inline 1 case

the j factor, also attributable to vortex shedding.

5.2.2 Staggered Array

In many respects the flow in the Staggered 2 array is similar to that seen in the Inline 1 array. The same transition from laminar, to time varying, to chaotic state is observed. However, the Reynolds numbers at which these transitions occur are very different. The results of Chapter 4 show that for the Staggered 2 geometry the transition from laminar to time varying flow occurs at a $Re_{\bar{U}_{minb}}$ of 111. Thus the transition occurs at a significantly higher Reynolds number than for the Inline case which became unstable at a $Re_{\bar{U}_{minb}}$ 57.

Despite the later transition, the general nature of the time varying flow for the Staggered 2 geometry remains similar to what is observed for the Inline 1 case. Figure 5.7 shows a series of vector plots of the flow solution for $Re_{\bar{U}_{minb}}$ equal to 142. Shown are two rectangular bodies composing a periodic cell of an infinite array. The plots shown are at an increment of 0.12 non-dimensional time units apart, and due to the periodic nature of the flow the sequence of plots repeats, with the first plot following the last. Waviness in the solution is again observed in the wake region to be caused by vortices shed from the trailing edge of bodies, which may be seen clearly in Figure 5.8, where the contours of swirl at the same time instances as Figure 5.7 are

Re	Re_{D_h}	$Re_{\bar{U}_{min}b}$	\bar{C}_d	\bar{C}'_l	$\langle \bar{Nu} \rangle$	St	f	j
15	312	70	3.30	0.000	9.97	-	0.076	0.037
21	514	115	2.38	0.130	10.90	0.24	0.055	0.024
25	637	142	2.20	0.212	11.75	0.25	0.051	0.021
30	781	174	2.12	0.695	13.08	0.26	0.049	0.019
40	1020	227	2.17	1.392	16.67	0.27	0.052	0.019

Table 5.3: Calculated values for time varying flow of case Staggered 2

Re	Re_{D_h}	$Re_{\bar{U}_{min}b}$	\bar{C}_d	$\langle \bar{Nu} \rangle$	f	j
21	526	117	2.27	10.66	0.052	0.023
25	689	154	1.88	10.86	0.043	0.018
28	819	183	1.66	10.86	0.038	0.015
33	1014	226	1.50	13.60	0.035	0.016

Table 5.4: Calculated values for case Staggered 2 with imposed symmetry

plotted. The presence of vortices shed at the leading edge of the bodies may also be noted. The effect of these leading edge vortices may be seen in the temperature solution shown in Figure 5.9, where the vortices cause local thinning of the thermal boundary layer on the bodies.

The flow remains qualitatively similar throughout the Reynolds number range considered. However, quantitative values such as the pressure drop and heat transfer see significant variation. The variation in these and other quantities with Reynolds number is shown in Table 5.3. From these data it may be seen that the Nusselt number increases steadily over the range of Reynolds numbers considered. The f and j factors initially decrease with Reynolds number but at the highest Reynolds number the f factor begins to slightly increase while the j factor levels off. At the highest Reynolds number the flow has become chaotic as seen in the plot of lift coefficient fluctuation shown in Figure 5.11. This may be contrasted with the plot at the lower Reynolds number of $Re_{\bar{U}_{min}b} = 115$ in Figure 5.10 where the flow is periodic with a single frequency. For the Staggered 2 case the onset of the chaotic flow state occurs at a $Re_{\bar{U}_{min}b}$ between 174 and 227, while for the Inline 1 case the transition to a chaotic state occurs at a Reynolds number above 431, the highest value for which calculations were performed.

The trends in the f and j factors are shown in Figure 5.12 which shows these quantities plotted as a function of the Reynolds number based on the hydraulic diameter. Also plotted are the data from Table 5.4 which show the results for the Staggered 2 case with imposed symmetry. The effect of vortex shedding may be seen to increase both the pressure drop and heat transfer efficiency. It

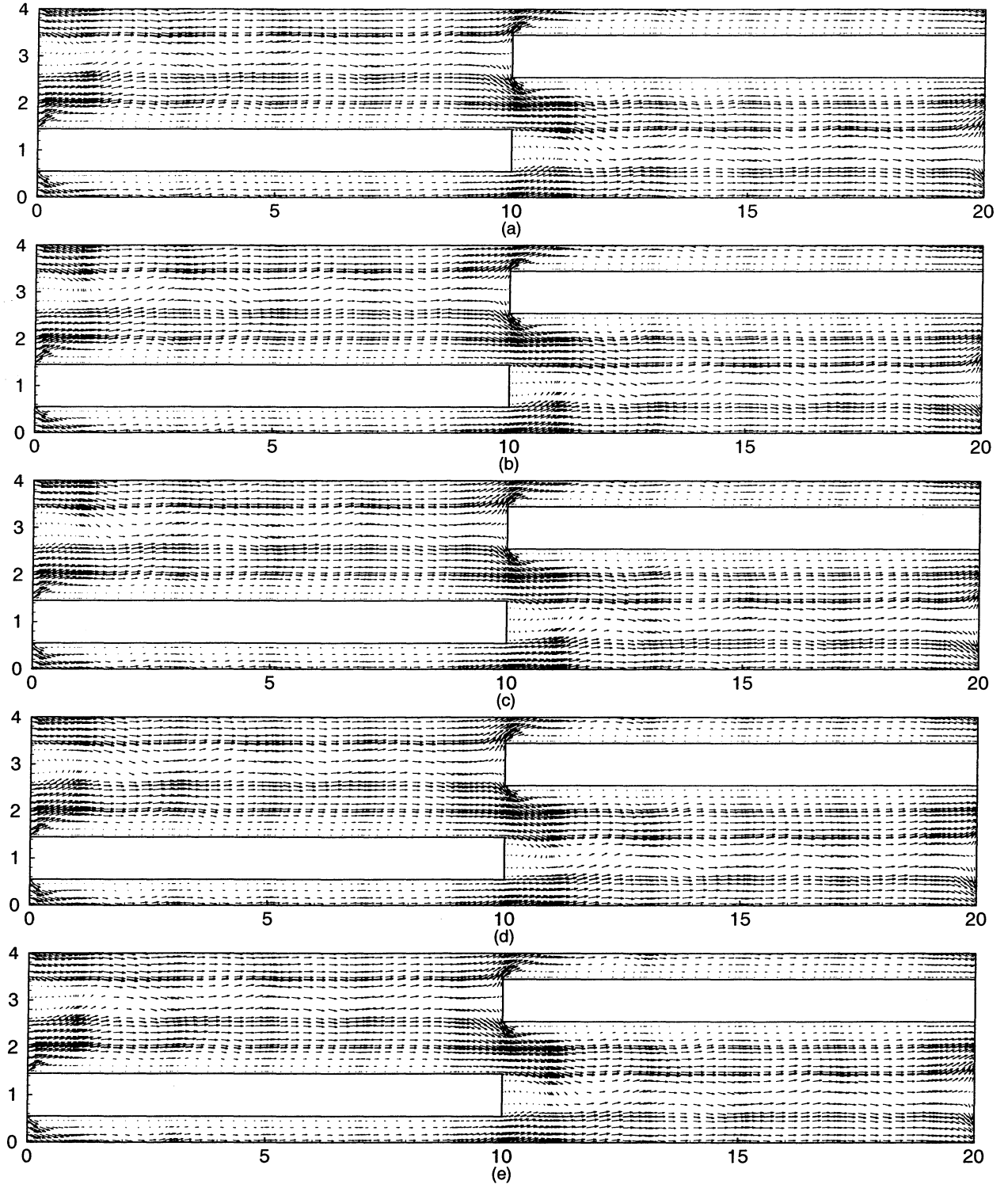


Figure 5.7: Vector plot of the flow solution for case Staggered 2 at $Re_{\bar{U}_b} = 142$ showing 5 time instances 0.12 time increments apart

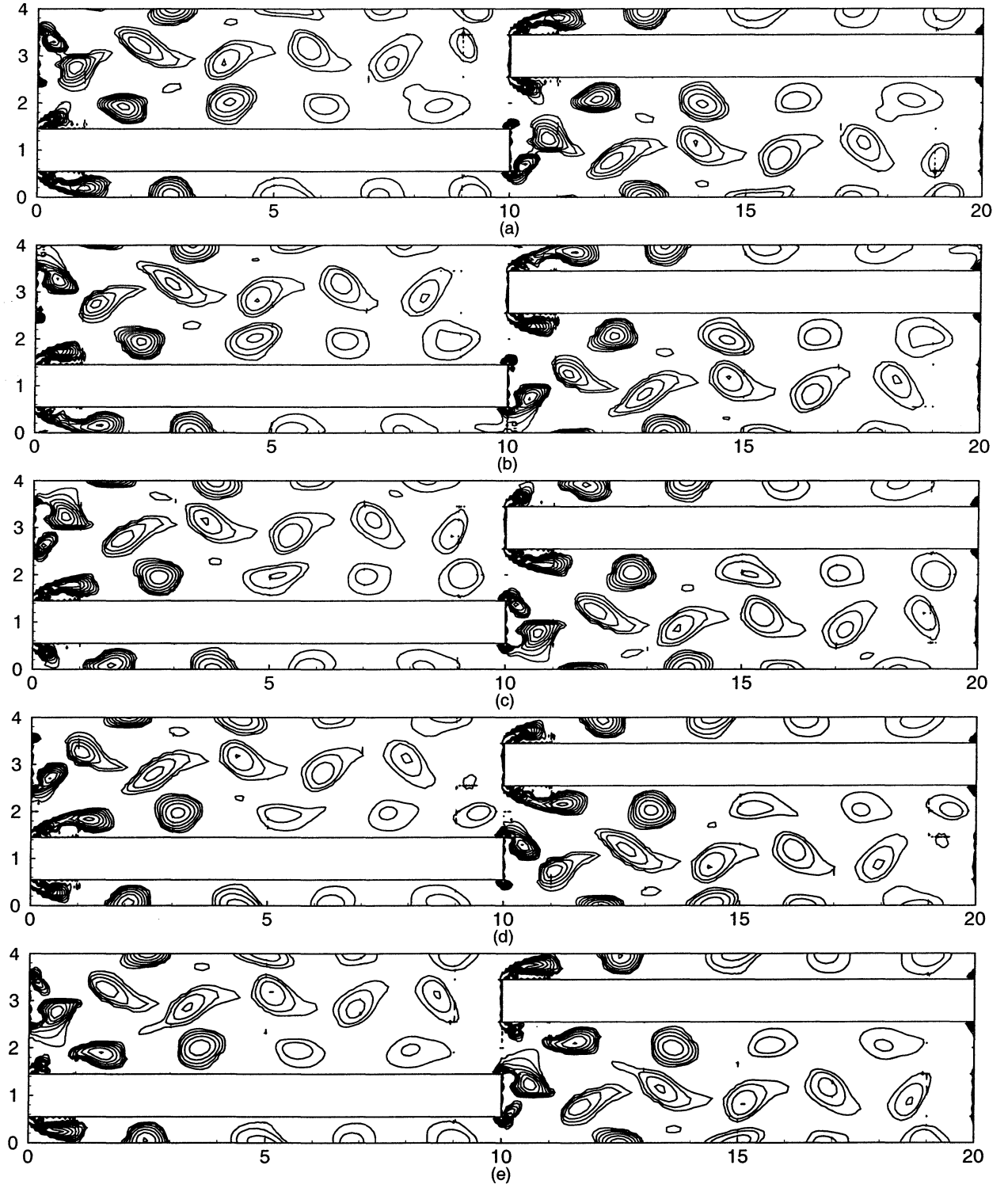


Figure 5.8: Plot of the swirl contours for case Staggered 2 at $Re_{\bar{U}b} = 142$ showing 5 time instances 0.12 time increments apart

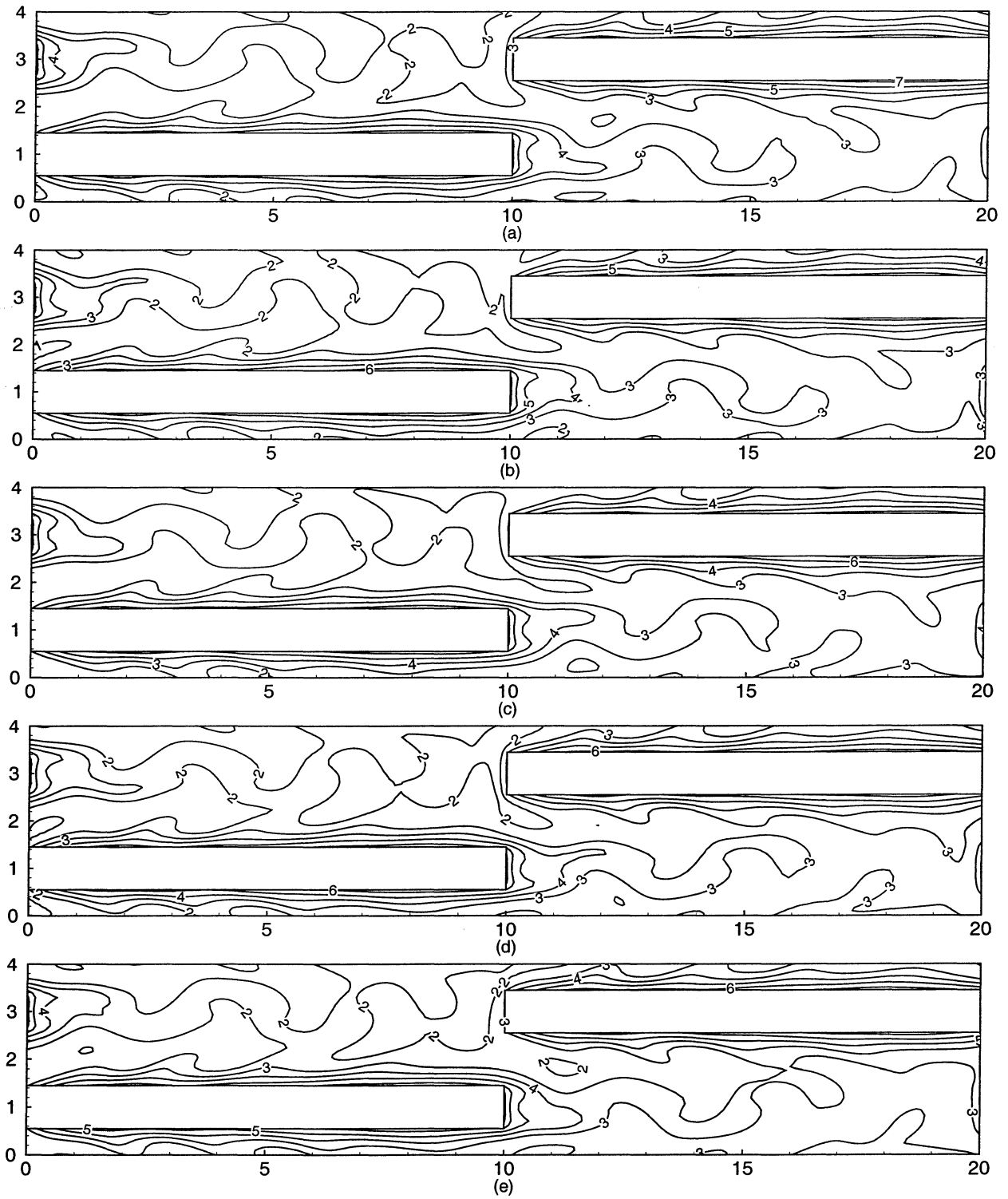


Figure 5.9: Plot of the temperature contours for case Staggered 2 at $Re_{\bar{U}_b} = 142$ showing 5 time instances 0.12 time increments apart

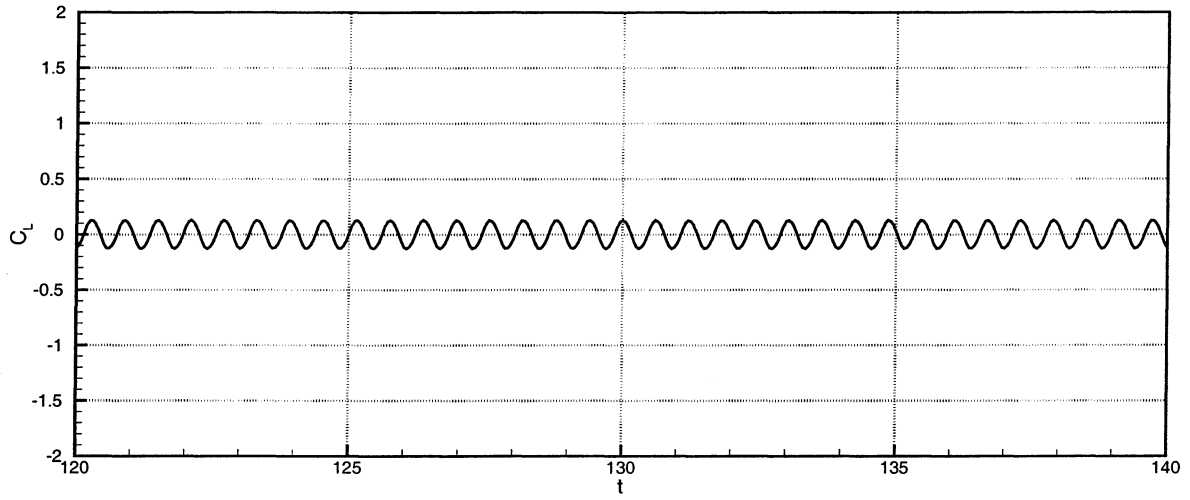


Figure 5.10: Plot of the Coefficient of Lift for Staggered 2 at $Re_{\bar{U}b} = 115$

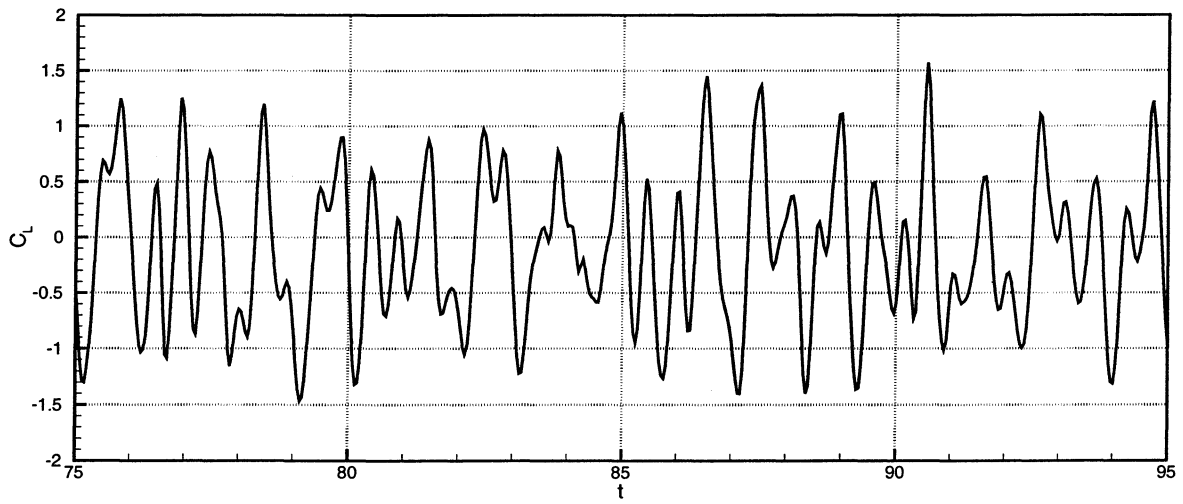


Figure 5.11: Plot of the Coefficient of Lift for Staggered 2 at $Re_{\bar{U}b} = 227$

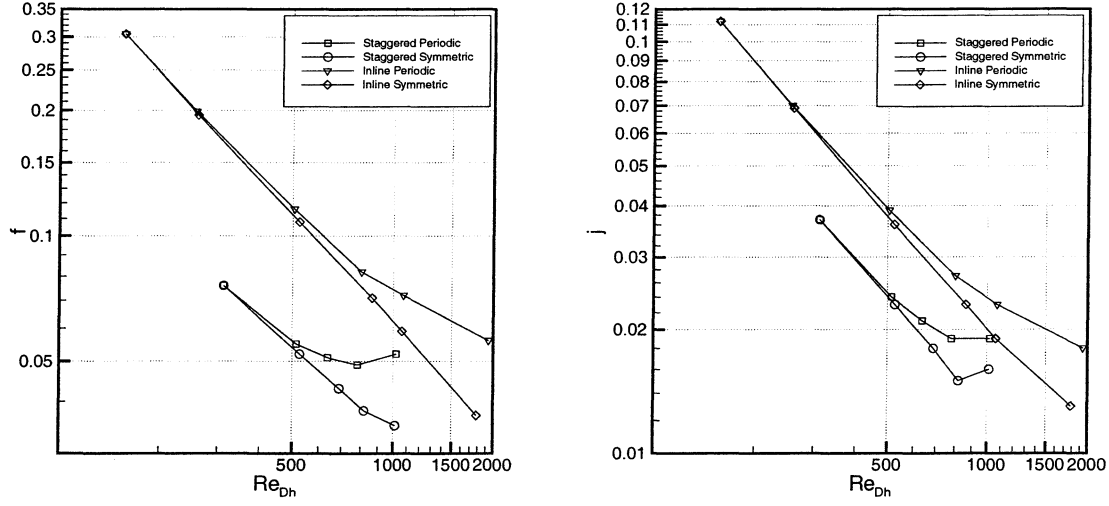


Figure 5.12: f and j as a function of Reynolds number for the Inline 1 and Staggered 2 case

should be noted that the symmetric case at the highest Reynolds number, $Re_{\bar{U}_{min}b} = 226$, exhibited weak symmetric vortex shedding from the leading edge which causes the upturn in the symmetric j factor curve. Figure 5.12 also shows the results of the Inline 1 case for comparison purposes. At low Reynolds numbers the Inline 1 case exhibits significantly higher values of f and j than the Staggered 2 case. However, this difference is greatly reduced at the higher Reynolds numbers. The difference in these values is largely attributable to the differing effective transverse spacing between bodies (Zhang et al. [59]), which for the Inline 1 case is 1.1 and for the Staggered 2 case is 3.1 .

5.3 Leading Edge Vortex Shedding

Vortex shedding has long been a phenomenon associated with flow around bluff bodies. In the canonical geometry of a circular cylinder a train of vortices is observed to be shed from alternating sides of the body. This phenomenon is also observed for flow over a square cylinder, as seen in the Square XY Non-Periodic case shown in Figure 3.9 where the Karman vortex street, composed of vortices shed alternately from the upper and lower surfaces of the body, may be observed.

In the case of rectangular bodies of larger aspect ratio, wake vortices are also observed to shed from the trailing edge of the body. Furthermore, at Reynolds numbers significantly higher than that required to produce shedding at the trailing edge, additional vortices may be shed from the

leading edge. In the two array geometries investigated, Inline 1 and Staggered 2, a body of aspect ratio, h/b , equal to 11.11 has been employed. An additional case, Rectangular XY Non-periodic, having only a single body of the same aspect ratio exposed to a uniform oncoming stream has also been considered. The parameters for this case are given in Table 4.1. From the stability analysis of Chapter 4 it was determined that the Rectangular XY Non-periodic flow becomes unstable and begins shedding vortices at a $Re_{\bar{U}b}$ of 111.6. A plot of the swirl contours for this case is shown in Figure 5.13 for the $Re_{\bar{U}b}$ of 200, 250, and 300. For all three Reynolds numbers, shedding of vortices from the trailing edge of the object is observed. At a $Re_{\bar{U}b}$ of 200, stationary recirculation regions are observed at the leading-edge of the body, but no vortices are observed to be shed. At a higher Reynolds number of 250 an asymmetry may be observed in the leading edge recirculation regions, which indicates either weak or impending leading edge vortex shedding. At a Reynolds number of 300, clear shedding of vortices from the leading edge may be seen. These vortices shed alternately from the upper and lower surfaces and travel along the body until merging into the vortices shed from the trailing edge. Thus for this flow two distinct bifurcations occur, the first at a $Re_{\bar{U}b}$ of 111.6 which is associated with the shedding of vortices from the trailing edge of the body and the second at a $Re_{\bar{U}b}$ of approximately 250 associated with the shedding of vortices from the leading edge.

For the Inline 1 and Staggered 2 geometries leading-edge vortex shedding of the type shown in Figures 5.2 and 5.8 is observed for all Reynolds numbers above the critical value. Thus no secondary bifurcation is observed which produces the vortex shedding at the leading edge, instead the onset of leading edge shedding occurs simultaneously with the onset of shedding at the trailing edge. The simultaneous onset of leading and trailing edge vortex shedding, however, is not observed for the Rectangular X Non-Periodic case, defined in Table 4.1, which consists of a single column of the Inline 1 array exposed to a uniform oncoming stream. Figure 5.14 shows three bodies in the column and depicts the vortices produced at a $Re_{\bar{U}b}$ of 77. Vortex shedding in the wake may be clearly observed while no shedding from the leading edge is seen. The simultaneous onset of leading and trailing edge vortex shedding present for the full arrays Inline 1 and Staggered 2, but absent in the Rectangular X and XY Non-Periodic cases, where the oncoming flow is uniform, indicates that the presence of upstream bodies, and most likely the vortices shed in their wake, is instrumental in

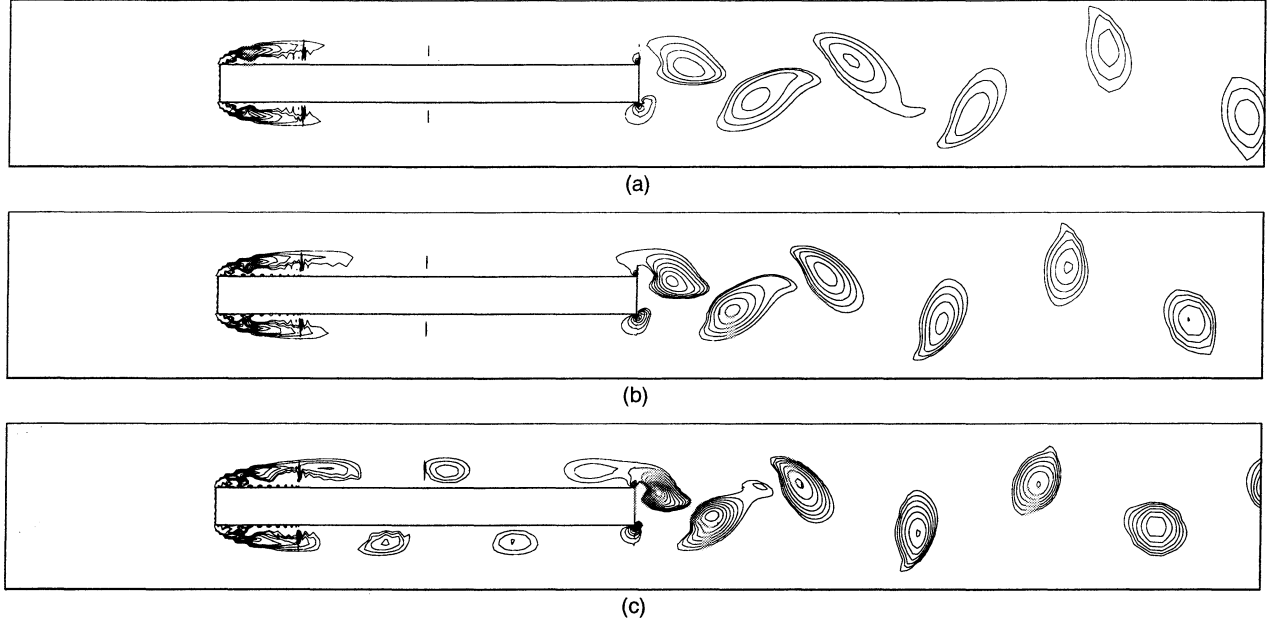


Figure 5.13: Swirl contours for case Rectangular XY Non-Periodic showing vortex shedding from a single rectangular body in a uniform oncoming stream at three different $Re_{\bar{U}_b}$ (a) 200 (b) 250 (c) 300

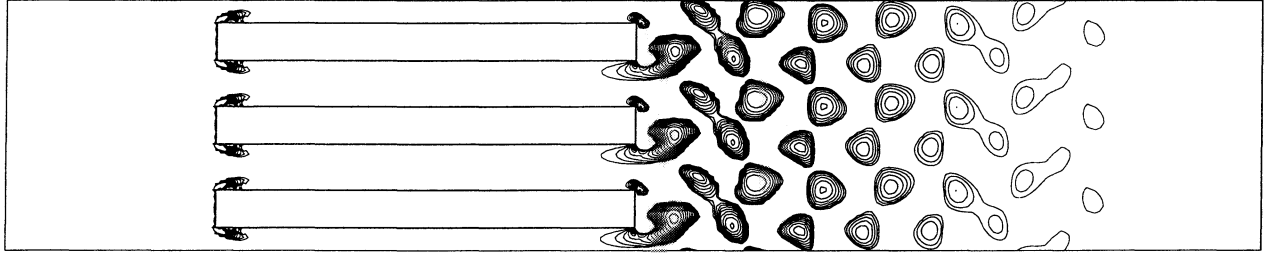


Figure 5.14: Swirl contours for the case Rectangular X Non-Periodic at $Re_{\bar{U}_b} = 77$

triggering the simultaneous onset of leading and trailing edge shedding.

The presence and relative intensity of the leading edge vortices may be quantified using the calculated values of the swirl. The swirl values, $S'(x, y, t)$ calculated for each instantaneous flow solution may be averaged over a shedding cycle to yield the time averaged swirl, $S'(x, y)$. Integrating the two dimensional time averaged swirl in the y direction and scaling by the average streamwise velocity at the minimum cross sectional area, \bar{U}_{min} , produces a measure of the swirl or vortex intensity variation in x , $S(x)$. Figures 5.15 and 5.16 plot this value along the length of a body for the Inline 1 and Staggered 2 cases respectively. For the Inline 1 case the y integration was performed across the entire gap, c in Figure 4.1(a), between bodies. For the Staggered 2 case the

y integration of the swirl was performed over the first 1.1 non-dimensional units of the gap c on either side of the body, the same as the gap length for the Inline 1 case, in order to capture only the leading edge vortices and not the trailing edge vortices shed from the upstream body, which from Figure 5.8 may be observed to remain largely confined to the region directly behind the body.

Figure 5.15 shows the variation in swirl intensity along the body for the Inline 1 case, with regular solutions results shown in part (a) and the results for solutions with imposed symmetry shown in part (b). High swirl intensities may be observed at the leading and trailing edges of the body, this is primarily due to extremely high swirl values very close to the corners of the body where the sharp change in flow direction has a singularity like effect on the calculated swirl. In addition, small peaks in the swirl may be observed at intervals along the body where sub-domains meet. This is a consequence of the multi-domain discretization and of no physical significance. The line for $Re_{\bar{U}_{minb}}$ equal to 35 in 5.15(a) shows the swirl intensity for a sub-critical laminar flow, where no vortices are shed. The results for all of the super-critical laminar flows with imposed symmetry, which also exhibit no vortex shedding, shown in 5.15(b) are seen to be nearly identical. For the non-symmetric, supercritical flows shown in 5.15(a) a steady increase in swirl intensity occurs with increasing Reynolds number, corresponding to stronger leading edge vortex strength. The swirl intensity may also be observed to decrease along the length of the body, as the vortices shown in Figure 5.2 weaken as they travel down the body.

Swirl intensity variation along a body in the Staggered 2 arrangement is shown in Figure 5.16. Again 5.16(a) shows the intensity for the flows without symmetry while 5.16(b) intensity for flow with symmetry imposed. The line for $Re_{\bar{U}_{minb}}$ equal to 70 shows the swirl for a sub-critical laminar flow with no vortex shedding. The swirl intensity for the symmetric cases may be seen to be similar, except for $Re_{\bar{U}_{minb}}$ equal to 226 where symmetric leading edge shedding occurs. For the laminar flows the swirl exhibits the same large values at the edges of the body as seen in the inline case. Additional peaks in the swirl are observed inward of both edges and are due to the sharp turns in the flow produced by the staggered arrangement. The swirl intensities of the non-symmetric solutions increase with Reynolds number, indicating stronger leading edge vortex shedding. The values are also generally higher than those of the Inline case.

The shedding of vortices from the leading edge of the body can have a pronounced affect upon

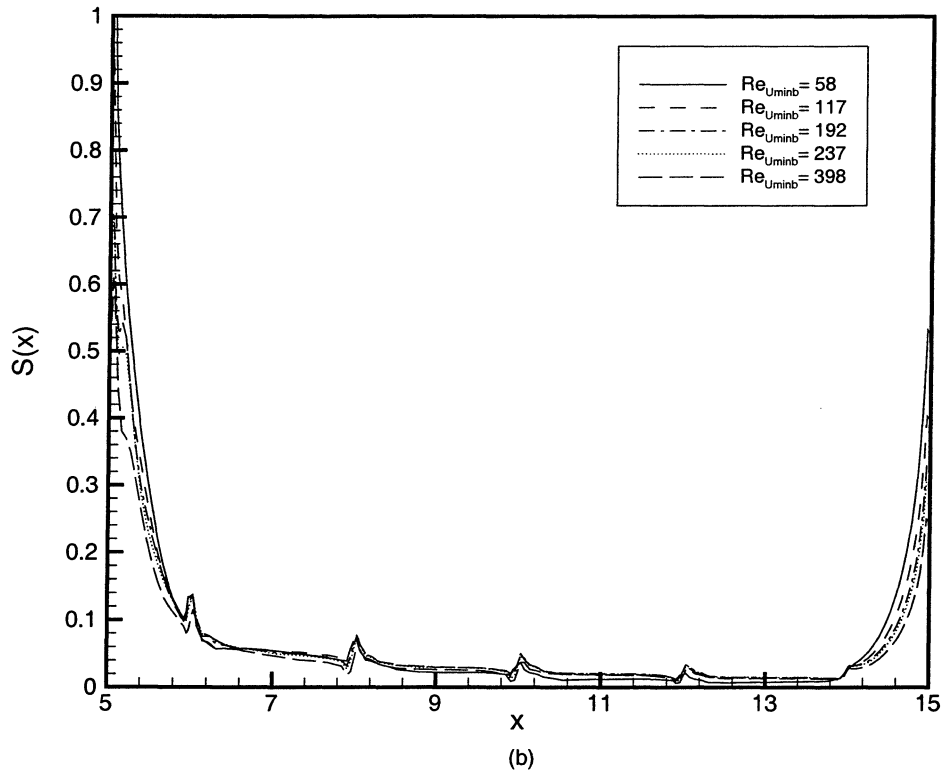
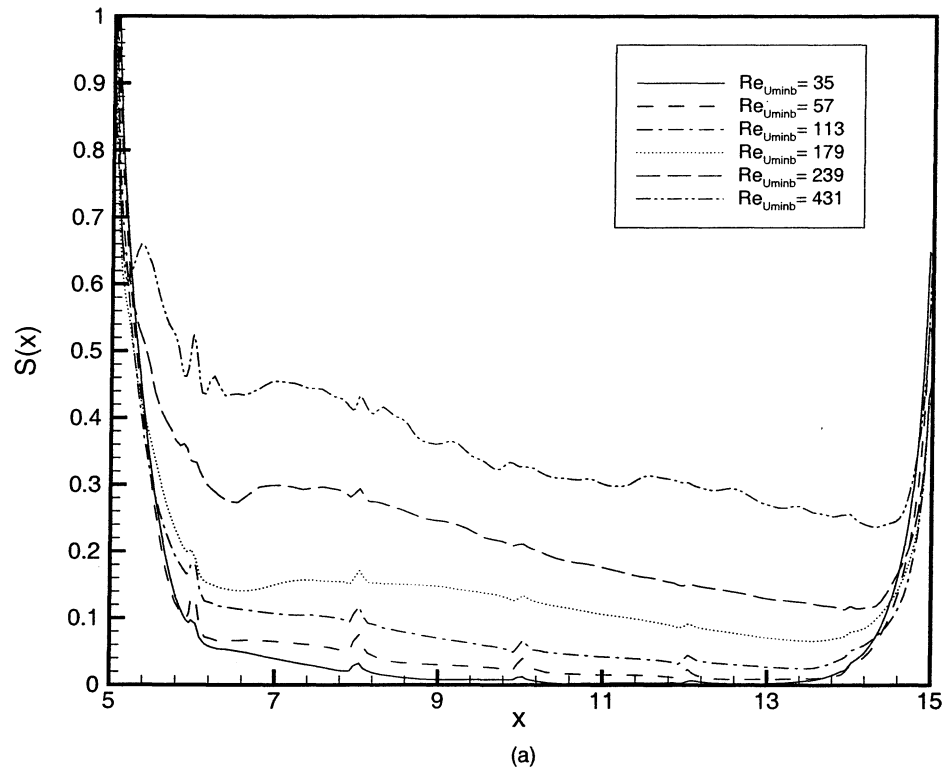


Figure 5.15: Integrated time averaged swirl intensity for the case Inline 1, (a) regular solutions, (b) solutions with imposed symmetry

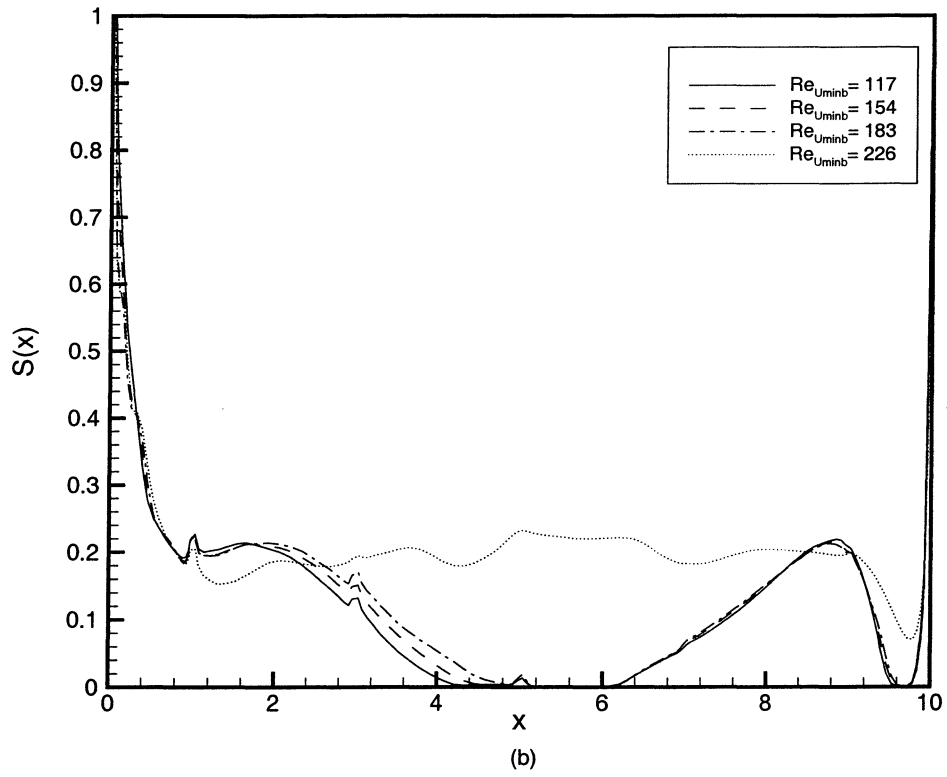
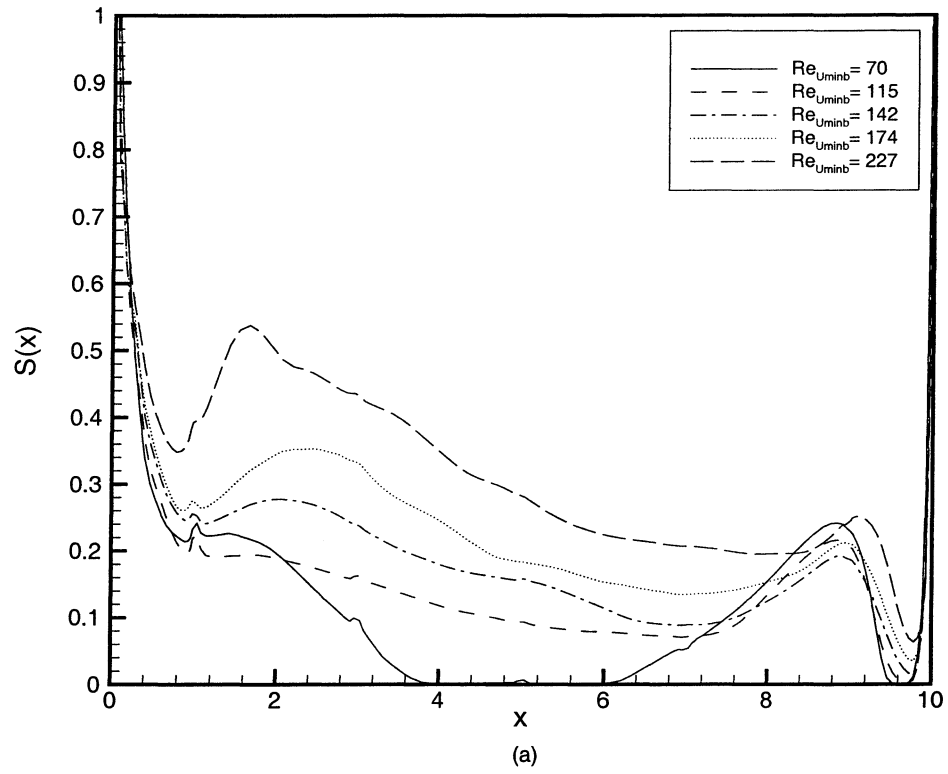


Figure 5.16: Integrated time averaged swirl intensity for the case Staggered 2, (a) regular solutions, (b) solutions with imposed symmetry

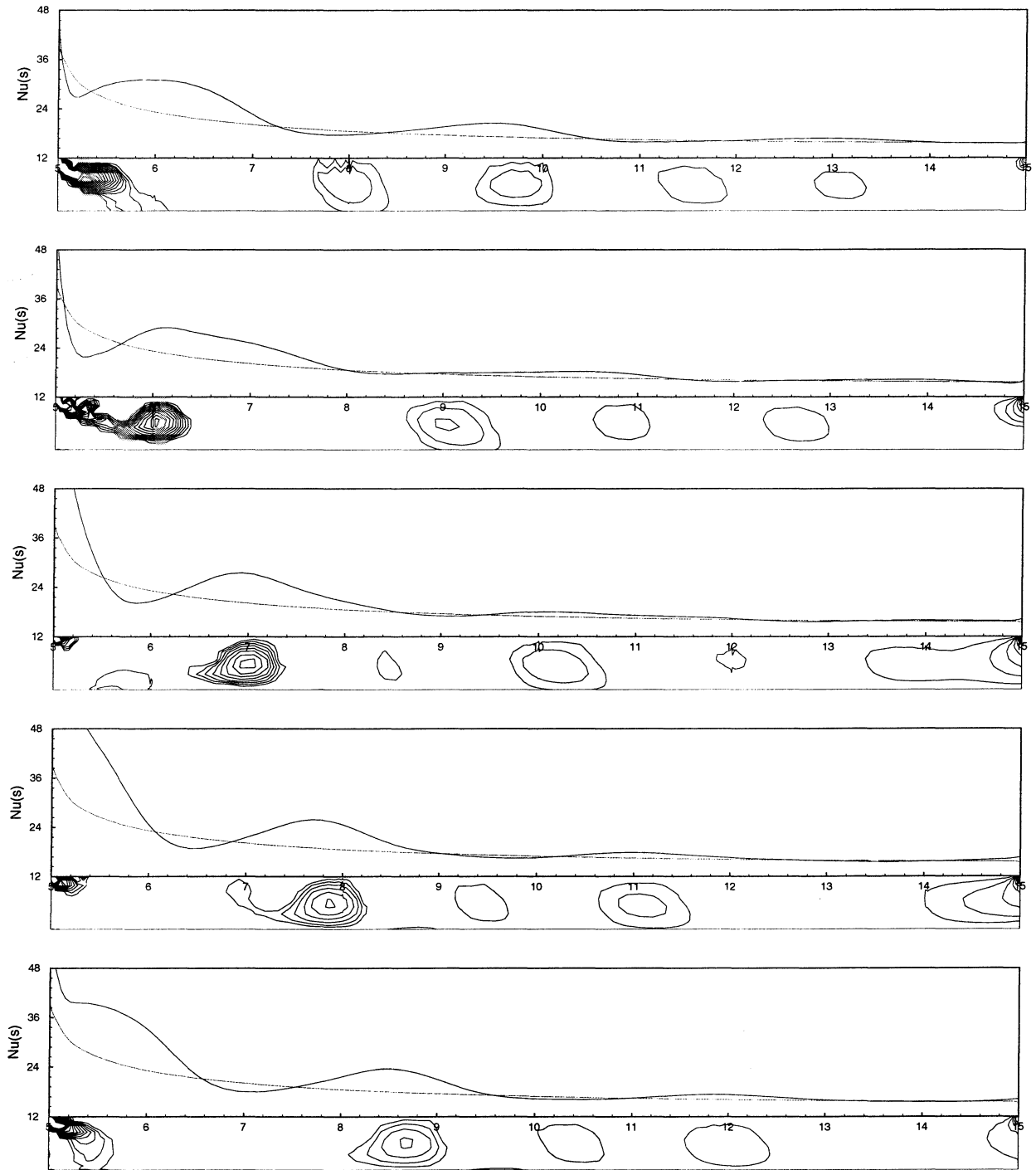


Figure 5.17: Leading edge vortex shedding and local Nusselt number along the lower surface of the body of the Inline 1 case at $Re_{\bar{U}_b} = 179$ and 0.23 time increments apart

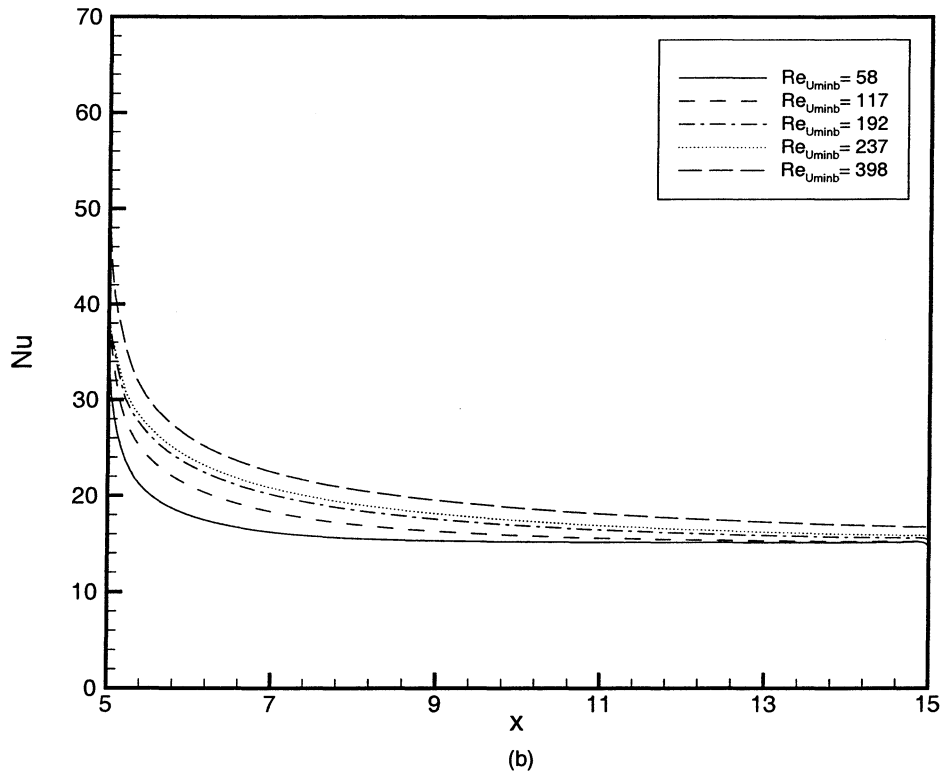
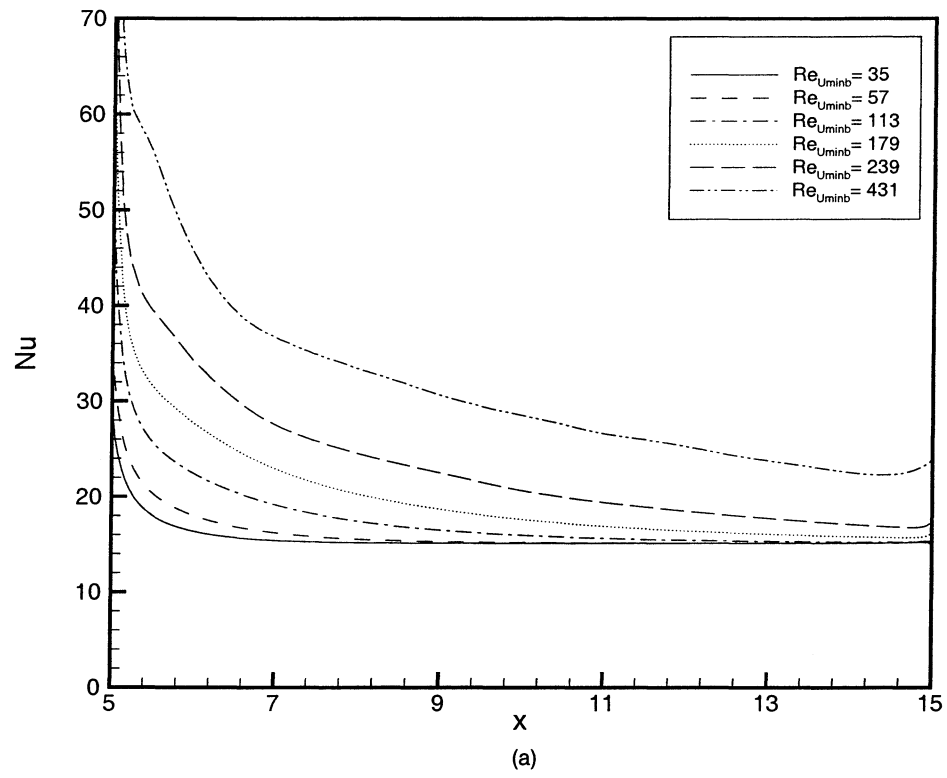


Figure 5.18: Time averaged local Nusselt number for the case Inline 1 (a) Periodic flow results (b) Symmetric flow results

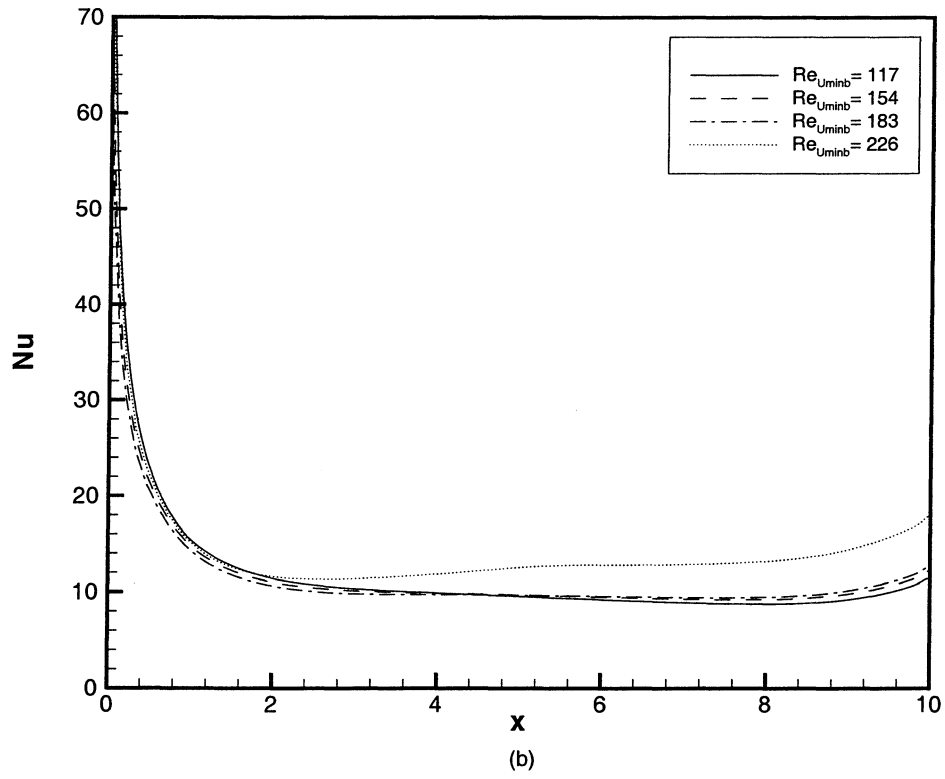
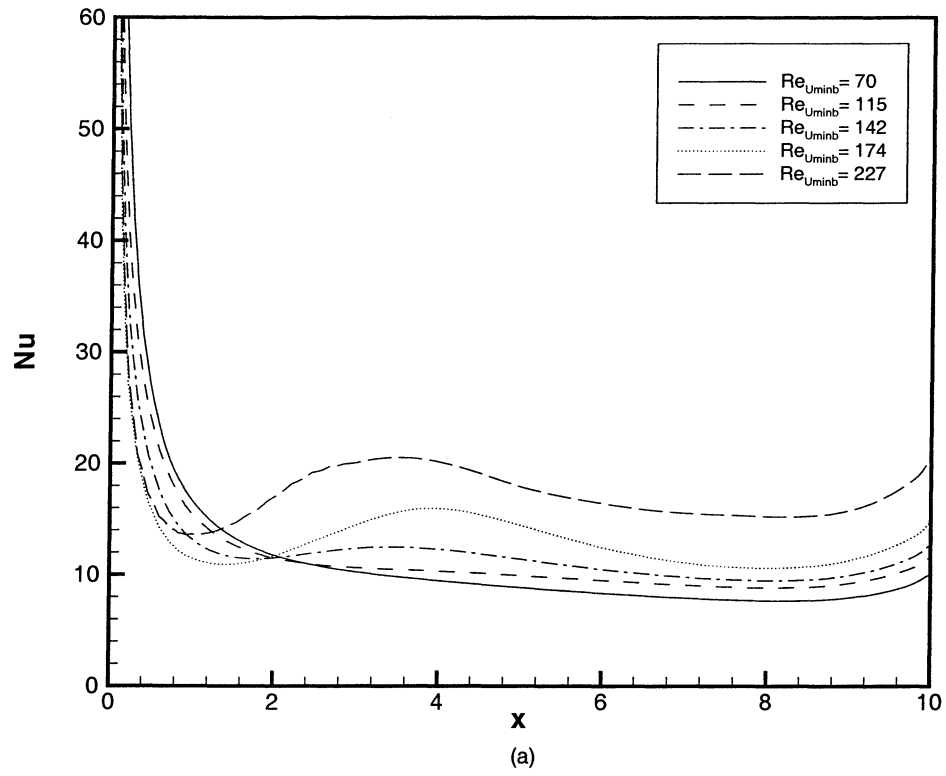


Figure 5.19: Time averaged local Nusselt number for the case Staggered 2 (a) Periodic flow results (b) Symmetric flow results

the rate of heat transfer from a body. The heat transfer results in Tables 5.1 - 5.4 show that the periodic flows with vortex shedding see an up to fifty percent increase in global Nusselt number over a symmetric laminar flow at the same Reynolds number. Figure 5.17 shows how the vortices shed from the leading edge effect the local, and thereby global, heat transfer from the body. The figure depicts the vortices shed along the lower surface of the body in the Inline 1 array at a $Re_{\bar{U}_{minb}}$ of 179 in a repeating sequence of five time instances 0.23 time increments apart. Also shown is the local Nusselt number and the local Nusselt number for a laminar flow at the same Reynolds number. The vortices may be seen to be associated with an increase in the local Nusselt number over that of the laminar flow. This is a consequence of the rotary motion of the vortex, which sweeps cooler fluid into the surface and ejects the warmer surface fluid, thus increasing local the mixing. The net effect of the vortices on the local Nusselt number can be seen in Figure 5.18 for the Inline 1 array and Figure 5.19 for the Staggered 2 array. The figures show the average local Nusselt number along the top or bottom surfaces of a body in the array for the regular flow solutions and those with symmetry imposed. The average local Nusselt number increases proportionately to the increase in swirl intensity.

5.4 Trailing Edge Vortex Shedding

Vortex shedding from the trailing edge of a body is a well known and much observed phenomenon. Numerous studies have investigated this type of shedding for the canonical geometries of circular or square cylinders. Shedding from these types of bodies takes the form of vortices shed from alternating surfaces and convecting downstream behind the object to form the well known Karman vortex street. An example of this for a square cylinder in a uniform flow is shown in Figure 3.9 where the Karman vortex street may be readily observed. Similar behavior at the trailing edge is observed for an isolated rectangular body of the same dimensions as those used in the Inline 1 and Staggered 2 arrays when exposed to a uniform oncoming stream. This may be seen in Figure 5.13 which shows the vortices shed from the body in the Rectangular XY Non-Periodic case.

The behavior of vortices shed at the trailing edge of a body in the Staggered 2 arrangement is very similar to what is seen for an isolated body. This may be observed in Figure 5.8 which shows the vortices shed in the Staggered 2 array at $Re_{\bar{U}_{minb}}$ equal to 142. The wake vortices may

be observed to shed from alternating sides of the body and travel downstream directly behind the object. The same basic behavior is present at all Reynolds numbers where shedding occurs. However, at the higher Reynolds numbers some chaotic interaction between the leading and trailing edge vortices occurs.

For the Inline 1 case, the behavior of the vortices shed from the trailing edge has been found to be very different from that described above. As a consequence of the stacking of the bodies, in the form of columns of the array, the trailing edge vortices shed from neighboring bodies interact. This vortex interaction causes the vortices to split and then form into counter rotating pairs which propagate at an angle to the mean flow direction. This behavior is shown in Figure 5.20, which shows eight bodies in an infinite array for a flow with a $Re_{\bar{U}_{min}b}$ of 179. The instances shown are 0.23 time increments apart and form a repeating cycle due to the periodicity of the flow. The time instances shown are the same as those shown in Figure 5.2. Starting in the first frame a vortex shed from the lower surface of a body is highlighted with dashed lines, while in the third frame a vortex shed from the upper surfaces is highlighted in grey. The motion of the highlighted vortices may be followed by tracking the vortex from frame to frame. In the first frame the dashed lower surface vortex is beginning to shed. By the third frame it is detached from the body. In the fourth frame the vortex may be seen to have been split by interaction with neighboring vortices, producing two separate vortices which propagate in differing directions. The upper of the two split vortices propagates upward at an angle to the free stream, while the lower propagates downward at an angle. The complete progress of the vortices may be followed by returning to the first frame after viewing the fifth and repeating. The vortex shed from the upper surface, highlighted in grey, may be seen to behave in a similar manner. Note also the the split vortices propagate upward and downward in pairs composed of one of the split vortices from the upper surface and one from the lower surface. This formation of counter rotating vortex pairs allows the vortices to impel themselves at an angle to the mean fluid motion which is in the x direction.

This behavior is observed in the Inline 1 case for all Reynolds numbers at which vortex shedding occurs. Furthermore, it has been observed for all of the Inline cases listed in Table 4.1, and additionally for the Rectangular X Non-Periodic case which consists of a single column of bodies exposed to a uniform flow. Therefore this behavior is a consequence of the vertical stacking of

bodies with close enough proximity to allow interaction of the vortices shed from the trailing edge. Some variation in the vortex trajectories is observed for the Inline 1 case at different Reynolds numbers. Trajectories of the vortices are shown for $Re_{\bar{U}_{min}b}$ 57 and 431 in Figure 5.21. At a $Re_{\bar{U}_{min}b}$ 57 the vortex splitting does not occur until around $x = 21$, at which point the vortices pair and begin to propagate at a small angle to the free stream. For the higher Reynolds number cases the vortex splitting occurs very close to trailing edge, as seen for the plot of $Re_{\bar{U}_{min}b}$ equal to 431 where the vortices split at around $x = 16$. As the Reynolds number increases the propagation angle also increases. The swirl intensity of the vortices also increases with Reynolds number, which may be what allows the vortices to move at a larger propagation angle.

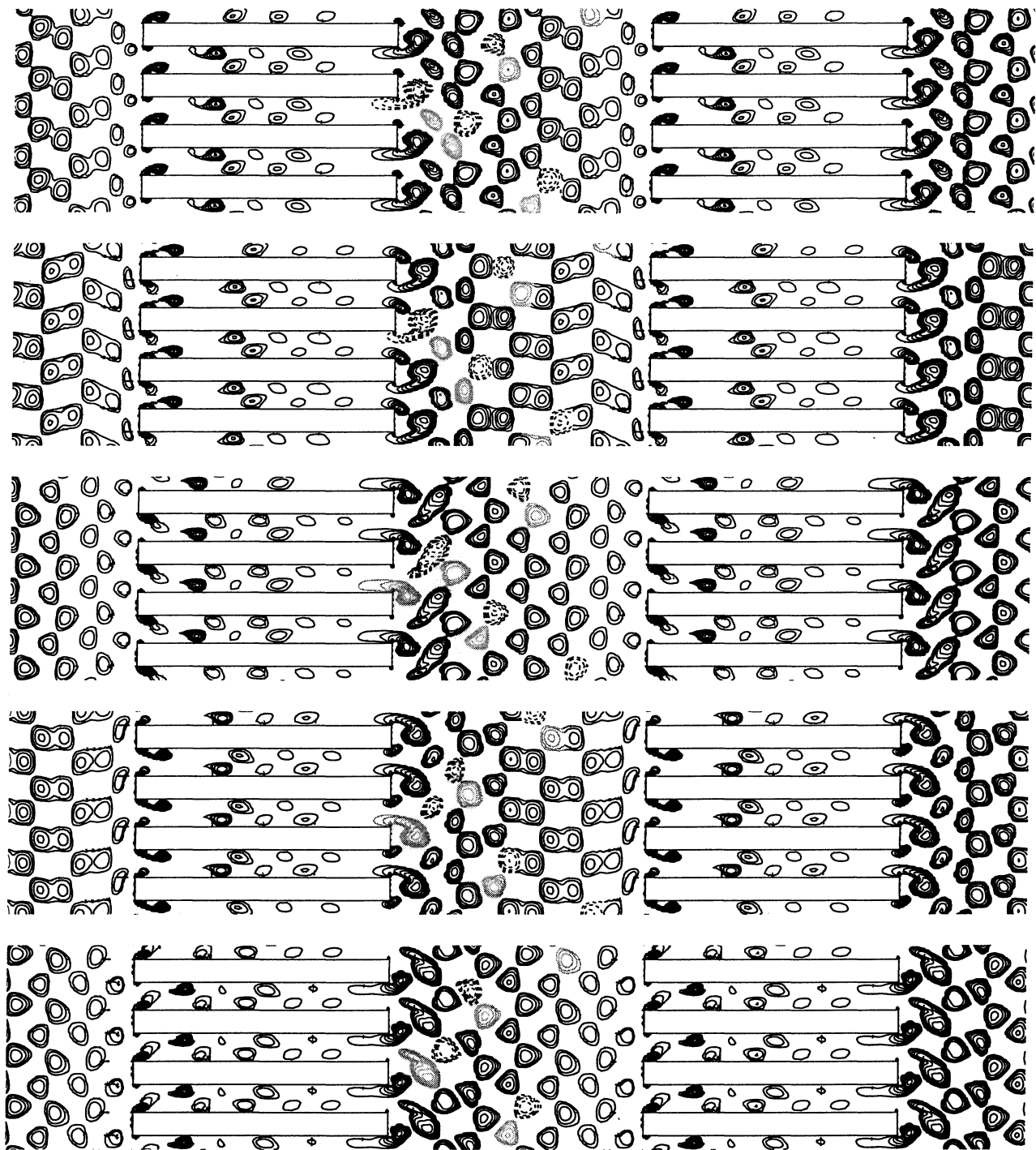


Figure 5.20: Swirl contours around eight element of the infinite Inline 1 array at five time instances 0.23 time units apart at $Re_{\bar{U}_b} = 179$

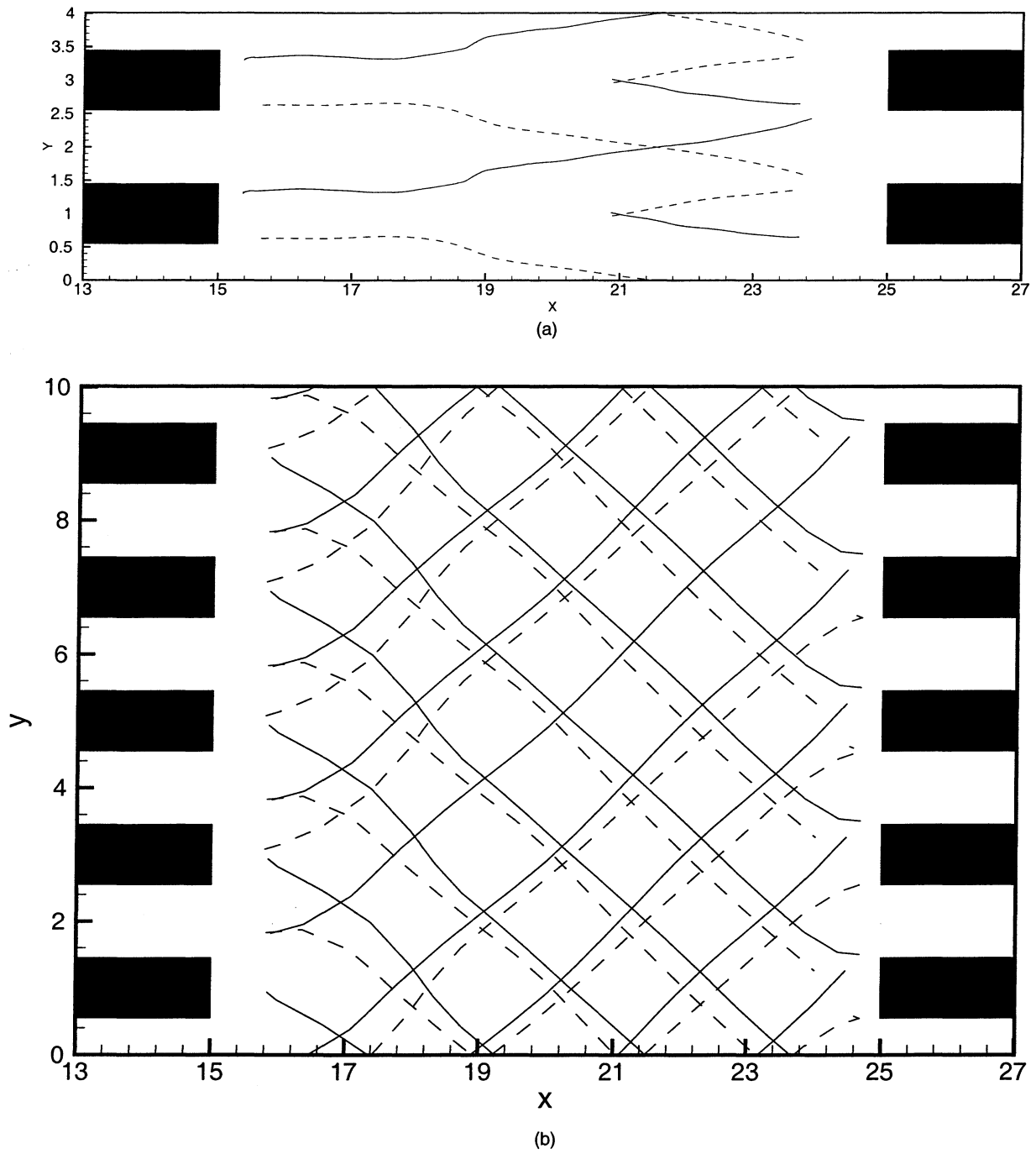


Figure 5.21: Vortex trajectories for the Inline 1 case at $Re_{\bar{U}_b}$ of (a) 57 and (b) 431. Solid lines plot the paths of vortices shed from the upper surface of the body and dashed lines for the lower.

Chapter 6

Intermediate Offset Array

6.1 Introduction

In this chapter a final flow geometry related to the earlier Inline 1 and Staggered 2 geometries is considered. The Inline 1 and Staggered 2 arrays are similar in all respects, except in the offset between successive rows of fins. For the Inline 1 arrangement each successive row is aligned with the rows adjacent to it, while for the Staggered 2 geometry every other row is offset by a fin length in the streamwise direction. We now consider a third arrangement wherein the same bodies and spacing as the Inline 1 and Staggered 2 cases are employed but each row is offset half a fin length in the streamwise direction from the one below it. This arrangement is shown in Figure 6.1(a). In terms of the row offsets this case is an intermediate case between the Inline and Staggered arrangements.

This intermediate arrangement shares some similarities with a common heat exchanger geometry, the louvered fin array. In a louvered fin array the fins are oriented at an angle to the oncoming

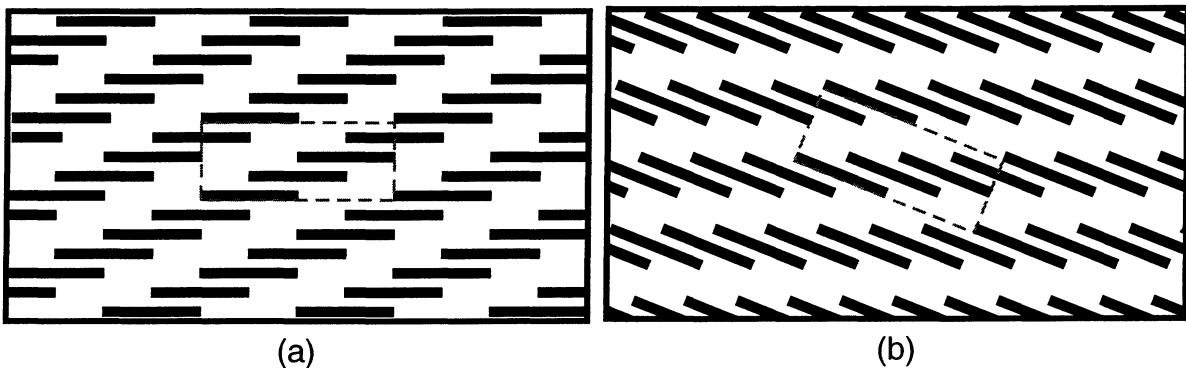


Figure 6.1: Intermediate offset geometry and the corresponding louver array

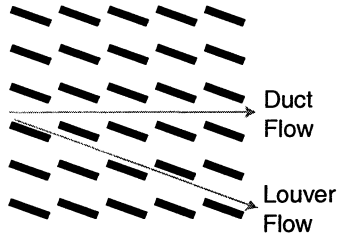


Figure 6.2: Duct and Louver flow

flow or driving pressure gradient. Such an array is shown in Figures 6.2, where the mean flow direction would nominally be from left to right. An alternate view of the Intermediate Offset array is shown in Figure 6.1(b) which is simply the geometry of Figure 6.1(a) rotated as a whole 21.8 degrees. The differences between the louver array model shown in Figure 6.2 and the intermediate offset arrangement shown in Figure 6.1(a) are the angle of orientation of the bodies relative to the direction of the oncoming flow or driving pressure gradient and the length of the channel region between bodies. For the intermediate offset array the bodies are aligned parallel to the driving pressure gradient, while in the louver geometry the bodies are at an angle of 21.8 degrees to the pressure gradient. The intermediate offset array also has a channel region between bodies equal to half the length of the fin, whereas a louvered array has none.

Early research into the flow through louvered arrays by Beauvais [4] and Davenport [10] has shown that under many conditions the flow becomes aligned with the louver direction and not with the direction of the driving pressure gradient. These observations were also later confirmed by Achaichia and Cowell [2] [1]. The phenomenon of louver directed flow was found to be Reynolds number dependent, with the flow direction being aligned with the driving pressure gradient at low Reynolds numbers, referred to as duct flow, and aligned with the louver direction at higher Reynolds numbers, referred to as louver flow. These two types of flow are depicted in Figure 6.2. This Reynolds number dependence was attributed to the viscous flow resistance occurring in the louver gap, which is high at low Reynolds numbers and low at high Reynolds numbers. Higher Reynolds numbers allow more flow between the louver gap, aligning the flow direction with the angle of the fins.

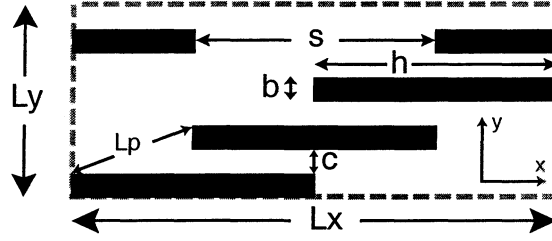


Figure 6.3: Periodic cell and geometric parameters for the Intermediate Offset geometry

Case	b	h	s	c	Lx	Ly	Lp	X Bnd.	Y Bnd.
Louver	0.90	10.00	10.00	1.10	20.0	8.0	5.39	Per.	Per.

Table 6.1: Tabulated geometric parameters for the Intermediate Offset geometry

6.2 Definitions

To solve for the flow through an intermediate offset array of infinite extent, periodic boundary conditions are again applied to a basic periodic cell, indicated in Figure 6.1 by the dashed lines and shown again in Figure 6.3. The parameters for this geometry are listed in Table 6.1. As discussed above, the body dimensions, streamwise spacing between bodies, and transverse spacing between rows are the same as those of the Inline 1 and Staggered 2 cases, which are listed in Table 4.1. As a consequence of the half fin length offset between rows the basic periodic cell now includes four fins and extends eight non-dimensional units in the y direction.

The application of periodic boundary conditions again requires the modified form of the Navier-Stokes momentum equation, Equation 2.7, be solved. This is done with the values of β_x and β_y set equal to one and zero respectively. The base non-dimensionalization used for the intermediate offset case remains the same as that used for Inline 1 and Staggered 2, and is described in Section 5.2. The temperature solution is determined by solving the energy equation, Equation 2.14, with the same constant heat flux boundary conditions.

While the geometry currently under consideration is similar to that of the Inline 1 and Staggered 2 geometries, it will prove useful to alter slightly some of the definition applied to those cases, as well as define some additional quantities. The mean velocity defined in Equation 5.5, is redefined

to allow for a net velocity in the y direction, and becomes

$$\bar{U}_{min} = \left[\left(\frac{\bar{Q}_x}{A_{min,x}} \right)^2 + \left(\frac{\bar{Q}_y}{A_{min,y}} \right)^2 \right]^{\frac{1}{2}} \quad (6.1)$$

where \bar{Q}_x and \bar{Q}_y are the net volumetric flow rate through the domain in the x and y directions respectively, and the effective minimum cross flow areas are defined as

$$A_{min,x} = (L_y - 4b)L_z \quad (6.2)$$

$$A_{min,y} = (L_x - h)L_z \quad (6.3)$$

The hydraulic diameter is defined as

$$D_h = \frac{4A_{min,x}L_x}{\Omega_f} \quad (6.4)$$

and has the same value as for the Inline 1 and Staggered 2 cases, with the net heat transfer area within the domain $\Omega_f = 8(h + b)L_z$. In addition to the Reynolds numbers based on hydraulic diameter, Re_{D_h} , given by Equation 5.2 and the Reynolds number based on body thickness, $Re_{\bar{U}_{min}b}$, an additional Reynolds number based on louver pitch is defined as

$$Re_{L_p} = \frac{\bar{U}_{min}^* L_p^*}{\nu} \quad (6.5)$$

where the louver pitch, L_p , is shown in Figure 6.3. Finally an additional quantity, the mean flow angle, is also defined as

$$\alpha = \tan^{-1} \left(\frac{\bar{Q}_x/A_{min,x}}{\bar{Q}_y/A_{min,y}} \right) \quad (6.6)$$

and is a measure of the mean direction of the flow and is similar to the flow direction angle defined by Achaichia and Cowell [1]. The definitions for the Nusselt Number, j factor, f factor, lift-drag coefficient, and Strouhal number are unchanged and remain as defined in Equations 5.6- 5.15, but use the altered definition of \bar{U}_{min} in Equation 6.1.

Re	Re_{D_h}	$Re_{\bar{U}_{min}b}$	$Re_{\bar{U}_{min}L_p}$	α	\bar{C}_d	\bar{C}_l	\bar{C}'_l	f	$< Nu >$	j	St
10	176.0	39.2	234.8	12.6	4.64	-0.015	0.0	0.106	6.5	0.043	-
15	293.1	65.3	391.0	9.3	3.77	-0.010	0.0	0.086	10.8	0.042	-
20	444.0	99.0	592.4	7.7	2.92	-0.007	0.0	0.067	11.5	0.030	-
23	545.9	121.7	728.3	7.2	2.55	0.021	0.119	0.058	11.9	0.025	0.18
25	610.6	136.1	814.5	6.8	2.41	0.091	0.926	0.055	12.2	0.023	0.17
30	759.3	169.3	1013.0	6.1	2.27	0.198	1.300	0.051	15.4	0.023	0.16

Table 6.2: Calculated values for the Intermediate Offset case

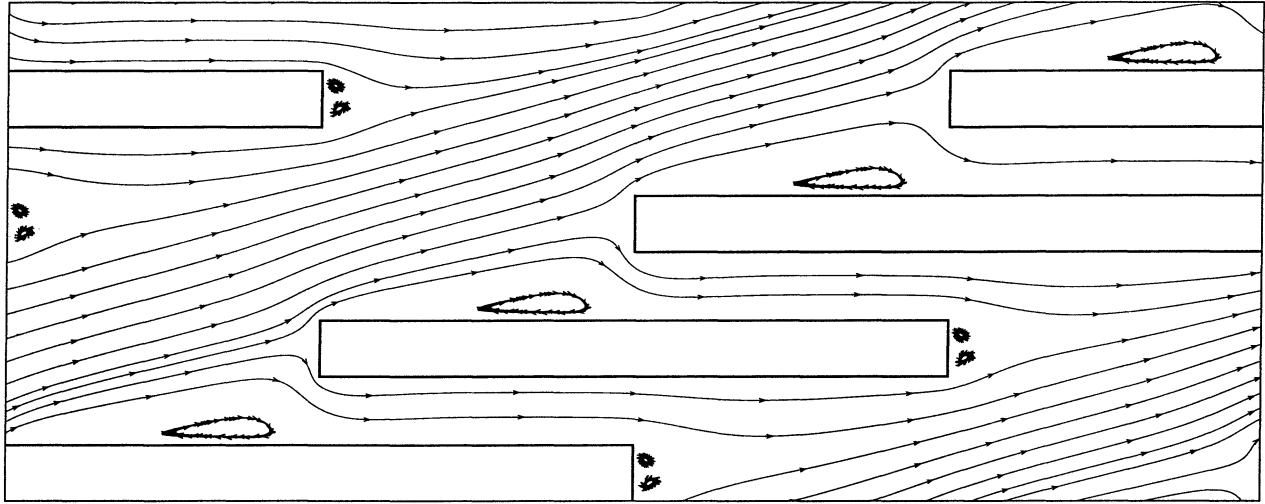
6.3 Flow Solutions

Flow solutions through the intermediate offset array have been obtained for six different Reynolds numbers. These Reynolds numbers and the calculated values for the various defined quantities are listed in Table 6.2. The following sections discuss various aspects of these flows in detail.

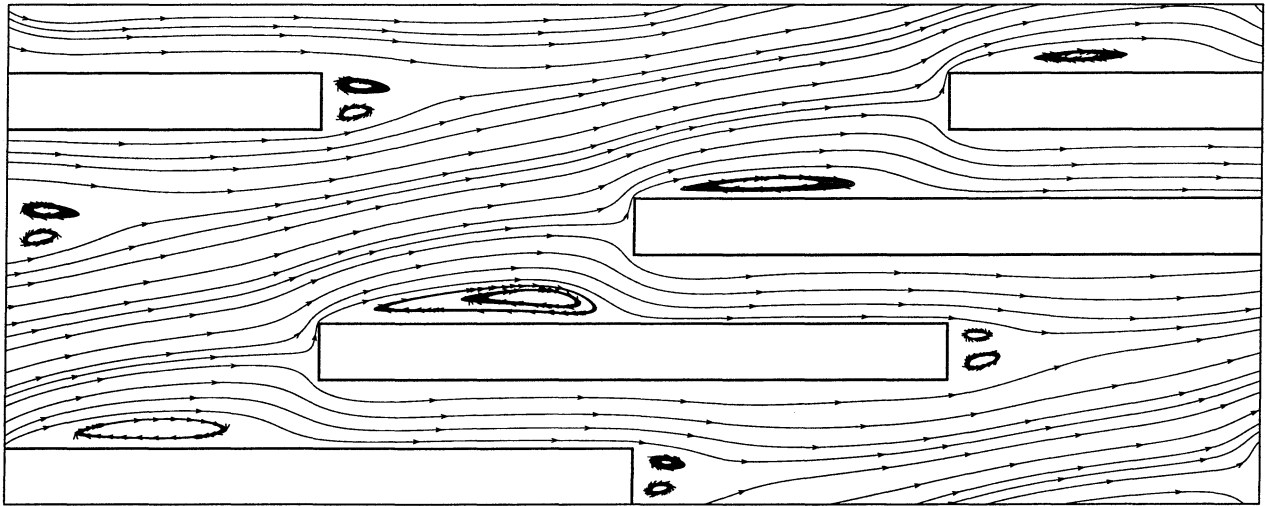
6.3.1 Flow Angle

A distinguishing characteristic of the flow in the Intermediate Offset array when compared to that of the Inline or Stagger cases is that, in a mean sense, the flow is not directed strictly in the x direction- the direction parallel to the body orientation. Instead the mean flow angle, α , listed in Table 6.2 may be seen to vary with the Reynolds number, with the flow having a larger angle to the x direction at smaller Reynolds numbers. In this sense the flow goes from being more duct directed at low Reynolds numbers to more louver directed at high Reynolds number. This may be seen in Figure 6.4 which shows the time averaged streamlines for the flow at Reynolds numbers of 10 and 30. At the lower Reynolds number a larger fraction of the flow may be seen to move at an angle to the x direction through the angled "duct" existing between fins. It is interesting to note that while the case under consideration is not a true model of flow through a louvered array, the same phenomena of Reynolds number dependent duct vs louver flow regimes is still observed.

A comparison may be made for the mean flow angle observed in the present simulations to those found in other examinations of flow through louvered arrays. Webb and Trauger [50] experimentally observed flow through louvered fin arrays using water channel dye visualization. They present the following correlation of their observations regarding mean flow angle at low to moderate Reynolds



(a)



(b)

Figure 6.4: Streamlines for the Intermediate Offset case at $Re = 10$ (a) and for the time averaged flow at $Re = 30$ (b)

Re	α	α_{wt}	α_{ac}
10	12.6	11.9	5.5
15	9.3	9.8	4.8
20	7.7	7.8	4.4
23	7.2	6.7	4.2
25	6.8	6.1	4.1
30	6.1	4.7	4.0

Table 6.3: Flow angle comparison

numbers,

$$\eta = 0.091 (Re_{L_p})^{0.39} \left(\frac{L_p}{F_p} \right)^{0.44} \left(\frac{\theta}{90} \right)^{0.3} \quad (6.7)$$

where η is a quantity they define as the flow efficiency, Re_{L_p} is the Reynolds number based on louver pitch, L_p is the louver pitch, F_p is the fin pitch, and θ is the louver angle. The equation may be recast to yield the mean flow angle, α , as tabulated in Table 6.2, giving

$$\alpha_{wt} = \theta - \tan^{-1} \left[0.091 (Re_{L_p})^{0.39} \left(\frac{L_p}{F_p} \right)^{0.44} \left(\frac{\theta}{90} \right)^{0.3} \tan \theta \right] \quad (6.8)$$

A comparison of the mean flow angles determined from the Webb-Trauger correlation and from the present computations are shown in Table 6.3. These results show surprisingly good agreement given the differences in the array geometries considered and the difference between the orientations of the arrays with respect to the driving pressure gradient, or a uniform oncoming flow.

The results for the present flow may be also be compared with the results for louver array flow studied numerically by Achaichia and Cowell [1]. In their work Achaichia and Cowell present an correlation for flow direction, which is shown here recast in terms of the flow angle α

$$\alpha_{ac} = \theta - \left[0.936 - \frac{243}{Re_{L_p}} - 1.76 \frac{F_p}{L_p} + 0.995\theta \right] \quad (6.9)$$

Achaichia and Cowell use fins of zero thickness, which requires the louver pitch be related to the louver gap c by the relation, $L_{pac} = c / \sin \theta$. In using this correlation for the present case of finite thickness fins it would appear desirable to redefine the louver pitch to satisfy the relation for L_{pac} above, which yields a louver pitch of 2.96 for the present case. Using this louver pitch

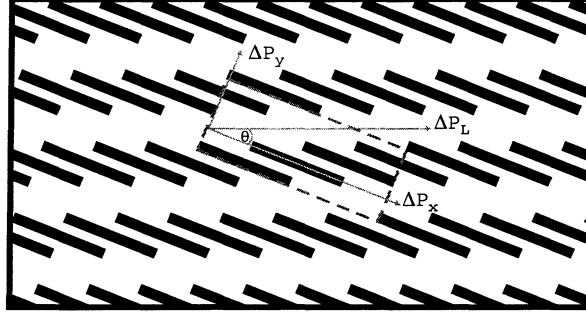


Figure 6.5: Pressure Gradient Orientation

in Equation 6.9 produces the values of mean flow angle listed in Table 6.3. The agreement is not particularly good, with the correlation showing a smaller flow angle than what is observed for the Intermediate Offset case. The disagreement in these results however may be due to the use of zero fin thickness to produce the correlation and presence of the inter-body channel in the Intermediate Offset geometry.

In general the present flow shows behavior similar to that observed for flow in louvered arrays. The direction of the flow is "duct" oriented at low Reynolds number and asymptotically approaches a louver oriented flow at higher Reynolds numbers. The mechanism for determining the flow angle, or choosing between duct and louver directed flow, has been noted by Daveport [10] and by Achaichia and Cowell [2] to be the viscous resistance to flow through the channels between the louvers. At low Reynolds numbers, or high viscosity, this resistance is high causing a larger portion of the flow to travel in the duct region between rows of louvered fins. At high Reynolds numbers, or low viscosity, more flow is able to pass through the louver channels allowing the flow to be more louver directed. This same mechanism is responsible for the determining the flow angle in the current Intermediate Offset geometry. As stated previously one of the differences between the current model and a louver flow model is the orientation of the pressure gradient relative to the fin orientation. Figure 6.5 shows a louver array model where the flow is driven by the pressure gradient ΔP_L , which may be broken into two component parts ΔP_x and ΔP_y . For a louver angle, θ , of 21.8 degrees $\Delta P_x = 0.93\Delta P_L$ and $\Delta P_y = 0.37\Delta P_L$. In the present offset model the flow is driven by a pressure gradient in the direction of ΔP_x , making the difference between it and a louver array model the pressure gradient ΔP_y . This difference would tend to manifest by producing a flow which is moderately more louver aligned for the Intermediate Offset case at a given Reynolds

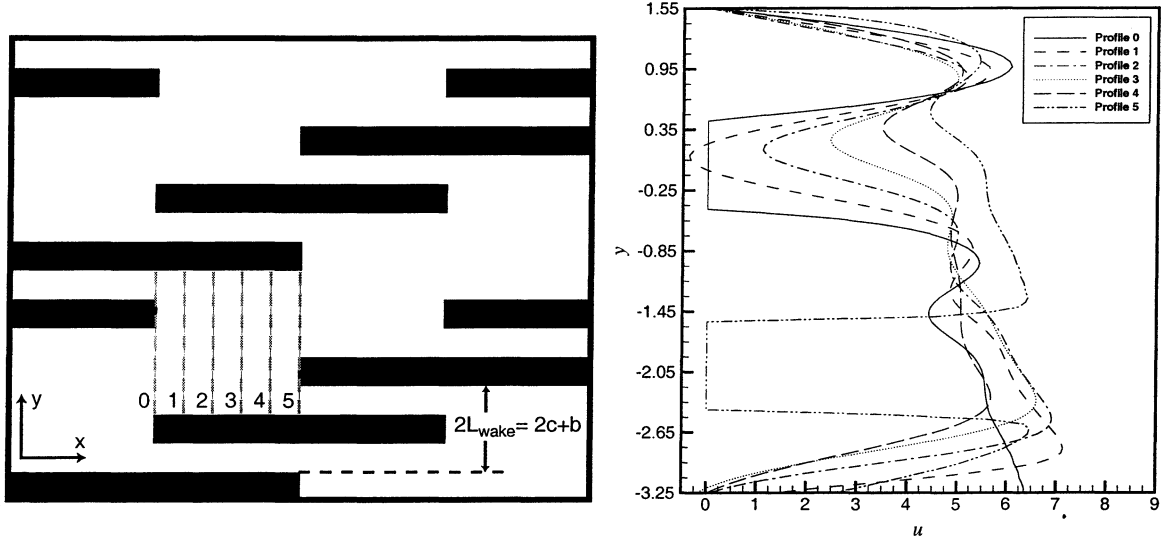


Figure 6.6: Profiles of U velocity for the Intermediate Offset Array at $Re= 22$

number than would occur in the louver flow model. However, the presence of the inter-body channel in the Intermediate Offset array tends to increase the hydraulic resistance to louver directed flow making the flow more likely to be duct directed, thus the two effects may tend to cancel each other out. The degree of difference in the flow angle at the low Reynolds number between the offset and louver arrays is not clear, but the comparison to the results of Webb and Trauger suggests it may not be large. On a final note, it would be possible to produce a proper model of louver flow with the existing code by specifying the proper values of β_x and β_y in Equation 2.7 to produce a properly oriented driving pressure gradient.

6.3.2 Stability

The transition from steady laminar, to periodic unsteady flow does not appear to effect the mean angle of the flow. This transition for the Intermediate Offset array was found to occur at a Reynolds number, Re , of 22. This may be observed from the data listed in Table 6.2 where for Reynolds numbers less than 22 the flow is steady, having zero lift fluctuation, C'_l , and correspondingly no Strouhal number. Above the critical Reynolds number the flow becomes unsteady, with fluctuating lift and periodic vortex shedding.

The value of the critical Reynolds number for the Intermediate Offset array may be compared

to that of the Inline 1 and Staggered 2 arrays. A comparison based on, $Re_{\bar{U}b}$, where $\bar{U} = Q_x/L_y$ and b is the fin thickness, shows that the critical Reynolds numbers are 31.4, 60.9, and 62.3 for the Inline 1, Staggered 2, and Offset cases respectively. Using the alternative scaling for stability results suggested in Section 4.5 and the Reynolds number, $Re_{\bar{U}_{chan}L_{wake}}$, yields critical Reynolds numbers of 127, 135, and 139 for the Inline 1, Staggered 2, and Offset cases. For consistency the average velocity in the inter-body channels, \bar{U}_{chan} , was taken as $\bar{U}_{chan} = Q_x/(L_y - 2b)$ and the length scale, L_{wake} , was set to $L_{wake} = c + b/2$. The choice of the value of L_{wake} was motivated by the profiles of the u velocity in the wake of an offset body shown in Figure 6.6. This figure shows six profiles of u velocity, starting at the trailing edge of a body and taken at increments of one non-dimensional length unit in the x direction, with the center line of the upstream body at $y = 0$. A comparison to the profiles for the Staggered 2 case shown in Figure 4.9(b) shows a marked similarity in the profiles over the upper 2.6 non-dimensional length units. Over this range the early profiles for the two cases exhibit a similar double-peaked structure. The lower portion of the Offset array profiles, however, deviate from the Staggered profiles due to the lack of a lower bounding surface symmetric to the upper one. Overall roughly 85% of the Staggered 2 profile is repeated in the profile for the Offset array, suggesting the choice of L_{wake} be the same as that of the Staggered 2 array. Given the similarities of the velocity profiles, and the role of the profiles in determining the flow stability, it is not surprising that the critical Reynolds number for the Staggered 2 array and the Intermediate Offset array are nearly identical.

Due to the similarities in the critical Reynolds numbers and in the unsteady flow regimes, which will be discussed subsequently for the Offset array, it is evident that the transition from laminar to unsteady flow in the Offset array is attributable to the same type of wake instability that occurs in the Inline and Staggered arrays. As the flow is largely louver directed at the point where it becomes unstable it is not surprising that it should be subject to the same type of instability. The approximate similarity between the Offset array and louver array models suggests that the same type of instability may be the cause of transition to unsteady flow in a louvered array where the flow becomes predominately louver directed before the onset of flow instability. Extrapolating from the present results it may be argued that the flow will become louver directed before it becomes unstable for a range of fin pitches. The results of Achaichia and Cowell shown in Equation 6.9 indicate that

for a given fluid and array geometry increasing the pitch, L_p , will cause the flow to become more louver directed for a fixed flow velocity, or alternatively the same flow angle can be achieved at a lower flow velocity. The stability results of Section 4.5 show that the type of instability occurring in the Offset array causes a transition at a constant Reynolds number, $Re_{\bar{U}_{chan}L_{wake}}$. Thus for a given fluid in a given array increasing the pitch will cause the flow to become unstable at a lower flow velocity. Both the flow velocity needed to obtain a given flow angle and the velocity needed for the flow to become unstable have a similar $1/L_p$ dependence. It is therefore likely that the flow will remain predominately louver directed before becoming unstable for a range of fin pitches. Therefore, in many cases it will not be the duct directed flow over the irregular louver geometry that leads to flow instability, but instead the same general wake instability that occurs for Inline and Staggered arrays.

6.3.3 Unsteady Flow

After the onset of instability the flow in the Offset array changes from a steady flow of the type shown in Figure 6.4(a), to an unsteady, vortex shedding flow which is depicted in Figures 6.7 - 6.9. Figure 6.4(a) shows a streamline plot of the flow solution over four bodies in an infinite Offset array at a Reynolds number, Re , of 10. As previously discussed the flow moves at angle to the bodies, and a pronounced recirculation region may be observed over the first half of the upper surface of each fin. A small recirculation region is also present at the rear of each body. Figures 6.7 - 6.9 show a sequence of vector, swirl, and temperature solutions at a Reynolds number, Re , of 30. Plots are shown at an increment of 0.18 time units, and the flow is temporally periodic so the first plot (a) follows the last plot (e) in a repeating sequence. The effects of flow unsteadiness may be readily observed in these figures. The wake region behind each body may be observed to show an oscillating waviness in the vector plot, which correspond in the swirl plot to vortices shed from the trailing edge of each body. As with the Inline and Staggered array the wake vortices are shed alternately from the top and bottom surfaces of the body and generally propagate in the x direction with a small deflection attributable to the angled mean flow. Vortices are also shed at the leading edge, with the vortices shed at the top surface being larger and more intense than those shed from the lower surface. The vortices shed from the upper leading edge may be seen to propagate through

a region of low velocity existing over the first half of the upper surface, and are clearly visible in the vector plot. Both sets of vortices shed from the leading edge propagate along the entire length of the body, however the upper vortices become weaker and more compact as they pass into the channel region between bodies. Both the wake and the leading edge vortex shedding have the same period as does the shedding on different bodies. However, the shedding is not synchronized between the different bodies, with each body at a different phase. The effects of the vortices may be observed in the temperature solutions shown in Figure 6.9. The thermal boundary layer may be observed to be thickest along the first half of the upper surface, or along the region of low flow velocity. The thickness of the thermal boundary layer in this region, and along the length of the fin, is effected by the presence of the shed vortices.

As with the Inline and Staggered arrays the intensity of the vortices in the near-surface region may be quantified by considering the normalized, y integrated swirl. The near surface region was considered to extend a distance of 1.1 units away from the surface, and the upper and lower surfaces were integrated separately to evaluate the difference in vortex intensity on the two sides of the body. Figure 6.10 shows the swirl intensity as it varies along the upper surface of the body (a) and the lower surface of the body (b). As was expected, the swirl intensity is generally higher along the upper surface of the body. Along both surfaces the swirl intensity shows sharp peaks at the front and rear of the body and at the mid point where the leading or trailing edges of adjacent bodies lie. These peaks are attributable to the sharp deflections that the flow undergoes at these points. Along the upper surface the swirl intensity may be seen to be highest in the recirculation region along the front of the body. Along both surfaces the swirl intensity shows an increase with increasing Reynolds number, with the largest increase occurring for the Re equal to 30 case where strong vortex shedding is present.

Another significant local quantity is the Nusselt number. Figure 6.11 shows the time averaged local Nusselt number along the (a) upper and (b) lower surfaces of the body. The Nusselt number may be observed to differ between the upper and lower surfaces, though the difference exists primarily over the first half of the body. Along the later half of the body the Nusselt numbers on the two surfaces are in fairly close agreement. The difference in the Nusselt numbers over the front portion of the body is attributable to the recirculation region which exist over the upper surface.

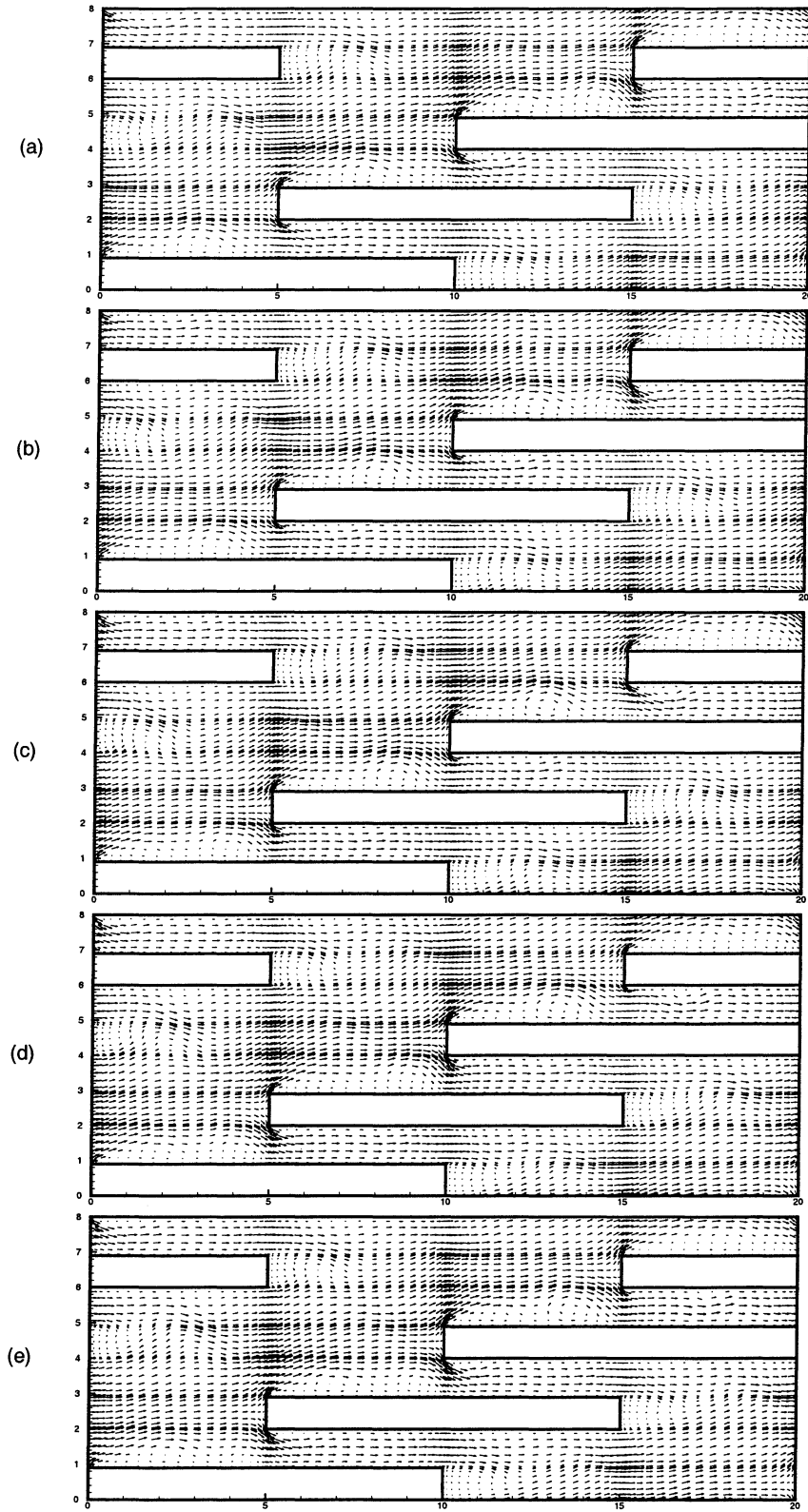


Figure 6.7: Vector plot of the Intermediate Offset array solution at $Re=30$ showing 5 time instances 0.18 time units apart

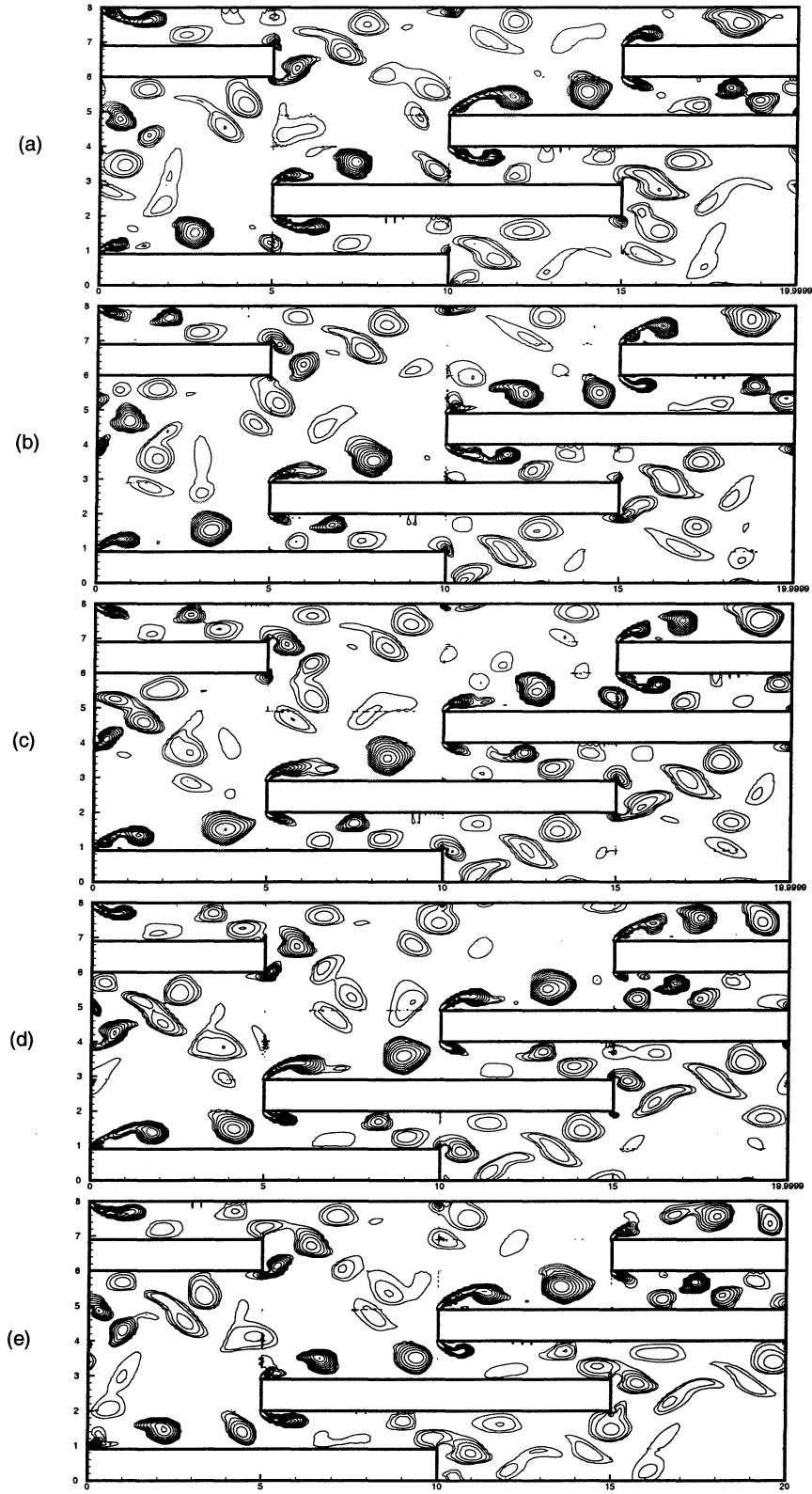


Figure 6.8: Swirl plot of the Intermediate Offset array solution at $Re = 30$ showing 5 time instances 0.18 time units apart

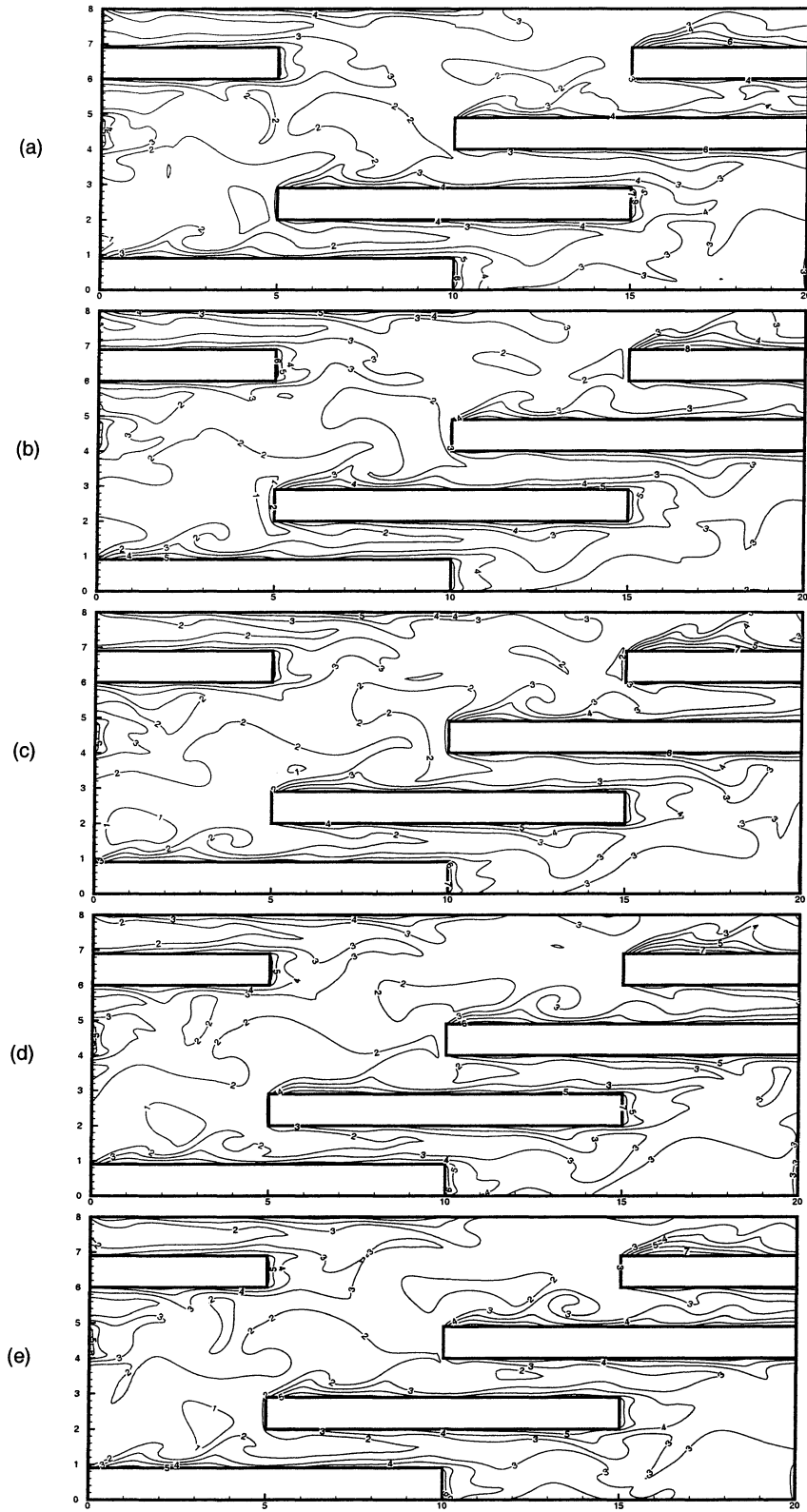


Figure 6.9: Temperature plot of the Intermediate Offset array solution at $Re=30$ showing 5 time instances 0.18 time units apart

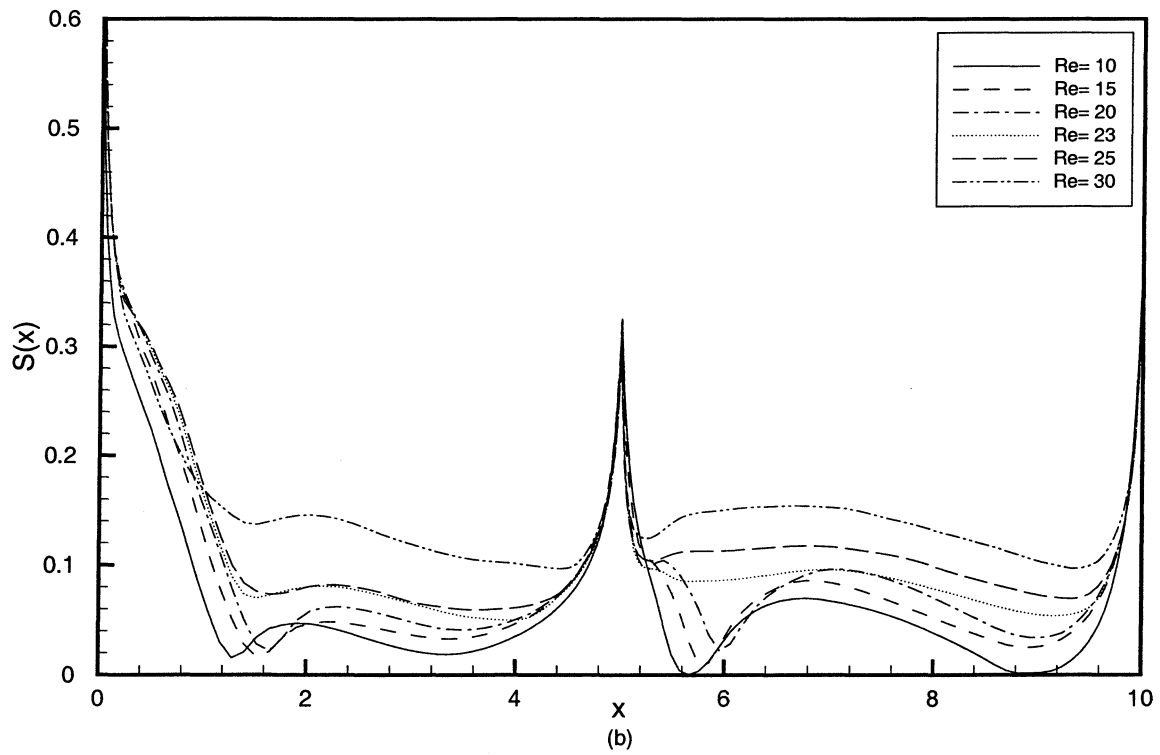
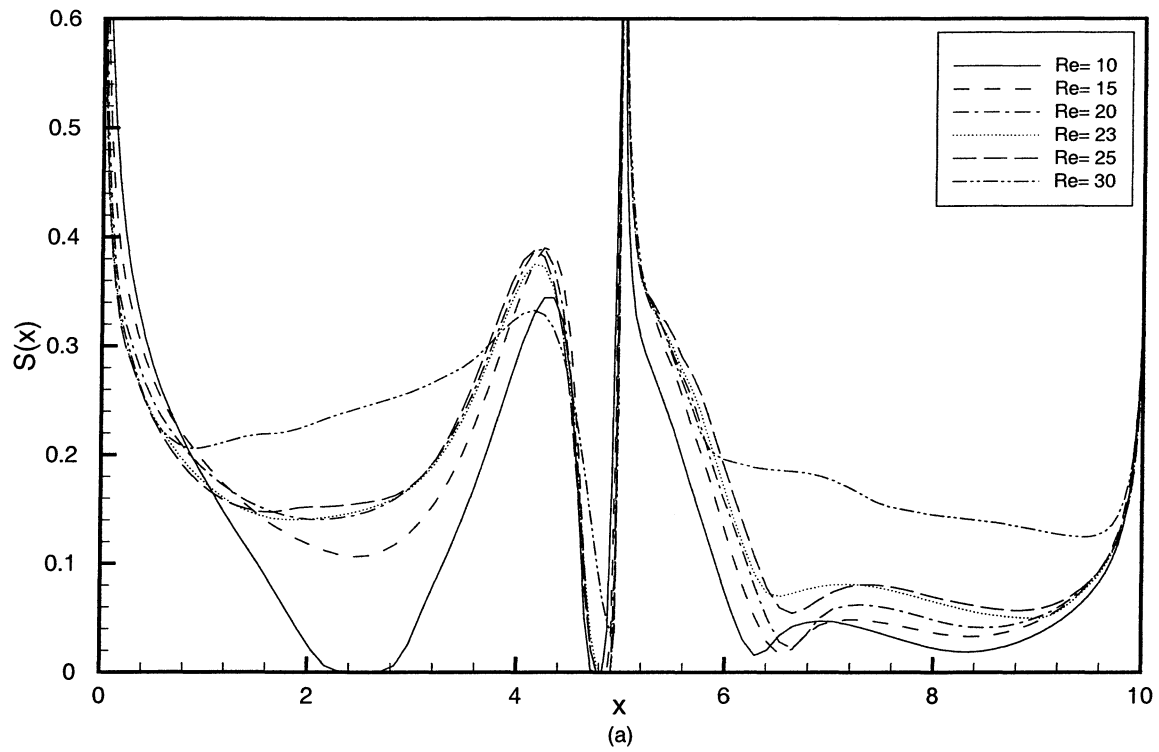


Figure 6.10: Swirl Intensity for the Intermediate Offset array over the near surface region along the upper surface (a) and the lower surface (b)

For both surfaces the Nusselt number peaks sharply at the start of the body where the new thermal boundary layer is thin. Along the lower surface the Nusselt number generally decays along the length of the body. Along the upper surface the Nusselt number decays rapidly from the leading edge peak through the recirculation region. Beyond the recirculation region the Nusselt number recovers and peaks just beyond the leading edge of the upper adjacent fin, after which it slowly decays. A significant increase in the local Reynolds number occurs for the $Re = 30$ case, where strong vortex shedding is present. The effect of strong vortex shedding is particularly noticeable in the recirculation region.

Finally the f and j data for the Intermediate Offset array may be compared to that of the Inline 1 and Staggered 2 arrays. These data are listed in Table 6.2 and plotted in Figure 6.12, which compares the results for the three array geometries. The values of f and j for the Offset array lie between those of the Inline and Staggered arrays, but noticeably closer to the results for the Staggered array. The data for all three cases show nearly the same dependence on the Reynolds number based on hydraulic diameter, Re_{D_h} .

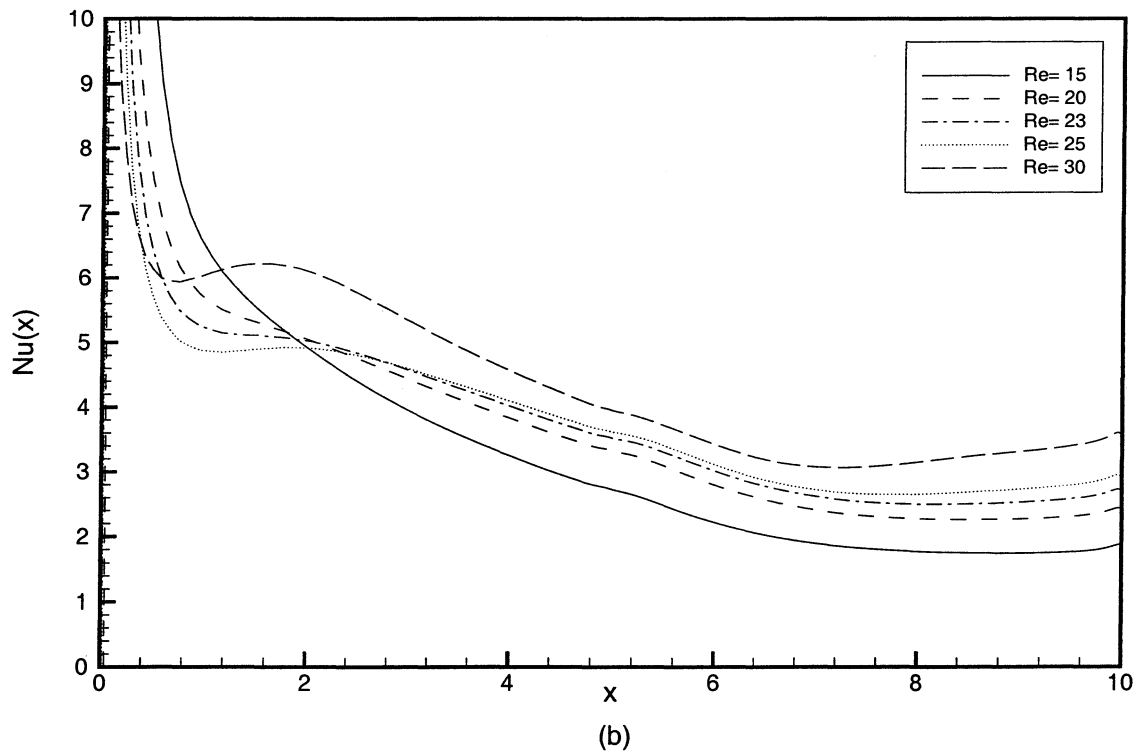
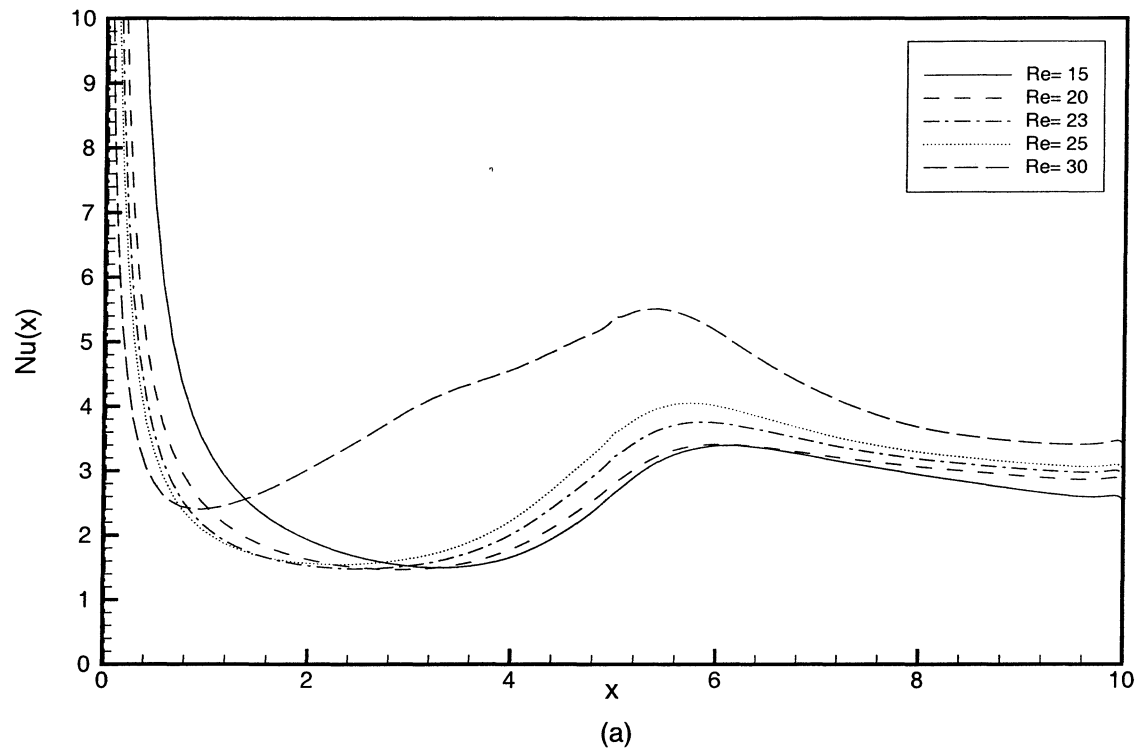


Figure 6.11: Time averaged local Nusselt number for the Intermediate Offset array along the upper surface (a) and the lower surface (b)

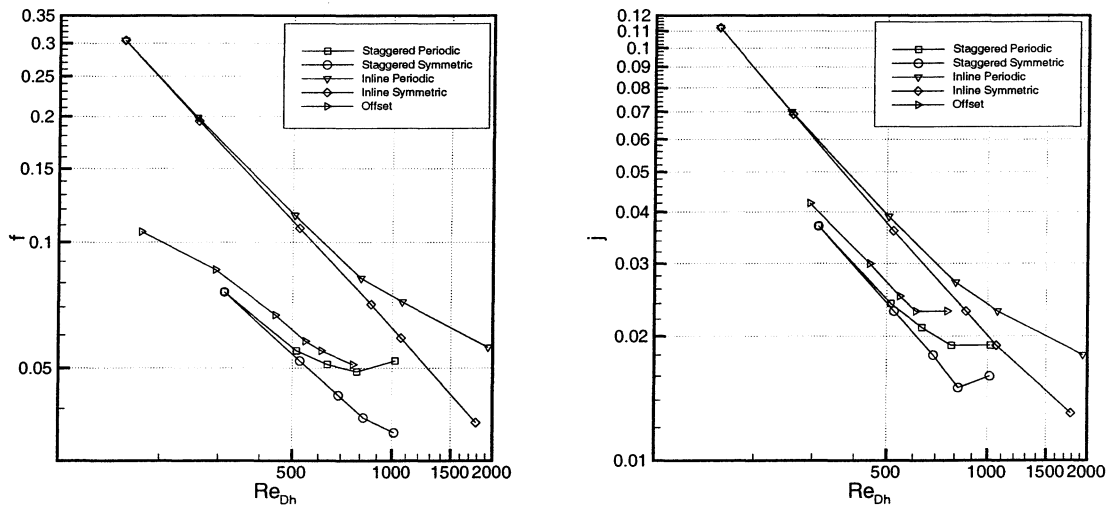


Figure 6.12: f and j factors as a function of Reynolds number for the Inline 1, Staggered 2, and Intermediate Offset case

Chapter 7

Conclusions

The present study utilized numerical simulations and theoretical analysis to investigate the flow, stability, and heat transfer characteristics of a dozen different geometries. The geometries considered consisted of; eight infinite arrays of rectangular bodies in Inline, Staggered, or Intermediate Offset configurations, a single column of rectangular bodies, a single column of square bodies, a single square body, and a single rectangular body. Stability results, including perturbation growth rates, critical Reynolds numbers, and eigenfunctions are reported for each of the above cases. Detailed flow and heat transfer solution data are reported for an Inline, Staggered, and Intermediate offset case, with a focus on the vortex shedding behavior.

The numerical analysis was performed using a specially developed spectral multi-domain solver for the governing flow and energy equations. This algorithm combines the flexibility of the multi-domain decomposition with the accuracy of a spectral discretization. Furthermore it provides excellent scalability on parallel computational architectures. Infinite array simulations were performed using periodic boundary conditions applied to a small unit periodic cell. Simulations for finite geometries employed a buffer domain outflow boundary condition, and all temperature solutions used a constant heat flux boundary condition.

Numerical two-dimensional stability analysis of the steady base flow was performed for each of the geometries. Disturbance growth rates were determined by adding a generalized disturbance to the steady base flow solutions and monitoring the change in disturbance energy. In unstable base flows the disturbance energy grew exponentially at a constant rate, while for stable flows it exponentially decayed. Steady base flow solutions at super-critical Reynolds numbers were obtained through the application of a symmetry condition about the bodies, which prevented the growth of

the disturbance. From the disturbance growth rates the critical Reynolds number for each geometry was determined. The proper scaling for defining the critical Reynolds number was determined through a one-dimensional analytic stability analysis of the sinusoidal streamwise velocity profiles observed in the Inline array configurations. The proper scaling was found to be based on the wavelength of the profile, or the transverse pitch of the array, and the magnitude of the primary sinusoidal oscillation. These scaling results were generalized to include Staggered arrays, and recast into more physical parameters, producing a general theory for determining the stability of Inline and Staggered bluff body arrays. The stability of the flow was shown to be dependent primarily upon the transverse spacing of the bodies and the average velocity in the inter-body channels, for low to moderate transverse body spacing. For large transverse spacing the stability of the flow was equivalent to that of a single isolated body. In the intermediate range of transverse spacings the critical Reynolds number increased from the lower value of an array to the higher value corresponding to an isolated body. Thus, the primary parameters impacting the point of transition from steady flow to unsteady flow with vortex shedding have been identified and the flow velocity at which transition occurs may be predicted for a given geometry. For example, a typical compact heat exchanger with a 1 millimeter fin pitch may expect to see flow transition at oncoming flow velocities on the order of 4 m/s.

The predictions for the onset of flow instability in the present work may be compared with experimental observations. Mullisen and Loehrke [35] present experimental data for inline arrays and identify the onset of flow instability based on changes in the f and j factor curves. For an inline geometry similar to that of the present Inline 2 array, Mullisen and Loehrke [35] report a critical Reynolds number, $Re_{\bar{U}_{chan, L_{wake}}}$, of 244, which may be compared with the value of 129 for the Inline 2 array. The factor two difference in these results may be attributed to the method by which unsteady flow was identified from the experimental data. From the f and j data for the present Inline arrays (See Figure 5.6, Tables 5.1 and 5.2) it may be seen that noticeable change in the f and j curves occur only at Reynolds numbers significantly above the critical value for true onset of flow unsteadiness. For example in Figure 5.6 a five percent increase in f and j factors above their steady state values occurs only at a Reynolds number nearly twice as large as the critical Reynolds number. Thus the data of Mullisen and Loehrke [35] can be considered to provide

adequate experimental support to the present computational and theoretical results.

A more accurate comparison of critical Reynolds numbers may be performed using data from water channel dye visualization experiments by DeJong and Jacobi [11]. For a staggered array comparable to the present array in geometry and arrangement they report a critical Reynolds number, $Re_{\bar{U}_{chan,Lwake}}$, of 155 which compares favorably to the value of 136 found for Staggered arrays from the present analysis. The slightly higher critical Reynolds number in the experimental measurement can again be explained in terms of higher saturation amplitude required for experimental observation of the instability.

The unsteady flow that follows the onset of instability was studied in detail for related Inline and Staggered arrangements. Detailed flow and temperature solutions were obtained and presented at differing Reynolds numbers throughout the regime where the flow is unsteady with a single characteristic frequency. For higher Reynolds numbers the flow was observed to be characterized by an increasing number of frequencies until the flow became chaotic. Vortex shedding was observed to occur simultaneously at the leading and trailing edges of the bodies in an array. Simulations of flow over a single column of bodies showed wake vortex shedding with no initial leading edge vortex shedding at Reynolds numbers just above the critical value. Leading edge vortex shedding results from a second bifurcation at a higher Reynolds number. Thus, it can be concluded that it is the presence of upstream bodies shedding vortices which results in the simultaneous onset of leading and trailing edge vortex shedding in the case of an array. Trailing edge vortex shedding behavior was found to be similar to that of an isolated body, with vortices shed periodically from alternating surfaces of the body. However, a unique angled motion of the trailing edge vortices was observed for infinite Inline arrays. The strength of the leading edge vortices was quantified and found to increase smoothly with increasing Reynolds number, with the vortex strength being relatively weak close to the critical Reynolds number. The position of the leading edge vortices was shown to be correlated with an increase in the local Nusselt number. The overall effect of the leading edge vortices on heat transfer was quantified by a comparison of j factor values for shedding and symmetric non-shedding flows over the same range of Reynolds numbers. A twenty percent increase in j factor for the shedding vs. non-shedding flows occurs at one and a half times the critical Reynolds number for the Staggered arrangement and four times the critical Reynolds

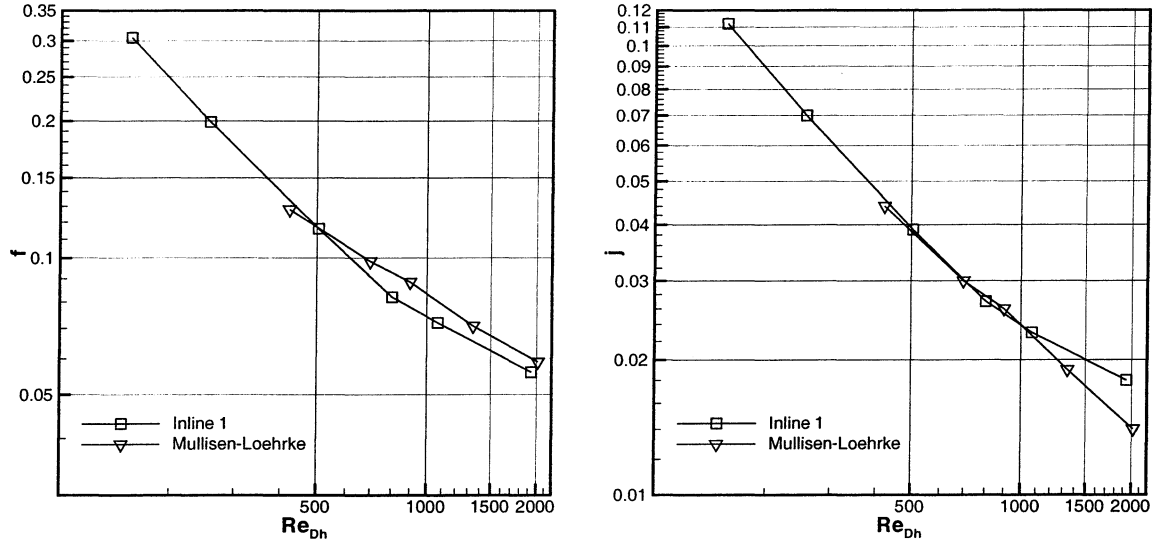


Figure 7.1: Inline 1 f and j data compared with Mullisen and Loehrke

number for the Inline arrangement. These results are consistent with experimentally obtained data for f and j . A comparison of the present results with the experimental data of Mullisen and Loehrke [35] for a similar geometry is shown in Figure 7.1, where generally good agreement may be observed. The difference observed at higher Reynolds number can be attributed to the three dimensional nature of the flow.

Finally, the flow and heat transfer characteristics of an alternate geometric case, the Intermediate Offset array, which is a variant of the Inline and Staggered geometries, was considered. This case was observed to display the same phenomenon of duct and louver directed flow observed in louvered arrays. However the stability of the flow was found to be very similar to that of the Staggered array, as was the nature of unsteady laminar flow regime. The strength of the leading edge vortices, however, was observed to be asymmetric about the body, with the vortices on the upper surface being larger and stronger. The relation of the flow stability characteristics to that of a staggered array plus the rough similarity in geometry and flow characteristic to that of a louvered array, suggest that the general mechanism of array flow stability reported in this work may extend to louver array geometries as well.

References

- [1] A. Achaichia and T. A. Cowell. A finite difference analysis of fully developed periodic laminar flow in inclined louvre arrays. In *Proceedings of 2nd UK National Heat Transfer Conference*, pages 883–897, Glasgow, 1988.
- [2] A. Achaichia and T. A. Cowell. Heat transfer and pressure drop characteristics of flat tube and louvered plate fin surfaces. *Experimental Thermal and Fluid Science*, 1:147–157, 1998.
- [3] Hiroshi Aoki, Tsutomu Shinagawa, and Kazuhiko Suga. An experimental study of the local heat transfer characteristics in automotive louvered fins. *Experimental Thermal and Fluid Science*, 2:293–300, 1989.
- [4] F. N. Beauvais. An aerodynamic look at automobile radiators. *SAE Paper*, 650470, 1965.
- [5] C. Canuto, A. Quarteroni, and T. A. Zang. *Spectral Methods in Fluid Dynamics*. Springer Verlag, 1988.
- [6] C. Carlenzoli and P. Gervasio. Effective numerical algorithms for the solution of algebraic systems arising in spectral methods. *Applied Numerical Mathematics*, 10:87–113, 1992.
- [7] A. J. Chorin. Numerical solution of the navier-stokes equations. *Mathematics of Computation*, 22:745–762, 1968.
- [8] T. A. Cowell, M. R. Heikal, and A. Achaichia. Flow and heat transfer in compact louvered fin surfaces. *Experimental Thermal and Fluid Science*, 10:192–199, 1995.
- [9] N. Cur and E. M. Sparrow. Experiments on heat transfer and pressure drop for a pair of colinear, interrupted plates aligned with the flow. *International Journal of Heat and Mass Transfer*, 21:1069–1080, 1978.

- [10] C. J. Davenport. Heat transfer and flow friction characteristics of louvered heat exchanger surfaces. In J. Taborek, G. F. Hewitt, and N. Afgan, editors, *Heat Exchangers: Theory and Practices*, pages 397–412. Hemishpere, 1983.
- [11] N. C. DeJong and A. M. Jacobi. An experimental study of flow and heat transfer in parallel-plate arrays: Local, row-by-row, and surface average behavior. *International Journal of Heat and Mass Transfer*, 40(6):1365–1378, 1997.
- [12] N. C. DeJong, L. W. Zhang, A. M. Jacobi, S. Balachandar, and D. K. Tafti. A complementary experimental and numerical study of the flow and heat transfer in offset strip-fin heat exchangers. *Journal of Heat Transfer*, 120:690–698, 1998.
- [13] Nicole Christine DeJong. *Flow, Heat Transfer, and Pressure Drop Interactions in Louvered Fin Arrays*. PhD thesis, University of Illinois at Urbana-Champaign, 1999.
- [14] P. G. Drazin and W. H. Reid. *Hydrodynamic Stability*. Cambridge University Press, 1981.
- [15] Daniele Funaro. A multidomain spectral approximation of elliptic equations. *Numerical Methods for Partial Differential Equations*, 2:187–205, 1986.
- [16] Philip M. Gresho and Robert L. Sani. On pressure boundary conditions for the incompressible navier-stokes equation. *International Journal for Numerical Methods in Fluids*, 7:1111–1145, 1987.
- [17] K. Hannemann and H. Oertel, Jr. Numerical simulation of the absolute and convectively unstable wake. *Journal of Fluid Mechanics*, 199:55–88, 1989.
- [18] Michio Hiramatsu, Tsuneo Ishimaru, and Koushou Matsuzaki. Research on fins for air conditioning heat exchangers. *JSME International Journal, Series II*, 33(4):749–756, 1990.
- [19] Huai-Zhang Huang and Wen-Quan Tao. An experimental study on heat/mass transfer and pressure drop characteritics for arryas of nonuniform plate length positioned obliquely to the flow direction. *Journal of Heat Transfer*, 115:568–575, 1993.
- [20] C. P. Jackson. A finite elment study of the onset of vortex shedding in flow past variously shaped bodies. *Journal of Fluid Mechanics*, 182:23–45, 1987.

- [21] Sony Joseph. Personal communication, 2000.
- [22] Himanshu M. Joshi and Ralph L. Webb. Heat transfer and friction in the offset strip-fin heat exchanger. *International Journal of Heat and Mass Transfer*, 30:69–83, 1987.
- [23] Ronald D. Joslin, Craig L. Streett, and Chau-Lyan Chang. Validation of three-dimensional incompressible spatial direct numerical simulation code. Technical Report 3205, NASA Langely Research Center, 1992.
- [24] W. M. Kays and A. L. London. *Compact Heat Exchangers*. McGraw-Hill, 1964.
- [25] J. Kim and P. Moin. Application of a fractional-step method to incompressible navier-stokes equations. *Journal of Computational Physics*, 59:308–323, 1985.
- [26] Y. Kurosaki, T. Kashiwagi, H. Kobayashi, L. Uzuhashi, and S. Tang. Experimental study on heat transfer from parallel louvered fins by laser holographic interferometry. *Experimental Thermal and Fluid Science*, 1:59–67, 1988.
- [27] Y. N. Lee. Heat transfer and pressure drop characteristics of an array of plates aligned at angles to the flow in a rectangular duct. *International Journal of Heat and Mass Transfer*, 29(10):1553–1563, 1986.
- [28] A. L. London and R. K. Shah. Offset rectangular plate-fin surfaces - heat transfer and flow friction characteristics. *Journal of Engineering for Power*, 90:218–228, 1968.
- [29] Raj M. Manglik and Arthur E. Bergles. The thermal-hydraulic design of the rectangular offset-strip-fin compact heat exchanger. In R.K. Shah et al, editor, *Compact Heat Exchangers*, pages 123–149. Hemisphere, 1990.
- [30] Raj M. Manglik and Arthur E. Bergles. Heat transfer and pressure drop correlations for the rectangular offset strip fin compact heat exchanger. *Experimental Thermal and Fluid Science*, 10:171–180, 1995.
- [31] S. V. Manson. Correlations of heat transfer data and of friction data for interrupted plane fins staggered in successive rows. *NACA TN*, 2237, 1950.

- [32] R. Mittal and S. Balachandar. Effect of three-dimensionality on the lift and drag of nominally two-dimensional cylinders. *Physics of Fluids*, 7(8):1841–1865, 1995.
- [33] S. Mochizuki and Y. Yagi. Characteristics of vortex shedding in plate arrays. In W. Merzkirch, editor, *Flow Visualization II*, pages 99–103. Hemisphere Publishing, 1982.
- [34] S. Y. Mochizuki, Y. Yagi, and W. Yang. Flow pattern and turbulence intensity in stacks of interrupted parallel-plate surfaces. *Experimental Thermal and Fluid Science*, 1:51–57, 1988.
- [35] R. S. Mullisen and R. I. Loehrke. A study of the flow mechanisms responsible for heat transfer enhancement in interrupted-plate heat exchangers. *Journal of Heat Transfer*, 108:377–385, 1986.
- [36] R. H. Norris and W. A. Spofford. High-performance fins for heat transfer. *Transactions of ASME*, 64:489–496, 1942.
- [37] H. Oertel, Jr. Wakes behind blunt bodies. *Annual Review of Fluid Mechanics*, 22:539–564, 1990.
- [38] S. V. Patankar, C. H. Liu, and E. M. Sparrow. Fully developed flow and heat transfer in ducts having streamwise-periodic variations of cross-sectional area. *Journal of Heat Transfer*, 99:180–186, 1977.
- [39] S. V. Patankar and C. Prakash. An analysis of the effect of plate thickness on laminar flow and heat transfer in interrupted-plate passages. *International Journal of Heat and Mass Transfer*, 24:1801–1810, 1981.
- [40] A. Quarteroni and G. Sacchi-Landriani. Parallel algorithms for the capacitance matrix method in domain decomposition. *Calcolo*, 25(1-2), 1988.
- [41] Alfio Quarteroni and Giovanni Sacchi-Landriani. Domain decomposition preconditioners for the spectral collocation method. *Journal of Scientific Computing*, 3(1):45–76, 1988.
- [42] Joseph Robichaux. *Study of Three-Dimensional Vortex Shedding in the Wake of a Square Cylinder*. PhD thesis, University of Illinois at Urbana - Champaign, 1997.

- [43] A. Roshko. Perspectives on bluff body aerodynamics. *Journal of Wind Engineering and Industrial Aerodynamics*, 49:79–100, 1993.
- [44] A. Sohankar, C. Norberg, and L. Davidson. Low reynolds flow around a square cylinder at incidence: Study of blockage, onset of vortex shedding and outlet boundary condition. *International Journal for Numerical Methods in Fluids*, 26:39–56, 1998.
- [45] E. M. Sparrow, B. R. Baliga, and S. V. Patankar. Heat transfer and fluid flow analysis of interrupted-wall channels, with application to heat exchangers. *Journal of Heat Transfer*, 99:4–11, 1977.
- [46] E. M. Sparrow and A. Hajiloo. Measurement of heat transfer and pressure drop for an array of staggered plates aligned parallel to an air flow. *Journal of Heat Transfer*, 102:426–432, 1980.
- [47] E. M. Sparrow and C. H. Liu. Heat transfer, pressure-drop and performance relationships for in-line, staggered, and continuous plate heat exchangers. *International Journal of Heat and Mass Transfer*, 22:1613–1624, 1979.
- [48] C. L. Streett and M. G. Macaraeg. Spectral multi-domain for large-scale fluid dynamic simulations. *Applied Numerical Mathematics*, 6:123–139, 1989/90.
- [49] Kazuhiko Suga and Hiroshi Aoki. Numerical study on heat transfer and pressure drop in multilouvered fins. *ASME/JSME Thermal Engineering Proceedings*, 4:361–368, 1991.
- [50] Ralph L. Webb and Paul Trauger. Flow structure in the louvered fin heat exchanger geometry. *Experimental Thermal and Fluid Science*, 4:205–217, 1991.
- [51] A. R. Wieting. Empirical correlations for heat transfer and flow friction characteristics of rectangular offset-plate-fin heat exchangers. *Journal of Heat Transfer*, 97:488–490, 1975.
- [52] P. T. Williams and A. J. Baker. Incompressible computational fluid dynamics and the continuity constraint method for the three-dimensional navier-stokes equations. *Numerical Heat Transfer, Part B*, 29(2):137–273, 1996.
- [53] G. N. Xi, T. Murata, K. Suzuki, and Y. Hagiwara. An experimental study on heat transfer characteristics of offset-fin arrays. *Trans. JSME*, 55B:3507, 1989.

- [54] Guannan Xi, Shunzo Futagami, Yoshimichi Hagiwara, and Kenjiro Suzuki. Flow and heat transfer characteristics of offset-fin array in the middle reynolds number range. *ASME/JSME Thermal Engineering Proceedings*, 3:151–156, 1991.
- [55] W. Yang. Forced convective heat transfer in interrupted compact surfaces. In *Proceedings of the ASME/JSME Thermal Engineering Conference*, pages 105–111. ASME, 1983.
- [56] Hyun Sik Yoon. Personal communication, 2000.
- [57] H. Zhang and X. Lang. The experimental investigation of oblique angles and interrupted plate lengths for louvered fins in compact heat exchangers. *Experimental Thermal and Fluid Science*, 2:100–106, 1989.
- [58] L. W. Zhang, S. Balachandar, and D. K. Tafti. Effects of intrinsic three dimensionality on heat transfer and friction loss in a periodic array of parallel plates. *Numerical Heat Transfer Part A*, 31(4):327–353, 1997.
- [59] L. W. Zhang, S. Balachandar, D. K. Tafti, and F. M. Najjar. Heat transfer enhancement mechanisms in inline and staggered parallel-plate fin heat exchangers. *International Journal of Heat and Mass Transfer*, 40(10):2307–2325, 1997.
- [60] Lizheng Winston Zhang. *A Numerical Study of Flow and Heat Transfer in Compact Heat Exchangers*. PhD thesis, University of Illinois at Urbana - Champaign, 1996.
- [61] Jigen Zhou. *Self-sustaining formation of packets of hairpin vortices in a turbulent wall layer*. PhD thesis, University of Illinois at Urbana - Champaign, 1997.